A MODEL BASED APPROACH TO THE ANALYSIS OF INTERSECTION CONFLICTS AND COLLISION AVOIDANCE SYSTEMS

by

Kazutoshi Nobukawa

A dissertation submitted in partial fulfillment
of the requirements for the degree of
Doctor of Philosophy
(Mechanical Engineering)
in The University of Michigan
2011

Doctoral Committee:

Professor Timothy J. Gordon, Chair
Professor Jessy W. Grizzle
Professor Huei Peng
Professor Noel C. Perkins

To my parents…

ACKNOWLEDGMENTS

This dissertation would not have been possible without a significant amount of help from various people. I would like to thank all of them, especially UMTRI staff, Ms. Michelle Barnes for providing the GIS data and spending time on the field study to collect the intersection data, Dr. Daniel Blower for providing the GES intersection crash data, Mr. Scott Bogard, Mr. Mark Gilbert, Mr. Michael Hagan and Dr. David LeBlanc for providing the detailed information necessary for conducting driving data analyses, Mr. Robert Goodsell for providing the left turn database and SQL advice, and Ms. Michelle Rasulis for providing the IT service necessary to complete the research; my friends at the University of Michigan, Dr. Tsuyoshi Higo, Dr. Atsushi Koguchi, Dr. Akira Saito, Dr. Eiji Saito, Ms. Krithika Srinivasan and Dr. Shingo Takeuchi for their valuable suggestions to complete the degree; my triathlon mates, who are also my valuable friends, Mr. Mrinal Iyer, Ms. Chrysta Lienczewski, Dr. Sebastian Martini, and Mr. Joseph Pak for keeping me healthy through fun training sessions; Ms. Anna Boot for detailed proofreading and delicious cooking; Professor Akio Fuwa, Professor Yoshiyuki Saito, and Professor Junichi Sakai at Waseda University, and Dr. Mitsuhito Hirota for encouragement and support before and during the initial period of my study abroad; my parents for patiently waiting for my degree; Professor Jessy Grizzle, Professor Huei Peng, and Professor Noel Perkins for generously participating in my dissertation committee despite their hectic schedules; and finally, my advisor, Professor Tim Gordon for all his help and support to complete my degree, provided with keen and enthusiastic advice on research studies, financial support, and delightful times outside the school, e.g. at the holiday party and during the trip to the conference, as well as providing me with valuable opportunities to work with various people from universities, the automotive industry, and the government.

TABLE OF CONTENTS

LIST OF FIGURES

FIGURE

LIST OF TABLES

TABLE

LIST OF APPENDICES

APPENDIX

LIST OF ABBREVIATIONS

a	DAS acceleration magnitude
a_x, a_y	DAS acceleration components in local coordinate system
$\hat{a}$	Acceleration magnitude from X-Y Kalman filter estimate/ Anticipated acceleration reference in the $\hat{a}$ speed control model
$\hat{a}_x, \hat{a}_y$	Acceleration estimates by X-Y Kalman filter in local coordinate system/
$\hat{a}$	Anticipated acceleration reference for the approach and turn stages in the speed control model
$\hat{a}_X, \hat{a}_Y$	Acceleration estimates by X-Y Kalman filter in global coordinate system
ACAS	Automotive Collision Avoidance System
d_1, d_2	Intersection parameters (distance)
DAS	Data acquisition system
$f_i(.)$	*i*-th objective function
FOV	Field of view
FN	False negative
FP	False positive
GT	Gap time
k_1, k_2	Parameters for predicted speed profile
LB	Leading buffer
LB_i	Leading buffer for *i*-th through vehicle
LTAP/OD	Left turn across path – opposite direction
nFN	Number of false-negative events
nFP	Number of false-positive events
nSB	Number of successful braking events given a true positive event

nTN	Number of true-negative events
nTP	Number of true-positive events
nUB	Number of successful braking events given a true positive event
p_1, p_2	Parameters for reference speed profile for deceleration stage
$P(.)$	Probability of an event
PET	Post encroachment time
POV	Principal other vehicle
q_1, q_2	Parameters for reference speed profile for acceleration stage
$R, \dot{R}$	Range and range rate of a target from the radar
RDCW	Road Departure Crash Warning System
s	Path coordinate
S_P	Pareto set
SV	Subject vehicle
SB	Successful braking
TB	Trailing buffer
TB_i	Trailing buffer for the i-th principal other vehicle
FN	False-negative
FP	False-positive
SB	Successful braking
TN	True-negative
TP	True-positive
UB	Unsuccessful braking
t_r	Transversal distance of a target from the center line of field of view of the radar
TTC	Time to collision
$T2C_{SV}$	Time for the left turn vehicle to arrive at encroachment zone (if it turn second), or leave encroachment zone (if it turns first)

$T2C_{POV}$	Time for the through vehicle to leave encroachment zone (if the left turn vehicle turns second), or arrive at encroachment zone (if the left turn vehicle turns first)
U	DAS speed
$\hat{U}$	Speed from the velocity estimates by X-Y Kalman filter
U_{pred}	Predicted speed profile
U_{ref}	Reference speed profile
U_{th}	Parameters for U_{ref}
UB	Unsuccessful braking
UMTRI	University of Michigan Transportation Research Institute
$\hat{v}_x, \hat{v}_y$	Velocity estimates by X-Y Kalman filter in local coordinate system
$\hat{v}_X, \hat{v}_Y$	Velocity estimates by X-Y Kalman filter in global coordinate system
$\mathbf{x}$	Decision vector
X, Y	X (positive to east) and Y (positive to north) coordinates transformed from geographical coordinates from GPS
$\hat{X}, \hat{Y}$	Position estimate by X-Y Kalman filter
δ	Intersection parameter (angle)
Δt_1	Latency difference estimate between GPS and data acquisition system
Δt_2	Latency difference estimate between GPS and radar
Δ_{LB}, Δ_{TB}	Threshold for acceptable leading buffer and trailing buffer
Δ_{PET}	Safety threshold for the post encroachment time
ϕ	Azimuth to a target obtained from R and t_r
$\dot{\theta}$	Yaw rate from the yaw rate sensor
$\hat{\theta}$	Heading angle estimate by X-Y Kalman filter
$\hat{\theta}'$	Heading angle estimate by constant speed Kalman filter
$\dot{\hat{\theta}}'$	Yaw rate estimate by constant speed Kalman filter
$\tilde{\theta}, \tilde{\dot{\theta}}, \tilde{\ddot{\theta}}$	Modified angular estimate by angular measurement fusion

Chapter 1
Introduction

1.1 Unprotected Intersection Left Turns at Signalized Intersections

Intersection safety is a major concern in traffic safety. More than one million crashes occurred at intersections in the United States in 2009 and approximately 40 % of them led to injuries or fatalities [1]. Typical intersection crashes are classified into five cases depending on path crossing types: Left Turn Across Path/Opposite Direction, Left Turn Across Path/Lateral Direction, Left Turn Into Path, Right Turn Into Path and Straight Crossing Path [2]. This dissertation focuses on the first type of scenario abbreviated by LTAP/OD, which involves a left turning vehicle and an oncoming through vehicle(s) in the opposing traffic (Figure 1.1). The LTAP/OD crash is the second most frequent path-crossing type crash and accounts for 27 % of intersection path-crossing crashes [3]. If an LTAP/OD scenario occurs with an unprotected (or "permissive") left turn at signalized intersections (Figure 1.1), the left turn vehicle driver must detect the through vehicles, judge their speeds and distances, and select the appropriate timing for making the turn. The main causes of these crashes are believed to be: 1) misjudgment of available gap, 2) misjudgment of the through vehicle speed, 3) failure to detect a through vehicle caused by an obstruction of vision, and 4) failure to detect a through vehicle due to careless oversight ("looked but did not see") [4, 5]. An example driver assistance system for the LTAP/OD scenario and potential design concept are briefly mentioned in Section 1.4.

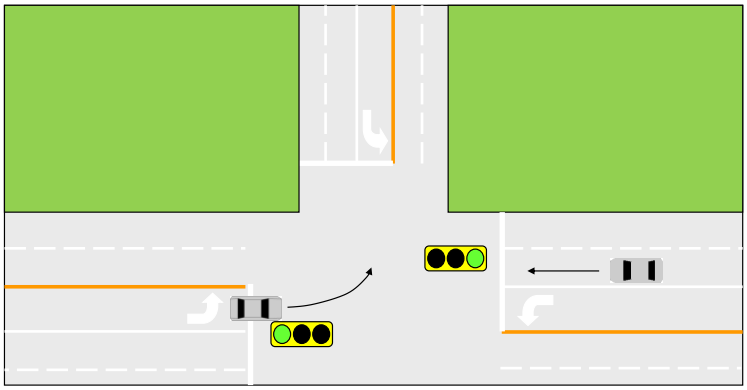

Figure 1.1 Schematic of unprotected LTAP/OD at a signalized intersection.

1.2 Conflict Analysis for Intersection Left Turns

In order to design an efficient intersection left turn assistance system, human drivers' gap acceptance behavior needs to be understood. This is achieved by computing appropriate conflict metrics to quantify such behavior.

Efforts to develop conflict metrics for road traffic safety were begun in the early 1970s [6]. Although it seems obvious that there is a relationship between the number of near-miss cases and the number of accidents, observing such a relationship in a reasonable way is difficult unless near-miss cases are clearly defined since the definition of near-miss can be different depending on individuals [6]. Therefore, conflict metrics are useful to provide objective judgments of conflict level by quantifying near-miss situations.

For the LTAP/OD case, conflict metrics are computed when the left turn vehicle, (subject vehicle, or SV) and through vehicle (principal other vehicle, or POV) are in either one of the following particular vehicle configurations of interest as shown in Figure 1.2. For each of these, a conflict point is defined as being in the encroachment zone, which is the intersection of the areas traced by the vehicles as they proceed. A conflict point is a fictitious collision point if time is delayed or advanced depending on the configuration of the SV and POV by the amount of spare time between those vehicles. Therefore, the conflict point should be defined so that the spare time becomes the shortest. In the LTAP/OD scenarios, two cases are possible depending on the vehicles' configuration.

The first case represents, “the SV crosses the intersection first” before the POV (Figure 1.2(a)) and the second case, “the SV crosses second” (Figure 1.2(b)). In the first case, the conflict point is located at the last point where the SV leaves the encroachment zone and, for the second case, it is found at the first point where the SV arrives at the encroachment zone. Also, note that since the vehicle shapes are assumed to be rectangular, the speed changes of the vehicles are negligible in and near the encroachment zone and the edges of the encroachment zone are approximately linear to make the conflict point always appear on one of the vertices of the encroachment zone. As a result, a conflict point is typically found in the top-right corner of the encroachment zone for the case of the SV crossing first (Figure 1.2(a)) and the bottom-left corner for the other case (Figure 1.2(b)).

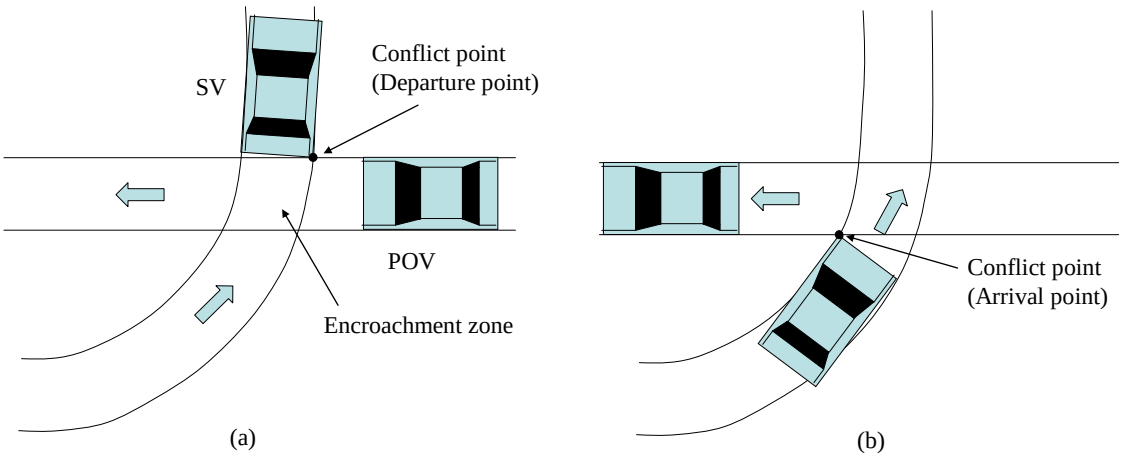

Figure 1.2 Left turn conflict points: (a) subject vehicle crosses first (conflict point is at departure point) and (b) subject vehicle crosses second (conflict point is at arrival point).

Example conflict metrics for the LTAP/OD scenarios are the post encroachment time (PET) [7], gap time (GT) [7, 8], and leading buffer/trailing buffer (LB/TB) [5, 9, 10]. Among these, the PET was originally defined as “…the time from the end of encroachment to the time that the through vehicle actually arrives at the potential point of collision…” [7]. Although this definition solely explains the case of the SV crossing first, it can be enhanced easily for the crossing second case based on Figure 1.2(b). Therefore, the PET is an actual measure of the available gap when the vehicles are in the conflict configuration, and it is defined uniquely for each event. On the other hand, the GT and LB/TB is computed prior to when the vehicles form the conflict configuration. In fact,

these conflict metrics are computed by taking the difference between the times at which the SV and POV reach the conflict point. The only difference between the PET, and GT and LB/TB is that the PET utilizes the actual times when the vehicles are at the conflict point while they are predicted times in the other metrics. This indicates that each of the predictive measures becomes a function of time or position.

Among the predictive conflict metrics, a noticeable difference in the LB/TB from the other conventional ones (e.g. the GT) is the use of a variable reference speed profile for the SV speed prediction, while the GT assumes a constant speed. The variable reference speed profile is expected to overcome the issue of the constant speed assumption in a predictive setting (as required by the assistance system which needs to give a warning before starting to turn left); for example, a predicted gap time between the SV and POV becomes infinite when the SV is stationary at the intersection.

In order to conduct the conflict analyses, vehicle trajectories of LTAP/OD events are necessary and are prepared by reconstructing vehicle trajectories using naturalistic driving data in this dissertation. Trajectories of both the SV and POV in the opposing traffic are reconstructed from field operational test data. There are technical challenges associated with this data from vehicle based sensors that are resolved by multiple use of Kalman filtering. One issue is the heading angle error due to randomly scattered GPS data at slow SV speed. Since POVs are only relatively detected by the forward sensors on the SV, a small heading angle error could result in a large positional error. This is resolved by the constant speed Kalman filter. Another issue is sampling timing errors between different sensors. The latency time difference correction is performed to adjust the time scales in these sensors.

After the trajectory reconstruction is complete, an extensive analysis of conflict metrics is conducted to find the typical gap acceptance behavior of the human driver measured by the PET. Its results suggest basic threshold values to be employed in decision components in the driver model and the design of a left turn assistance system. A left turn assistance system should have a reasonable method to evaluate whether a gap is

acceptable for a left turn and this process involves predictions of future vehicle motion. The LB/TB is adopted for this purpose due to its advantage over the other predictive metrics.

1.3 Modeling the Human Driver for Intersection Left Turns

Early attempts of human driver modeling focused on path tracking based on closed-loop servomechanisms, e.g. quasi-linear model [11, 12], cross-over model [13] and optimal preview control model [14]. A shortcoming of these models is that they assumed a predetermined reference path. On the other hand, a lane keeping model based on reference yaw rate defines no explicit reference path [15]. It was shown that vehicle yaw rate was confined between critical yaw rate envelopes while driving within lane boundaries [16]. Risk is considered as a factor used by the driver to adapt to varying situations. This type of model is called a motivational model [17-19]. Commonly used quantitative measures of risk are time to collision (TTC) [6, 8] and time to line crossing (TLC) [20, 21]. On the other hand, a hierarchical model based on the type of driver behaviors has knowledge-based, rule-based and skill-based behaviors from higher to lower level [22]. In driver modeling, knowledge-based behavior applies when the driver encounters an unfamiliar situation and case-by-case problem solving is required. Rule-based behavior is the application of rules obtained through experience. Skill-based behavior represents automatic reaction within vehicle control. Another hierarchical model distinguishes by tasks, i.e. strategic, tactical (maneuvering) and operational (control) tasks [23]. Strategic task involves planning of travel route, tactical task represents driving maneuvers, and control task is control action to operate the vehicle. The combination of these behaviors and tasks in the hierarchical models indicates the level of proficiency in driving [23, 24]. Moreover, each task involves cyclic information processing which contains selection, processing and action, and the driver is assumed to adjust the vehicle speed so that an available time to complete one cycle becomes larger than the time needed to do it [25, 26].

For intersection left turns, a speed control model dedicated to this type of scenario is especially needed since the vehicle speed tends to vary widely during a left turn. Speed control behavior of human drivers has been researched since the 1950's, but there have not been large and highly detailed data sets from naturalistic driving available until now. Many previous models have focused on traffic flow on highways, headway control and longitudinal dynamics being the main considerations [27-31]. Driving on curved roads or making intersection left turns requires additional consideration due to lateral control. Examples of existing models are based on time-to-lane-crossing (TLC) [21], lateral acceleration margin [32], total acceleration [33], lateral jerk [34], sight distance [35], and stopping distance [36]. However, none of these models can address the driver's need to simultaneously address *multiple* potential outcomes – stopping or turning at an intersection – and hence a new approach has been developed.

Visual and vestibular systems are the most relevant sensory inputs for human drivers [37]. Drivers receive a wide range of information which may affect speed choice, including road geometry (e.g. lane width and curve radius [38-41]), as well as general road conditions [42]. In the scenario of an intersection left turn, the dominant factor during the straight line approach is presumed to be the anticipation of the acceleration required to either make the turn or stop before making the turn. Here, complex behaviors relating to traffic, such as adjusting speed in anticipation of a gap, are not considered. The acceleration "penalty" for turning or braking too quickly (for safety or comfort) places an upper limit on the entry speed, depending on the distance from the turn. It is clear that human drivers learn and adapt their behavior with experience and that only visual information is available for the underlying control reference for speed control on approach to an intersection; of course vestibular and other cues (e.g. vehicle pitch response and brake pedal force) may be useful for modulating the vehicle speed. In this dissertation, the visual reference signal are focused mainly, and while the specific optical or physiological mechanisms involved are not considered, it is sought to make use of variables involving motion and distance that are instantaneously available to the driver and do not require critical knowledge of friction or estimation of stopping distances, etc. As a side note, one reason to support this working hypothesis is that, from experience, the

anticipated “penalty” is equally available to passengers and drivers; even if a passenger is not an experienced driver, they may apply a non-existent “brake pedal” when the approach seems too fast.

In this study, the longitudinal control is developed based on the anticipated acceleration reference (AAR) model which utilizes the directional error between the current heading angle and reference heading angle parallel to the lane boundary. The driver parameters in the AAR model are tuned by fitting the acceleration profile obtained from the simulations to the acceleration from the driving data. For the lateral control, a preview tracking model [43] is adopted which compensates the yaw rate and angle errors. The Monte Carlo simulations are run for various driver parameter values selected from the determined ranges to provide a large number of left turns for designing a left turn assistance system using the MATLAB® Simulink and CarSim® vehicle model.

1.4 Designing a Left Turn Assistance System

In order to avoid LTAP/OD crashes, the assistance system needs to evaluate the conflict level accurately by estimating the future trajectories using the vehicle kinematics at a proper time so that an effective warning signal can be given at a sufficiently distant location from the intersection in order for the SV to stop safely. Three types of intersection collision avoidance system are considered: 1) vehicle-based system, 2) infrastructure-based system, and 3) vehicle-infrastructure cooperative system. As an example of the cooperative system, the Cooperative Intersection Collision Avoidance System for Signalized Left Turn Assist (CICAS-SLTA) [44] focuses on the LTAP/OD scenarios with unprotected left turns at signalized intersections, communicating with the vehicles through the dedicated short range communications (DSRC) [45]. Since signalized intersections with unprotected left turns generally have a larger traffic volume compared to unsignalized intersections on rural roads, making a proper decision to start a left turn is crucial in terms of safety. Assistance system such as the CICAS-SLTA is expected to help the SV driver perform such a maneuver more easily. In addition, this

concept of adding a supporting system to an existing infrastructure can be significantly less expensive than replacing with a new traffic signal with a protecting left arrow [44].

Since the assistance system needs to predict the future conflict in order to provide a warning at the proper time based on the gap acceptance behavior obtained from the conflict analysis, some level of error is unavoidable. Such an error is caused by mismatches between the actual and estimated vehicle trajectories and between actual and estimated speed profiles. Moreover, the level of the error varies depending on values of the system parameters as well (e.g. SV position at which the conflict measure is computed). For example, as the vehicle approaches the intersection, the accuracy of the prediction increases. Of course, the high rate of successful detections of potential conflicts is of a primary interest to achieve, but an overly conservative system design (i.e. a warning signal is issued to a small level of conflict) increases the rate of unnecessary warnings which would cause drivers' frustration and unnecessary change in their driving state. A warning signal is referred to as "true-positive (TP)" if attempting a left turn is predicted as unsafe and making a left turn is actually unsafe. Here, the safety of an event is estimated by comparing the predicted conflict measurement (i.e. LB/TB) with the actual safety threshold represented by a PET value determined from the naturalistic driving data analysis. Similarly, a warning signal is considered as "false-positive (FP)" if it is predicted as unsafe while turning left it is actually safe with no warning provided. P(TP) and P(FP) are used as performance measures in a safety system design [46-50]. Figure 1.3 shows conceptual probability density distributions of the estimated safety level for safe events (right) and unsafe events (left). By comparing the estimated safety level with the threshold, Δ, the assistance system estimates whether an event is safe or unsafe. Due to the estimation error in the estimate, there will be an overlap between the two distributions. P(TP) is defined by the area $(1)\cup(2)$ and P(FP) is the area (2). It is noted that the complementary areas can also be defined, i.e. false-negative, (P(FN) or (3)) and true-negative (P(TN) or the area $(3)\cup(4)$) are complementary to P(TP) and P(FP) respectively. Although it is omitted here, a similar diagram can be made for the LB as well. Since sets of safe and unsafe events are exclusive to each other, $P(\mathrm{TP})+P(\mathrm{FN})=1$ and $P(\mathrm{FP})+P(\mathrm{TN})=1$.

P(TP) and *P*(FP) obtained for various parameter values are often plotted to make a receiver operating characteristics (ROC) curve [46-52]. A typical ROC curve consists of *P*(TP) in the vertical direction and *P*(FP) in the horizontal direction. This is convenient to visualize the trade-off between the two probabilities by a single curve. A schematic of an ROC curve is shown in Figure 1.4. Once an ROC curve is made, an operating point is ready to be selected based on subjective design criteria and corresponding parameter values are found for implementation. Moreover, *P*(TP) and *P*(FP) are affected not only by the selected parameter values but also by inherent characteristics of a system because they determine the shapes and relative location of the distributions. If a system can judge whether an event is safe or unsafe more accurately than another system, the probability density distributions will be more separate. In this case, the ROC curve will be closer to the corner at the (0, 1) coordinates in Figure 1.4. On the other hand, an ROC curve for a less accurate system will shift toward the diagonal line. Of course, the above condition for finding an operating point may be subject to change depending on the design criteria. In fact, the ROC curve is a set of points, each of which is an optimal solution in the sense of the Pareto optimality. A Pareto set can be formed based on the concept of dominance.

Moreover, the SV location at which a warning signal is issued if the system detects a potential conflict affects the rates of successful braking (SB) or unsuccessful braking (UB) to reach rest before entering the intersection. These are defined given a warning signal, or under the condition of TP.

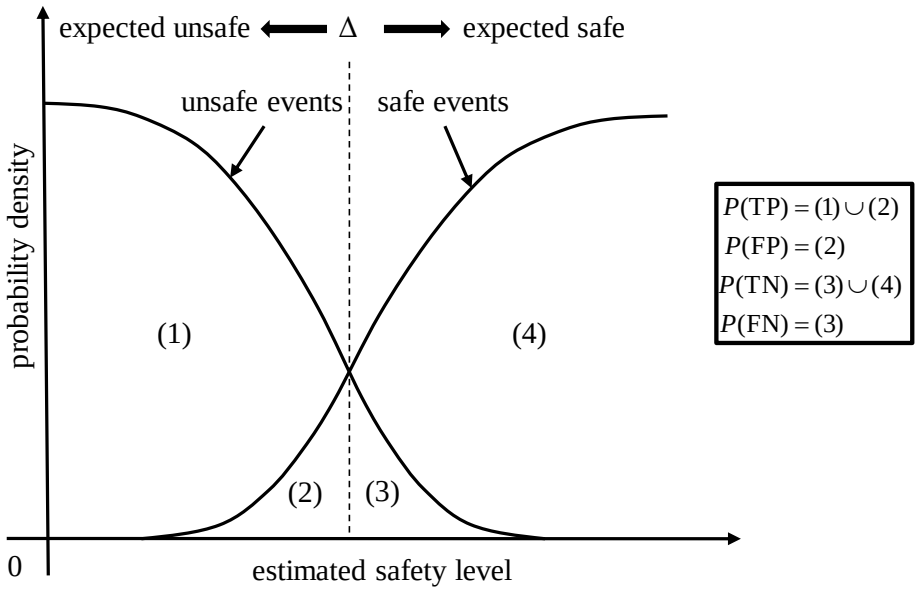

Figure 1.3 Conceptual distributions of conflict estimation.

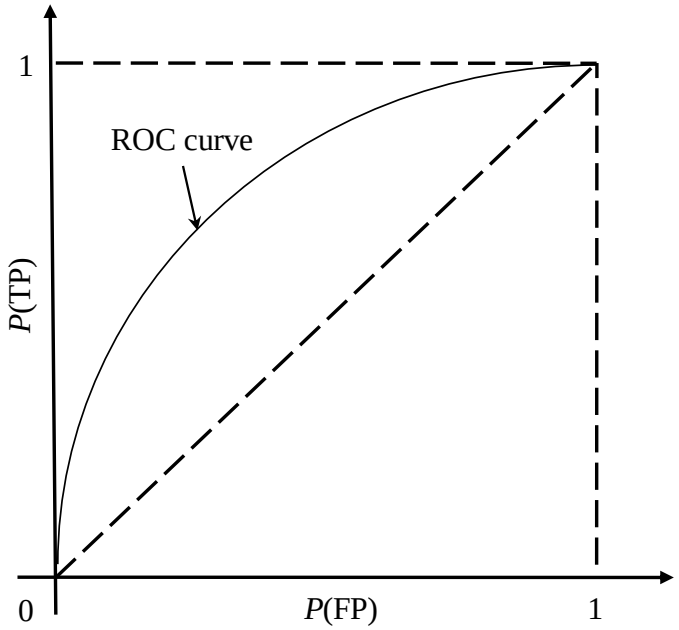

Figure 1.4 Schematic of receiver operating characteristic curve.

1.5 Research Objectives

This research aims to investigate the viability of driver assistance systems to improve the safety of unprotected left turns at signalized intersections. It requires realistic understanding of the nature of the problem to develop a quantitative method for the system design and evaluation of the system. In order to achieve these requirements, naturalistic driving data are used to derive information about the gap acceptance behavior of human drivers. An assistance system should estimate or predict the conflict level before the vehicle starts turning, giving sufficient time to warn the driver in advance. Because of the complex and stochastic nature of the human-in-the-loop system, the test conditions are best suited to a Monte-Carlo simulation approach, where a large number of left turn events are generated to estimate the overall system performance. This is achieved by expanding the available set of left turn events from the driving data using a simulation model. The simulation model is to reflect the driving characteristics of actual drivers, based on the driving data analysis, with special attention given to vehicle speed control during the approach to the intersection; this is because the speed profile has a strong effect on gap timing during a left turn, and hence on the intersection conflict analysis.

The assistance system is to be formulated based on a proposed design methodology to maximize the system performance with an acceptable level of detrimental effects due the trade-offs between the design objectives. Specifically, the following are to be carried out.

1) Trajectory reconstruction

   This is approached by multiple applications of Kalman filtering and measurement fusion to the left turn events found in naturalistic driving data.

2) Conflict analyses

   The post encroachment time (PET) is computed for each left turn event to find the gap acceptance behavior of left turn drivers. A predictive conflict metric (LB/TB) is developed as the predictive measure of the PET by using the variable reference speed profile for the subject vehicle (SV) and constant speed for the principal

other vehicle (POV). The concept of buffer band is introduced for visualization of the safety level given predictive measures and the PET thresholds.

3) Modeling the human driver

   It is crucial to predict the speed profile of the SV accurately for the calculation of the LB/TB. The speed control model for free left turns is developed based on a new concept of *anticipated acceleration reference* (AAR). The AAR is validated for both individual left turn events and the averaged speed of multiple events. For the latter, the Monte Carlo simulations are conducted to prepare a large number of events.

4) Designing a driver assistance system

   An assistance system is designed and evaluated for scenarios where the SV driver "looked but did not see". Monte Carlo simulation makes use of the human driver model, as well as vehicle and other sub-models. Optimal system parameter values are found based on the Pareto optimality.

The dissertation is organized as follows. In Chapter 2, the naturalistic driving data used for the trajectory reconstruction is described, the trajectory reconstruction process is presented in Chapter 3, the conflict analysis procedure is explained in detail in Chapter 4, detailed descriptions of the simulation model, parameter tuning and the result of the Monte Carlo simulations are presented in Chapter 5, an assistance system is designed by using the proposed design procedure which is based on the Pareto optimality in Chapter 6, and conclusions and future topics are summarized in Chapter 7.

Chapter 2
Data Sources

2.1 Naturalistic Driving Data

Candidate LTAP/OD events were obtained from a naturalistic driving database, which was the field operational test for the road departure crash warning system (RDCW-FOT) previously conducted at the University of Michigan Transportation Research Institute (UMTRI) [53]. Although the RDCW-FOT was originally conducted to develop lane departure warning (LDW) and curve speed warning (CSW) systems, these systems did not generate warnings during left turns except for few cases. The vehicle-based data acquisition system (DAS) with approximately 400 data channels installed in the test vehicles (11 of 2003 Nissan Altima 3.5 SE) recorded necessary information for the trajectory reconstruction using a differential GPS (DGPS), vehicle sensors, forward radars for object detection and video cameras. A brief explanation about the RDCW-FOT and the instrumentation of the test vehicles is noted in Appendix A. The RDCW data is considered naturalistic since the test drivers were randomly selected from the general public, were given no guidance from the research staff during driving and no RDCW warning was generated during left turns excluding a small number of cases. Seventy-eight test drivers were recruited from three different age groups: younger (20-30), middle (40-50) and older (60-70). Each age group contained 26 subjects with equal numbers of males and females. The test drivers drove the test vehicles as substitutes for their personal vehicles for 26 days.

Recorded driving data showed that most trips were made in southeast Michigan which consists of seven counties. In this study, two counties were selected for mining left turns for the analysis. Washtenaw County was selected since UMTRI had an intersection

database provided by the county's road commission. In other words, unprotected left turns can easily be distinguished from protected ones by the signal type information. However, the number of left turns was not sufficient for the gap analysis by age and gender groups (Section 4.3.3). Therefore, an additional data source was desired. Oakland County, the second selected county, included a large number of left turns, but signal information was not available. In this case, unprotected left turns had to be identified through manual search using the video data. The detailed procedure is explained in Section 2.2.1.

2.2 Initial Screening of Driving Data

2.2.1 Data Retrieval

To retrieve the left turn event data from the naturalistic driving database, MATLAB® was used to send SQL queries with parameters to identify particular events. Those parameters were Driver #, Trip #, Start time and End time (recorded in centi-seconds) and were chosen from a list of all relevant left turn events detected in the naturalistic driving database. In the figure, SEMCOG ID is a label code that uniquely identifies the individual intersection, and Type represents the type of the intersection's traffic control indicated by either TS (traffic signal) or FL (flashing light). Additional information about whether an intersection of the TS type was protected or unprotected was given in a separate intersection database table (Washtenaw County only).

On the other hand, such intersection data is not available for Oakland County and signal types are known as either signalized or flashing light only. Therefore, whether a left turn was protected or unprotected was determined by video observation for each left turn. If the SV or another vehicle also waiting to turn left in front of the SV crossed the stop bar while POVs were approaching, the left turn was identified as unprotected. It is possible that those left turns are actually filtered cases which mean that the left turn vehicle is not protected until some period of time is passes and a left arrow appears. However, POVs are decelerating or stopped and such cases can be rejected. If POVs did not exist in the camera view and the SV turned, it cannot be confirmed if this left turn was protected or

unprotected. In this case, this event was left open and checked again later after checking all the left turns to see if there were left turns that happened in the same intersection and direction.

Moreover, the retrieved data contained necessary variables to reconstruct the SV and POV trajectories sensed by the GPS, motion sensors and forward radars. Each left turn event was manually examined to test if it had an appropriate time range for the conflict metric analyses. The Start and End times were previously found automatically via SQL queries of turning motions. For analysis here, the retrieved data was extended by ten seconds before the Start time and after the End time, mainly to improve the latency time estimations between variables from different onboard modules.

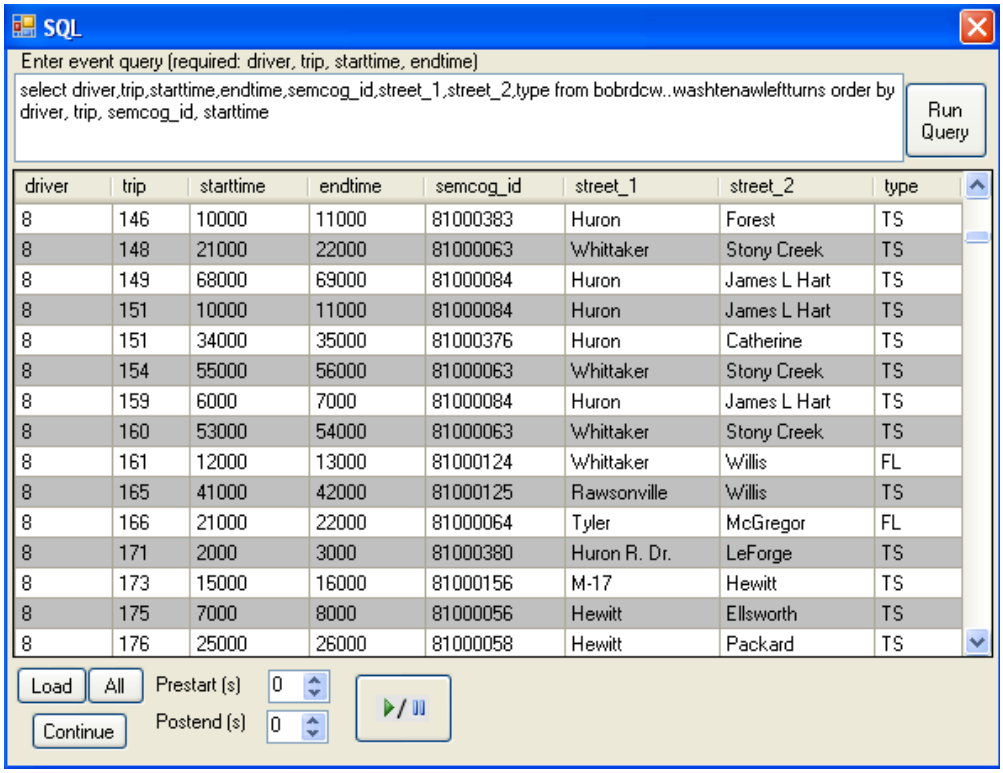

Figure 2.1 List of left turn events in the naturalistic driving database.

2.2.2 Variable Selection for Trajectory Reconstruction

In order to reconstruct the vehicle trajectories, kinematic variables must be obtained by either directly accessing desired variables or deriving ones from retrieved variables. In order to obtain the best results, the most suitable set of variables were to be determined before beginning reconstruction of the trajectories. Variables required for absolute location of the vehicle were position and heading angle, and for the SV the only direct measurement was via GPS, which included differential correction.

The differential correction of the GPS was from a regional rather than a local base station and absolute positional accuracy had a margin of error of less than 1m (Table A.5), which is accurate enough for the SV trajectory reconstructions (0.1 s error for 10 m/s) for the conflict analysis. However, the random errors due to noise inherently present in GPS data is undesirable. For this purpose, a standard Kalman filter was adopted; this is advantageous because velocity and acceleration estimates are determined directly from the filter. In the SV trajectory reconstruction process, the accurate heading angle of the SV was considered crucial to maintain the relative orientations of the SV and POV; otherwise, the error (increasing in proportion to the distance between the two vehicles) would cause a distorted POV trajectory, since the POV motion was available only relative to the SV. There were three options for finding the SV heading angle: 1) recorded GPS heading angle directly available in the database, 2) on-board yaw rate sensor $\dot{\theta}$ to be integrated, and 3) multiple angular measurement sources, including the Kalman filter generated trajectory.

The first choice had a significant defect due to a truncation in the speed range of less than 5 m/s – see Figure 2.2. For the second option, simple integration of the yaw rate creates a smooth curve but requires additional information for the initial heading, and is likely to cause an absolute drift error which accumulates as the integration time increases. Therefore, the third option, angular measurement fusion to fuse GPS and inertial sensor (INS) measurements is commonly practiced for vehicle tracking purposes [4, 44, 54, 55]. In fact, it actually performed the best among these three options. A procedure for the application of the angular measurement fusion is described in Section 3.2.4.

The kinematic variables available from the radar, used to generate the POV trajectory, were range R, range-rate $\dot{R}$ and lateral offset t_r. In addition, longitudinal acceleration a_x and lateral acceleration a_y collected from the onboard accelerometer were retrieved from the database in order to validate the heading angle of the SV resulting from the angular measurement fusion. Table 2.1 summarizes the sets of variables used in the process of reconstructing the SV and POV trajectories.

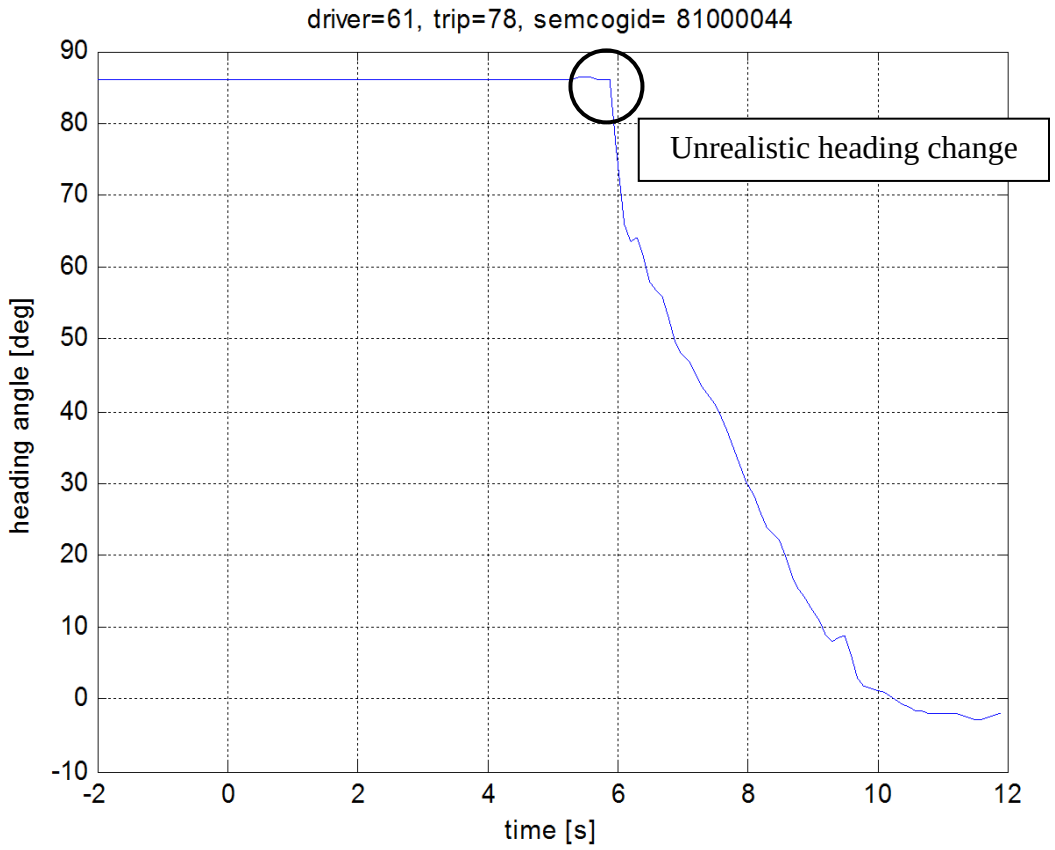

Figure 2.2 Inaccurate GPS heading angle.

Table 2.1 Variables retrieved for the trajectory reconstruction process.

Vehicle	Variables for trajectory reconstruction	Variables for validation
SV	X, Y, $\dot{\theta}$	a_x, a_y, $\dot{\theta}$
POV	R, $\dot{R}$, t_r	

The sampling rates of these variables were 10 Hz for (X, Y) and $\dot{\theta}$, and 20 Hz for $(R, \dot{R}, t_r)$ and (a_x, a_y). However, the sampling rate for the GPS was slower – the GPS data were updated at 4 Hz and in a way that was not fully synchronized with the other variables so that the GPS samples, while recorded at 10 Hz, typically stayed constant for 2 or 3 time steps. This fact (due to GPS clock update limitations) motivated the use of a time varying Kalman filter for those variables with varying time steps.

2.2.3 Selection and Fine-Tuning of Left Turn Events

Candidate left turn events were selected through a screening and tuning process as shown in the screenshot below – Figure 2.3. In the naturalistic driving database, the radar data were sometimes unavailable due to, for example, device limitations and malfunction in a specific test vehicle during a specific test period, and it also happened that a constructed SV trajectory was corrupted due to excessively noisy GPS data; such turning events were not considered amenable to analysis and were also removed from the candidate left turn event set. Moreover, the established list of turning events in the naturalistic driving database sometimes do not contain real left turn events – e.g. a sharp curve in the road was being negotiated. In addition, the RDCW system occasionally gave a warning to the driver during a left turn, and the driving behavior would not be representative, so such cases were excluded. Figure 2.4 shows examples of the three problematic cases: (a) corrupted trajectory due to large errors in the GPS data, (b) improperly assigned time range, and (c) non-left turn case. The stars indicate the trajectories for the period of time of an event and the solid lines show the trajectories in a time range with the extra 10 s for both the Start time and End time.

As mentioned earlier, the time range between the Start time and End time could be modified from the original one. These times were checked visually for each left turn event and, if necessary, adjusted manually so that the trajectory was fully included within the time period. Criteria for proper time range were: 1) the trajectory was to start and end at small values of yaw rate, 2) the lowest speed before the turn was to be included and 3) any following or previous turn was to be excluded where necessary. Note that even if an original pair of the Start time and End time of a left turn event was changed to different

values, it was specified by the original times along with the other numbers, Driver # and Trip #, to fully identify the event in the initial event table shown in Figure 2.1.

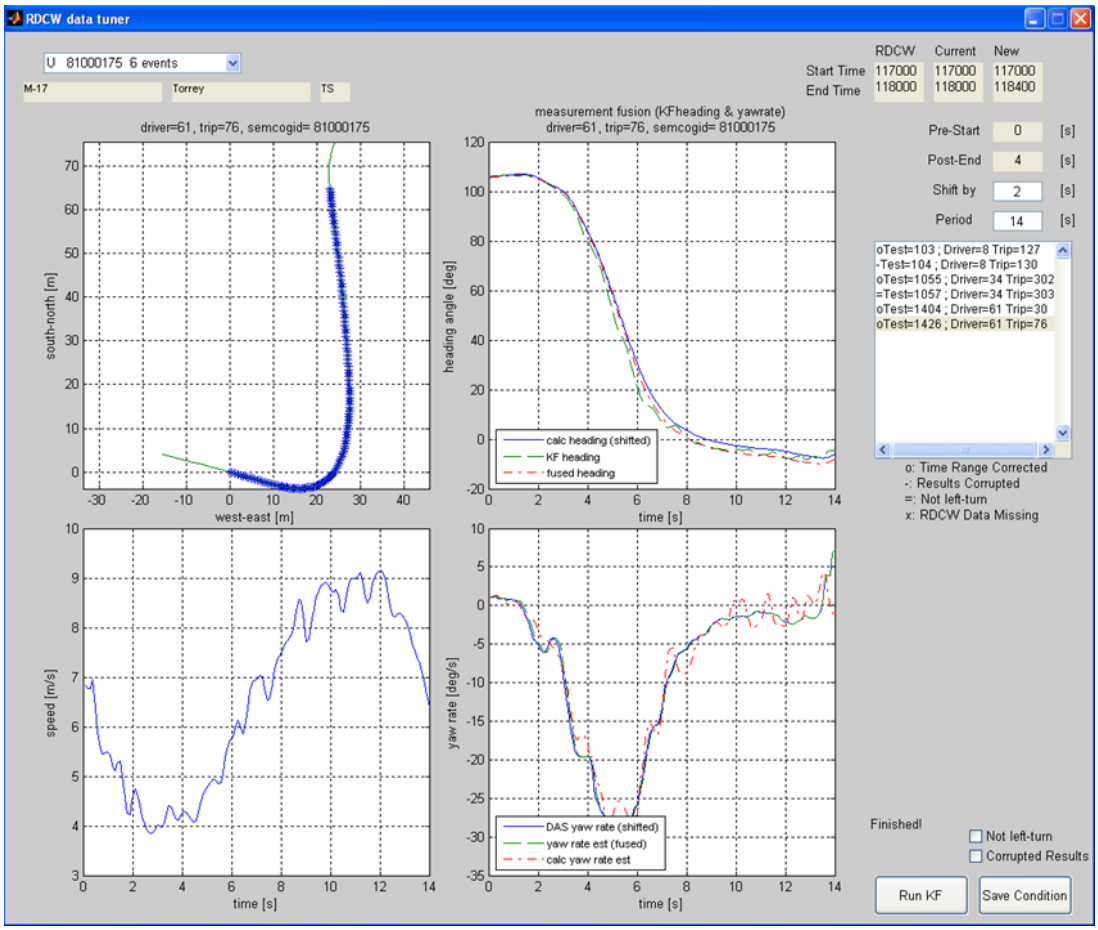

Figure 2.3 Screenshot of event screening process.

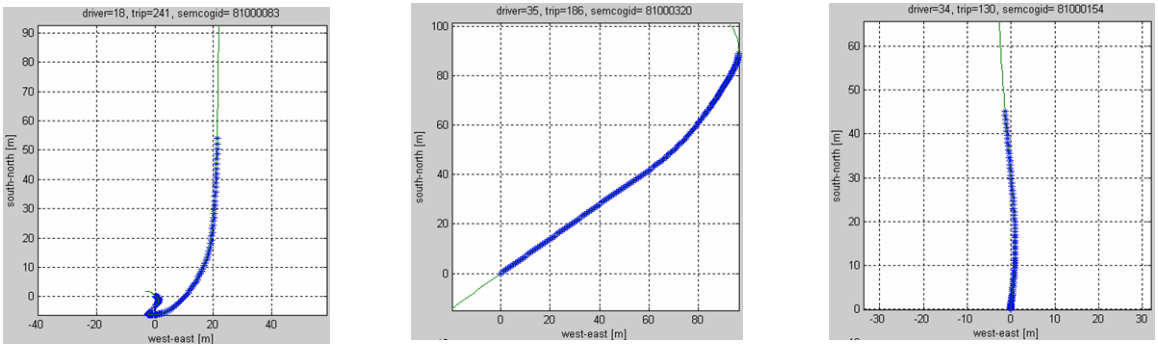

(a) Corrupted trajectory (Discarded)

(b) Improper time range (Corrected)

(c) Not a left turn (Discarded)

Figure 2.4 Examples of inappropriate cases to be corrected or removed.

2.2.4 Summary of Left Turn Events in the Driving Database

The tables below show summary information about all detected left turns in the naturalistic driving database after the initial data checks and screening were performed as mentioned in the last section. The initial set of left turns was detected via a simple algorithm based on vehicle kinematics: first each quadrant with a horizontal axis in the west-east direction and a vertical axis in the south-north direction was quantized. Then, if the heading angle of the SV changed from one quadrant to another in counterclockwise direction, the motion was considered as a candidate left turn. These events were then matched to locations in the intersection database for Washtenaw County or confirmed in the video data to generate the initial candidate left-turn set. More than 70 % of all these left turns are valid for the trajectory reconstruction (Table 2.2), 60 % of the intersections are provided with unprotected signals (Table 2.3) and 50 % of all the left turns detected were unprotected left turns (Table 2.4). It should be noted that the number of left turns found in Oakland County is much smaller than those in Washtenaw County because the type of left turns (i.e. protected or unprotected) in Oakland County was determined by using detected POVs in the video, whereas this was achieved by using the intersection database for Washtenaw County.

Table 2.2 Summary of left turns.

	Number of left turns			Percentage
	Washtenaw	Oakland	Total	
Valid left turns	1191	664	1855	70.7
Corrupted results	116	59	175	6.7
Non-left turn events	149	240	389	14.8
Left turns but data missing	115	85	200	7.6
RDCW warning on	5	0	5	0.2
Total	1576	1048	2624	100

Table 2.3 Types of intersections.

Intersection type	Number of intersections			Percentage
	Washtenaw	Oakland	Total	
Unprotected	199	209	408	61.0
Protected	108	118	226	33.8
Flashing light	35	0	35	5.2
Total	342	327	669	100

Table 2.4 Types of left turns.

Intersection type	Number of left turns			Percentage
	Washtenaw	Oakland (with POV)	Total	
Unprotected	594	173	767	53.2
Protected	476	38	514	35.7
Stop sign/Flashing light	92	1	93	6.5
Unknown	29	38	67	4.7
Total	1191	250	1441	100

Chapter 3
Trajectory Reconstruction

3.1 Overall Procedure and Kalman Filtering

3.1.1 Variable Selection

The primary sensor for the SV trajectory reconstruction was the GPS position (*X*, *Y*). The yaw rate $\dot{\theta}$ from the yaw rate sensor was also used to fuse with the heading angle obtained from the GPS to improve the SV heading angle. For the POV, target point information such as range *R*, range rate $\dot{R}$ and transversal distance t_r (to derive azimuth ϕ) measured by the forward radars was used (see Table 2.1). Since the GPS data was given in geographic coordinates, it needed to be transformed into Cartesian coordinates by projecting onto a plane tangent to the globe at the initial SV position. In addition, the forward camera was used for manual review and the face camera could be used to receive contextual information for manual review. In fact, the heading angle was available directly from the GPS in the naturalistic driving database, but its value was held constant when the vehicle speed became slower than 5 m/s and moreover the time history is not smooth through the whole time range due to noise from the GPS. As a result, this became a significant issue for accurate trajectory reconstructions especially for POVs, since they were detected relatively to the SV. This problem was resolved by using the constant speed Kalman filter and angular measurement fusion.

3.1.2 Flowchart of the Analysis

Figure 3.1 shows a flowchart of the overall process performed in the trajectory reconstruction and conflict metric analysis. It contains four major tasks: data retrieval

from the naturalistic driving database, reconstruction of SV trajectories, reconstruction of POV trajectories and computation of the conflict metrics.

Several types of Kalman filters were used for the trajectory reconstructions in components labeled (1), (2), (4) and (9). Standard (or X-Y) Kalman filters are used in (1), (2) and (9). For (2), source data was modified before the X-Y Kalman filter was applied (constant speed Kalman filter). A measurement fusion was achieved in (4) by fusing $\hat{\theta}$ and $\dot{\theta}$.

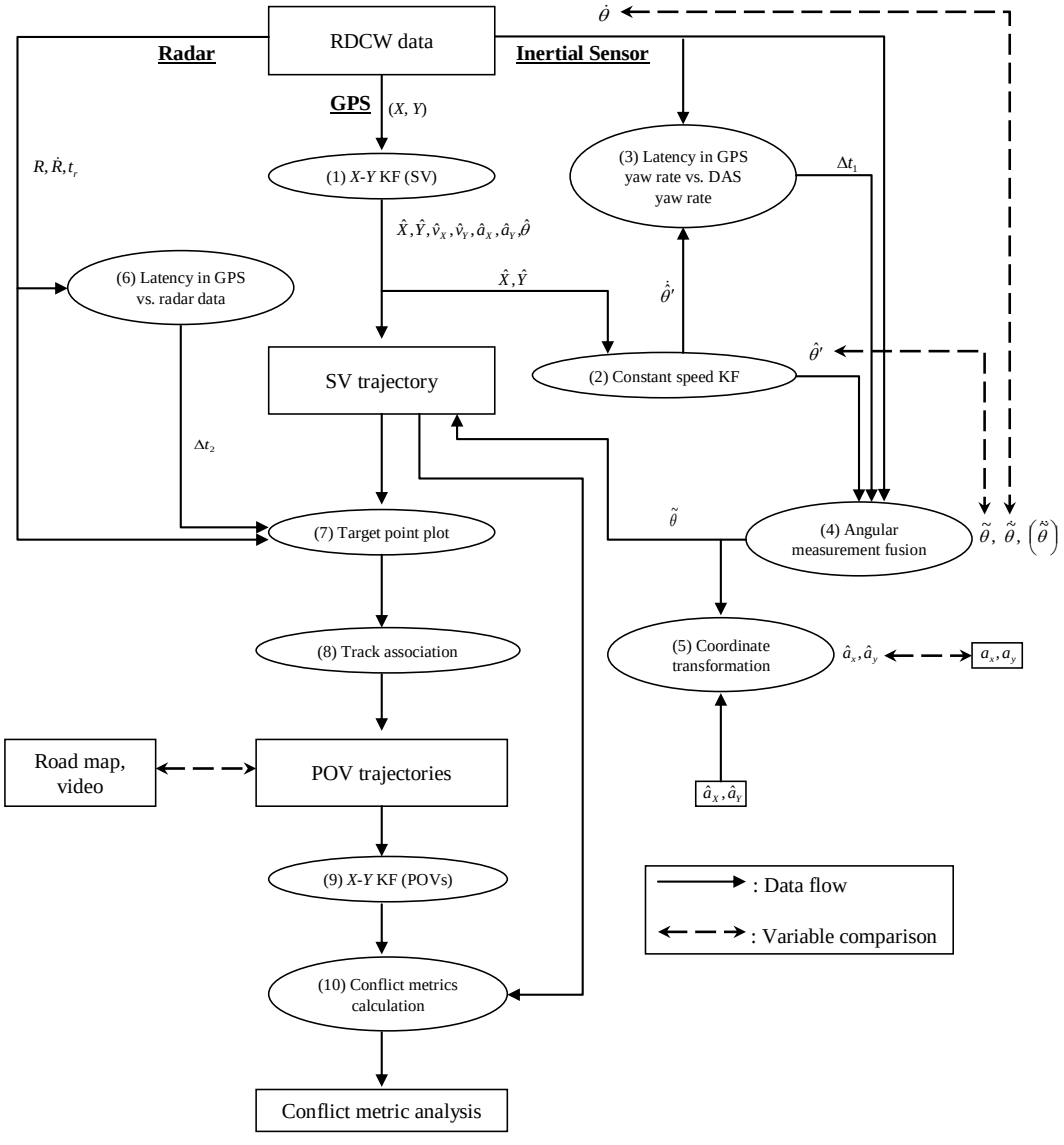

Figure 3.1 Flowchart of the conflict metric analysis.

The sampling rates of these variables were 4 Hz for (*X*, *Y*), 10 Hz for $\dot{\theta}$, and 20 Hz for $\left(R, \dot{R}, t_r\right)$ and $\left(a_x, a_y\right)$. Due to a lack of synchronization between the sampling rate of the DPGS (4 Hz) and the recording rate of the data acquisition system (DAS) (10 Hz), varying time steps were utilized. Alternatively, if more data points were needed, an integration scheme would be used for time update for when the GPS data were missing [54, 55], but in our analysis the GPS sampling rate is considered fast enough for the conflict metrics analysis.

3.2 Trajectory Reconstruction for Subject Vehicles

3.2.1 X-Y Kalman Filter

Of three slightly different types of Kalman filters used in the trajectory reconstruction, the basic concepts adopted, such as Wiener process acceleration model, varying time step and backward sweep before forward sweep are employed in each of them. A common structure of such Kalman filters is summarized in Appendix C.

The first Kalman filter is applied to (*X*, *Y*) in order to obtain position, velocity and acceleration estimates of the SV. The obtained states are denoted, $\hat{X}, \hat{Y}, \hat{v}_X, \hat{v}_Y, \hat{a}_X$ and $\hat{a}_Y$. This result has revealed that the position estimate error is negligible in the high speed region. The filter smoothes speed and acceleration, but there appears to be a slight time delay in the acceleration estimate. However, the overall results indicate a high level of correlation between the direct measurements from the speed sensor and accelerometer compared to those estimated from GPS measurements.

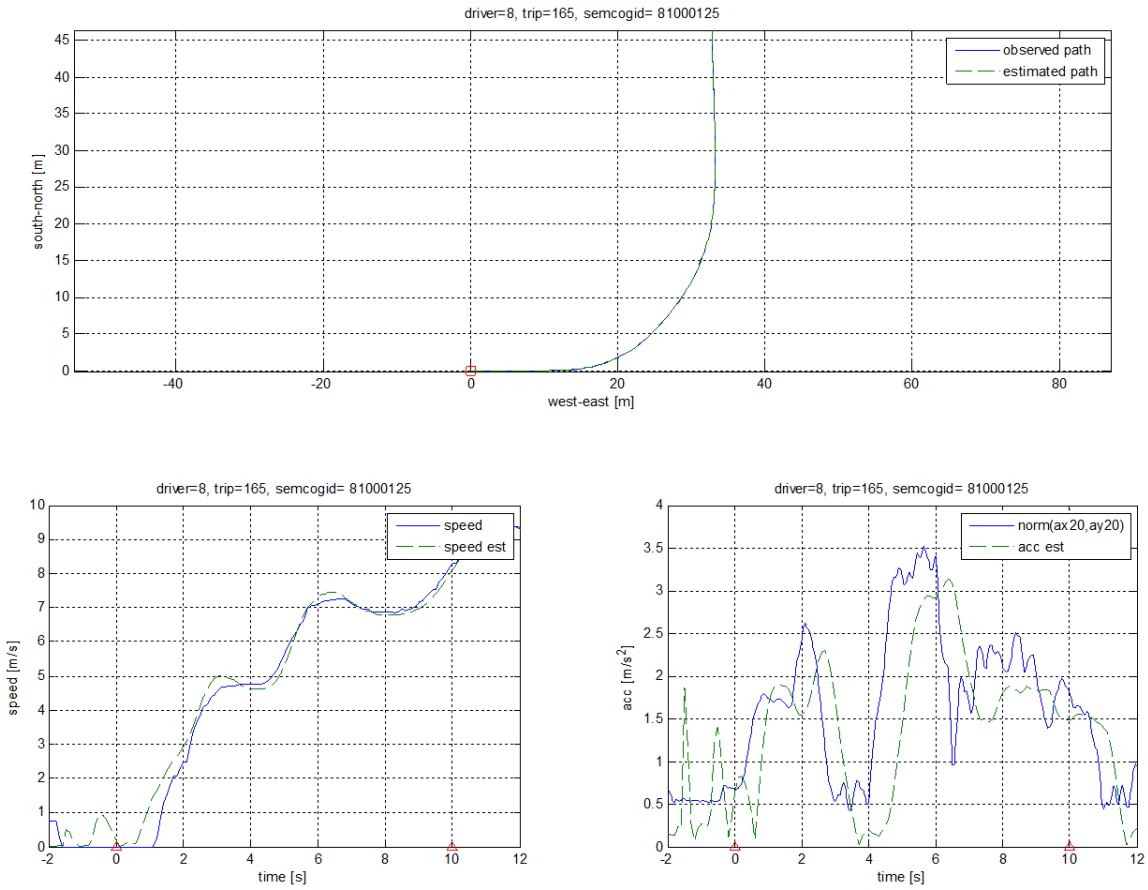

Figure 3.2 Results of the X-Y Kalman filter for the subject vehicle: trajectory (top), speed (bottom-left) and acceleration magnitude (bottom-right).

3.2.2 Constant Speed Kalman Filter

Although the trajectory estimation looks good on a large scale, estimating yaw angle $\hat{\theta}$ from the velocity estimate $(\hat{v}_X, \hat{v}_Y)$ causes a large heading error whenever vehicle speed is low – at low speed the following equation, used for the estimate, becomes ill-conditioned:

$$\hat{\theta} = \tan^{-1} \frac{\hat{v}_Y}{\hat{v}_X}. \tag{3.1}$$

As a result, a raw vehicle trajectory tends to possess a dense cluster of points in a small area, with values dominated by small errors.

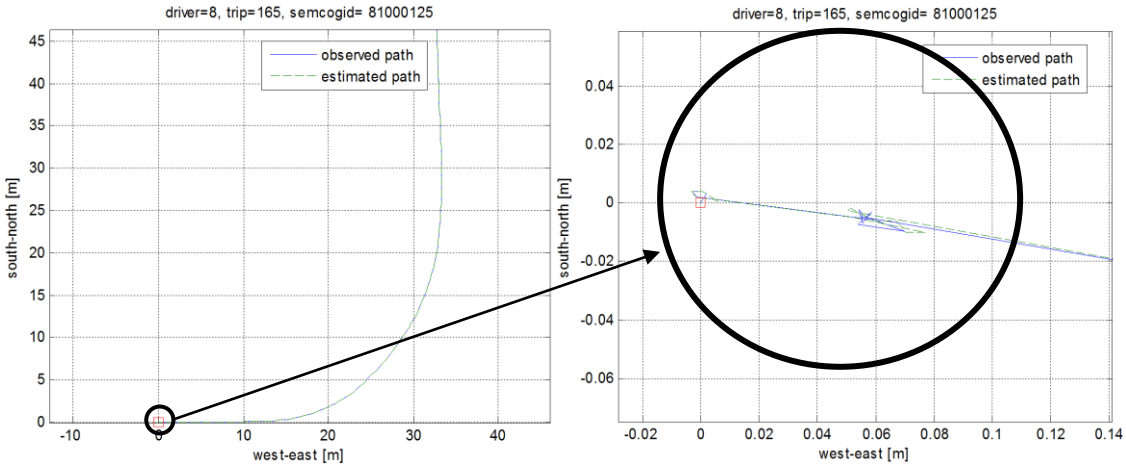

Figure 3.3 Corrupted trajectory due to the low subject vehicle speed.

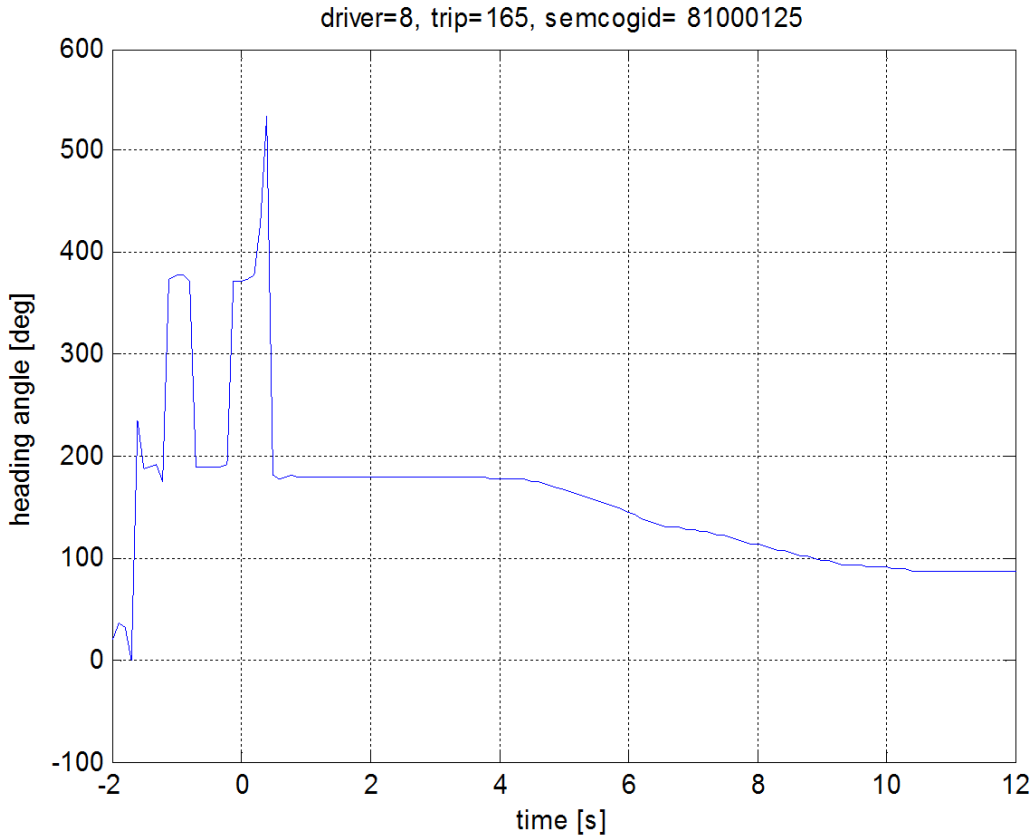

Figure 3.4 Heading error due to the low subject vehicle speed.

The "constant speed Kalman filter" is used to resolve this issue by assuming the vehicle moves at a constant speed on the left turn path. Essentially, this creates equally spaced points (e.g. 1 m apart between two adjacent points) to remove any cluttered dense regions (Figure 3.5 (a)). A fictitious time domain is used to run a constant speed vehicle which is

also equally spaced (e.g. 0.1 s of intervals). Then, using Equation (3.1) a new heading angle can be made. Consequently, after recovering the real time domain, the improved heading angle $\hat{\theta}'$ is obtained (Figure 3.5(b)). Figure 3.6 shows the speed estimate of the constant speed Kalman filter.

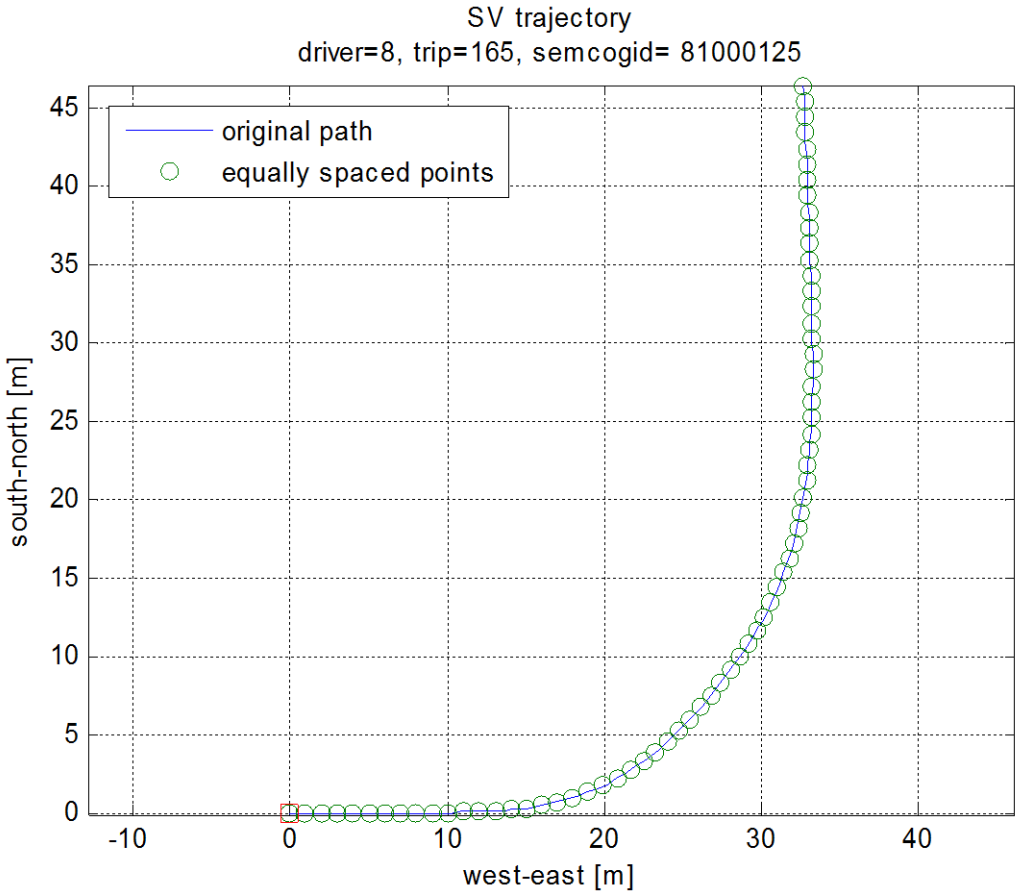

(a)

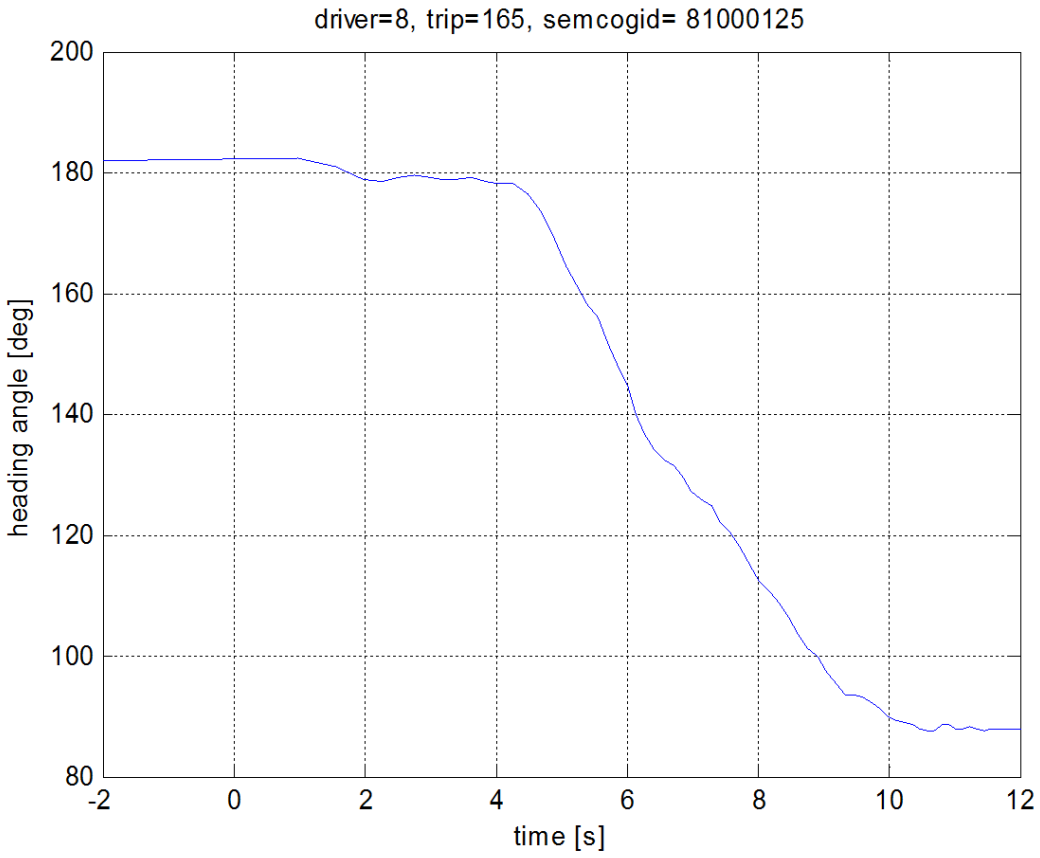

(b)

Figure 3.5 (a) Equally spaced points to avoid the heading error and (b) resulted improved heading angle.

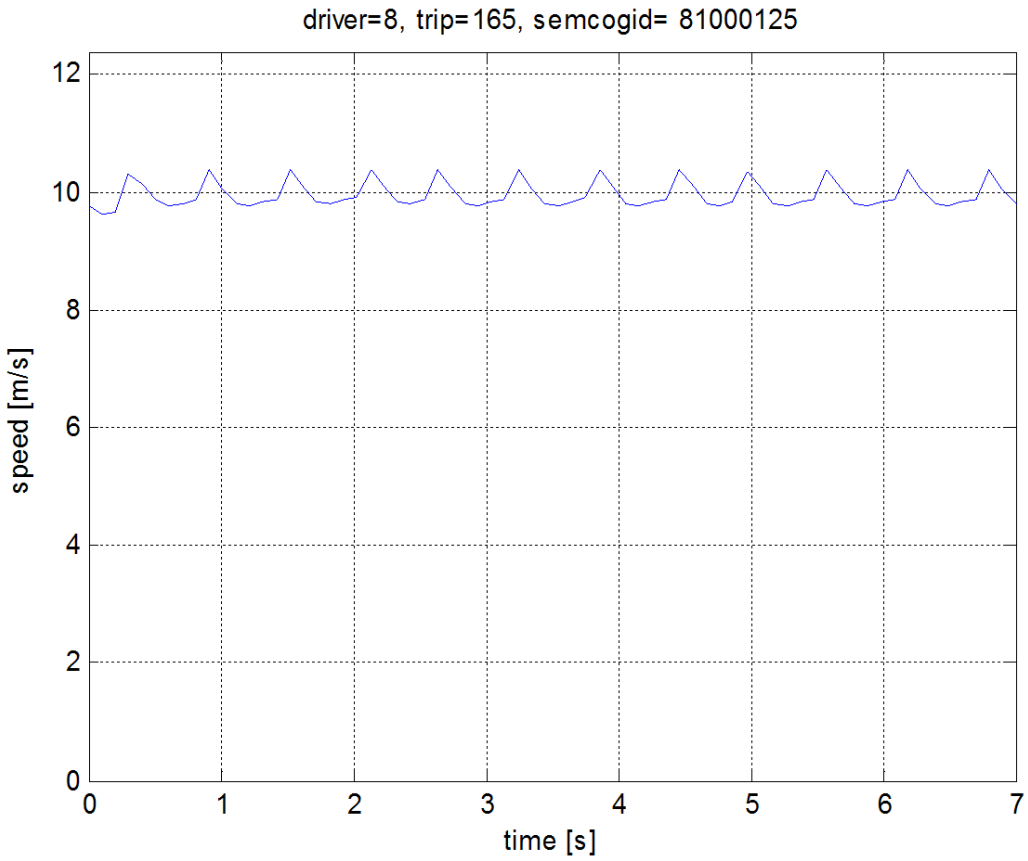

Figure 3.6 Speed estimate obtained from filtering the equally spaced trajectory in the fictitious time domain.

3.2.3 Latency Time Difference between the GPS and DAS

Due to different modules used in the data processing for the GPS and DAS, $\hat{\theta}'$ (GPS-based) and $\dot{\theta}$ (yaw rate sensor), which are the measurements selected to be fused for further heading angle improvement, contain distinct latency times. Therefore, the difference between these times (Δt_1) needs to be estimated and $\dot{\theta}$ is to be shifted by Δt_1 to align both variables, i.e. the GPS time is used as datum time domain.

The yaw rate is first derived from $\hat{\theta}'$, based on the fact that the curvatures of the SV path are the same for both of the fictitious and real time scales. Thus, $\dot{\hat{\theta}}'$ is given by,

$$\kappa = \frac{\dot{\hat{\theta}}'}{\hat{U}} = \frac{\dot{\hat{\theta}}_{const.speed}}{\hat{U}_{const.speed}} \qquad \Rightarrow \qquad \dot{\hat{\theta}}' = \frac{\hat{U} \cdot \hat{a}_{y,const.speed}}{\hat{U}^2_{const.speed}} . \tag{3.2}$$

Then, Δt_1 is calculated by minimizing a cost function, that is,

$$\min_{\Delta t_1} \; f = \sum_{k=1}^{N} \left\{ \dot{\hat{\theta}}'(t_k) - \dot{\theta}(t_k - \Delta t_1) \right\}^2 , \tag{3.3}$$

where N is the number of sampling points in the left turn event.

In the example event, the time shift between the GPS yaw rate, $\dot{\hat{\theta}}'$, and the DAS yaw rate, $\dot{\theta}$, was 0.45 s by which $\dot{\hat{\theta}}'$ was delayed. By choosing the GPS time as the reference time, $\dot{\theta}$ was shifted by that amount to the right as shown in Figure 3.7.

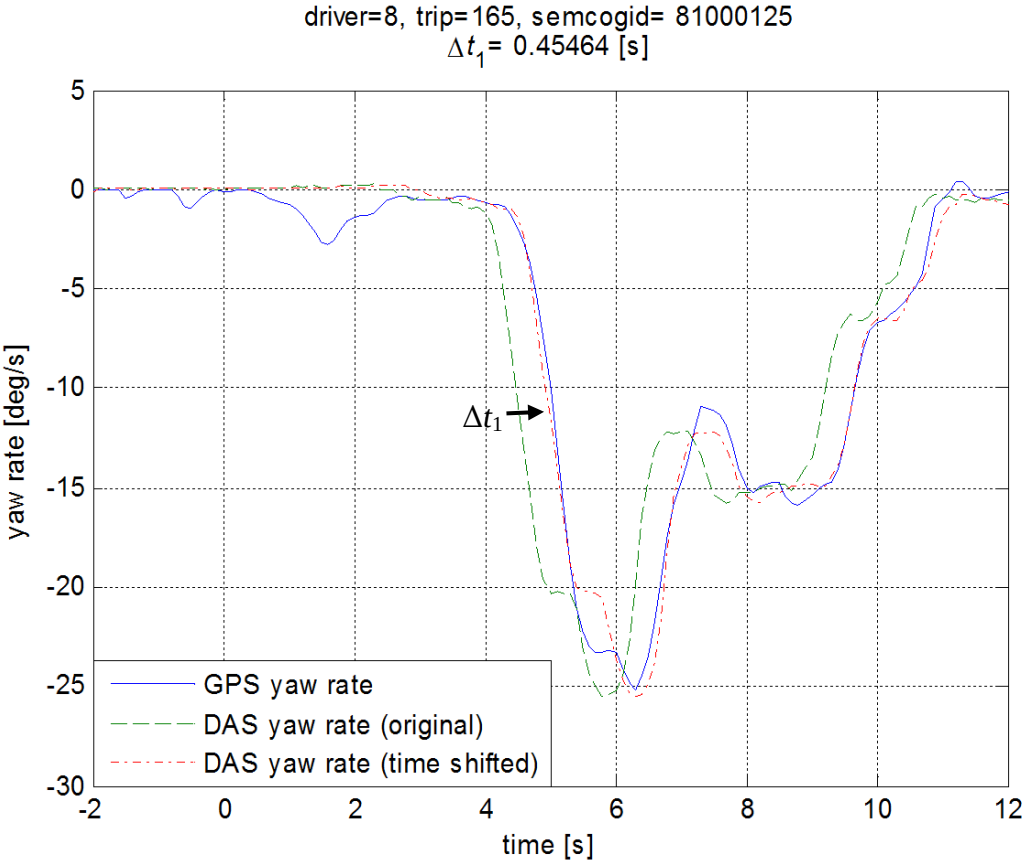

Figure 3.7 Result of the latency time estimation.

3.2.4 Angular Measurement Fusion

The motivation behind the fusion process is that the GPS always gives an absolute position over the entire time range but tends to contain undesirable noise, while the yaw rate sensor gives a smooth curve but with a drifting error when it is integrated over time. The fusion is to provide a pooled estimate that improves either sensor used in isolation. The measurement fusion has been adopted here because of its superior performance to the state variable fusion with a smaller covariance [56].

Fusion starts with the measurements $\hat{\theta}'$ and $\dot{\theta}$ and the Wiener process acceleration model is again used for the angular motion in discrete-time as shown below:

$$\mathbf{x}(k)=\begin{Bmatrix}\phi(k)\\ \dot{\phi}(k)\\ \ddot{\phi}(k)\end{Bmatrix},\ \mathbf{A}(k)=\begin{bmatrix}1 & T(k) & \frac{T(k)^2}{2}\\ 0 & 1 & T(k)\\ 0 & 0 & 1\end{bmatrix},\ \mathbf{G}(k)=\begin{bmatrix}\frac{T(k)^2}{2}\\ T(k)\\ 1\end{bmatrix},\ \mathbf{y}(k)=\begin{Bmatrix}\hat{\theta}'(k)\\ \dot{\theta}(k)\end{Bmatrix},$$

$$\mathbf{C}=\begin{bmatrix}\mathbf{C}_{KF}\\ \mathbf{C}_{DAS}\end{bmatrix}\ \text{and}\ \mathbf{w}=\begin{Bmatrix}w_{KF}\\ w_{DAS}\end{Bmatrix}. \tag{3.4}$$

The components of the measurement matrix **C** are $\mathbf{C}_{KF}=\begin{bmatrix}1 & 0 & 0\end{bmatrix}$ and $\mathbf{C}_{DAS}=\begin{bmatrix}0 & 1 & 0\end{bmatrix}$ [57]. The fused measurement noise covariance is **R**=diag(**R**$_{KF}$, **R**$_{DAS}$) where **R**$_{KF}$ and **R**$_{DAS}$ are the individual measurement noise covariance. In Figure 3.8, it can be seen clearly that $\hat{\theta}'$ has been smoothed by the measurement fusion, particularly at the beginning of the event. More importantly, the time rate of change of these signals is consistent with the yaw rates measured on the vehicle.

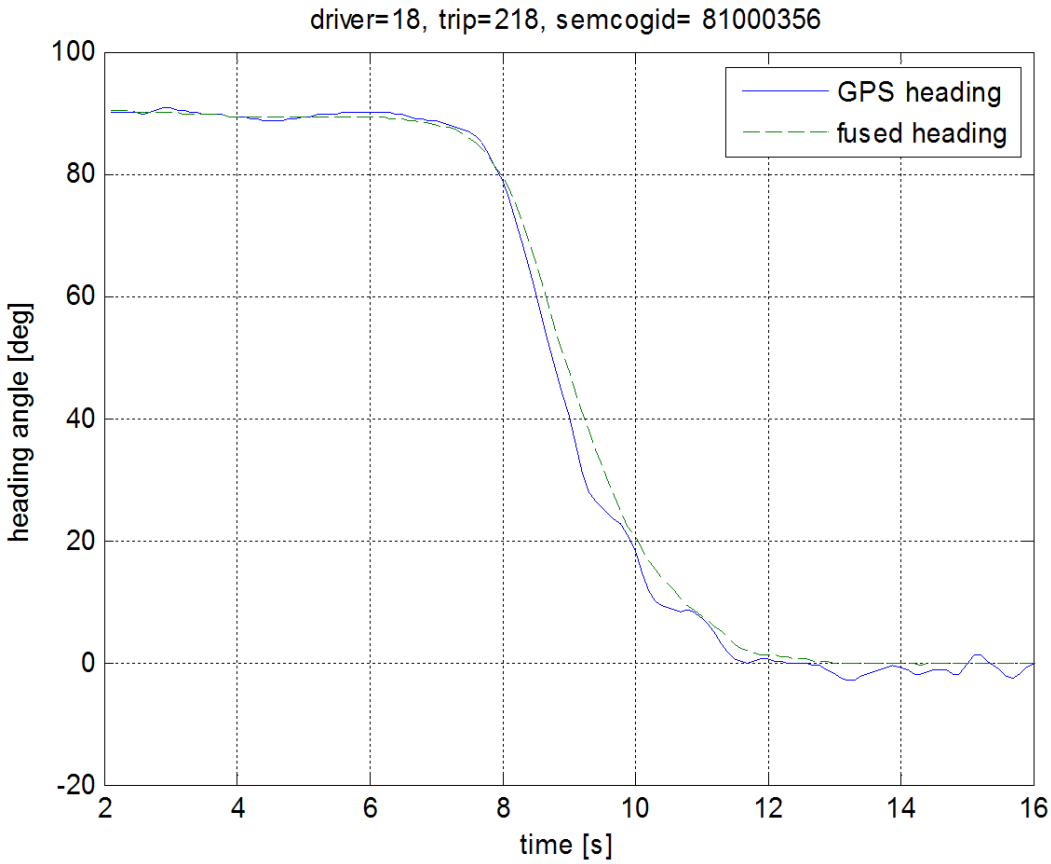

Figure 3.8 Smoothed heading after the angular measurement fusion.

3.2.5 Validation of the Fused Heading

As in the first part of the validation process, the fused heading angle, $\tilde{\theta}$, was examined by comparing it to the GPS-based heading, $\hat{\theta}'$, along with a comparison of the fused yaw rate, $\dot{\tilde{\theta}}$, with the DAS yaw rate, $\dot{\theta}$. As the second part, an independent validation was based on the resolved acceleration components $(\hat{a}_x, \hat{a}_y)$ being compared with those obtained directly from the vehicle-based sensor (a_x, a_y). In this second case, $\tilde{\theta}$ was required to transform $(\hat{a}_X, \hat{a}_Y)$ in the global coordinate system into $(\hat{a}_x, \hat{a}_y)$ in the local one.

Figure 3.9(a) shows that the mean error in $\tilde{\theta}$ vs. $\hat{\theta}'$ was 0.54 degrees and the standard deviation was approximately 2 degrees. The largest deviation occurred while the SV was

turning. In the worst case scenario, the error might be fully attributed to the estimation of $\tilde{\theta}$ in the measurement fusion process, e.g. because of noisy data in the GPS. It is highly unlikely that the errors are all due to $\tilde{\theta}$ but this does give a reasonable upper bound on the errors in the estimated heading angle. In any case, the remaining errors in the heading angle estimate will have some effect on the POV trajectory. As mentioned later, some further refinement of the POV trajectory will also be possible: the speed of the POV can be improved by using $\dot{R}$ measurements and a wrongly directed heading angle for the POV can be corrected by using an appropriate extrapolation method in order for the POV trajectory to reach the intersection for reasonable results from the conflict metrics. In terms of the lateral position error, the deviation would be about 3.5 m for 2 degrees of heading error for the POV located 100 m away from the SV. At this stage we believe the heading angle estimates are as accurate as can reasonably be constructed from the available data. The following figures show examples of heading angle and yaw rate comparisons.

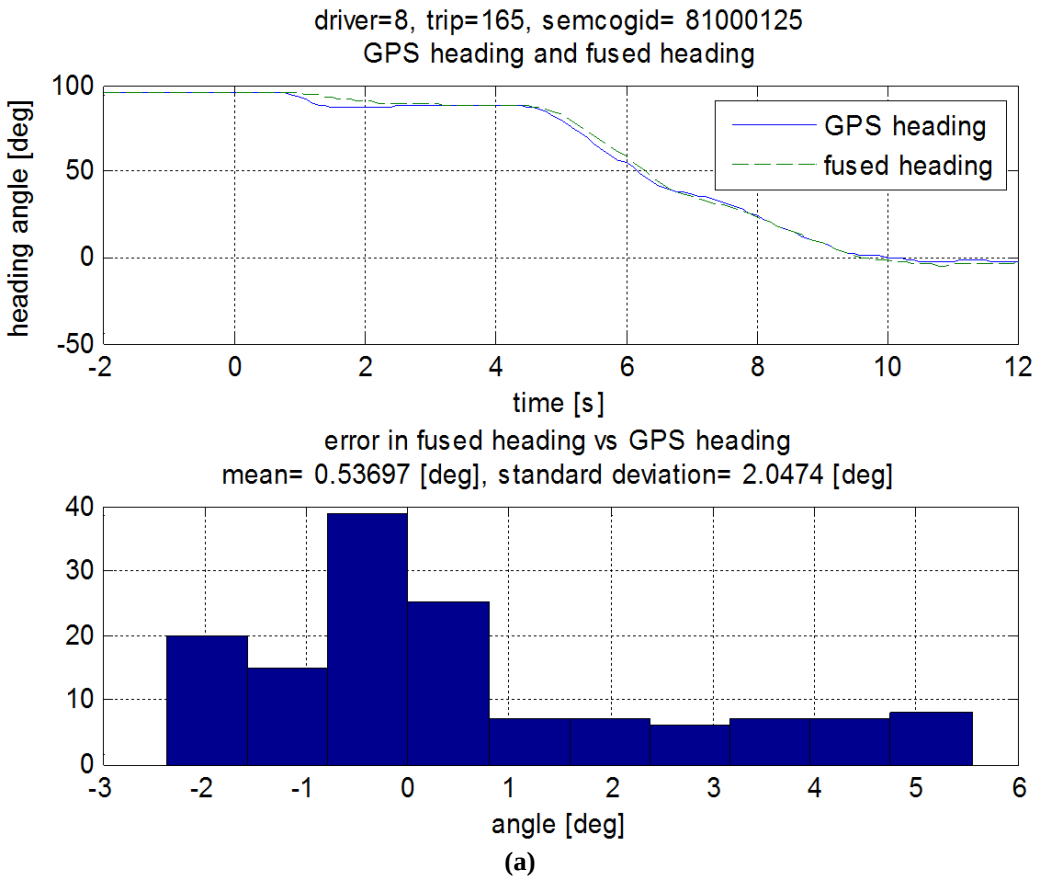

(a)

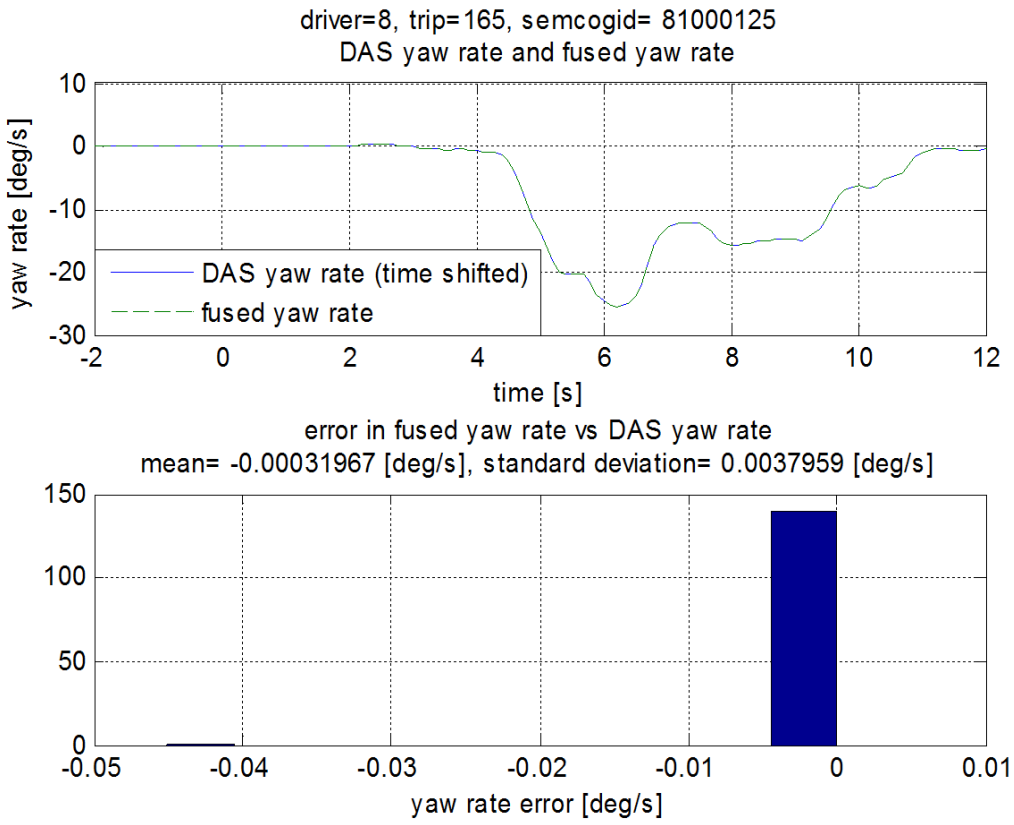

(b)

Figure 3.9 Comparisons of (a) fused heading vs. GPS heading (b) fused yaw rate vs. yaw rate from yaw rate sensor.

For further validation, the coordinate transformation from the global to local coordinate system was achieved by,

$$\begin{Bmatrix} \hat{a}_x \\ \hat{a}_y \end{Bmatrix} = \begin{bmatrix} \cos\tilde{\theta} & \sin\tilde{\theta} \\ -\sin\tilde{\theta} & \cos\tilde{\theta} \end{bmatrix} \begin{Bmatrix} \hat{a}_X \\ \hat{a}_Y \end{Bmatrix}. \tag{3.5}$$

Figure 3.10 shows that the coordinate transformation results reasonably represent each component of the SV acceleration. For the lateral components, it can be recognized that a_y was biased by about 0.5 m/s^2 which might be a calibration error or the result of cross-slope (since the SV was at rest in the beginning period).

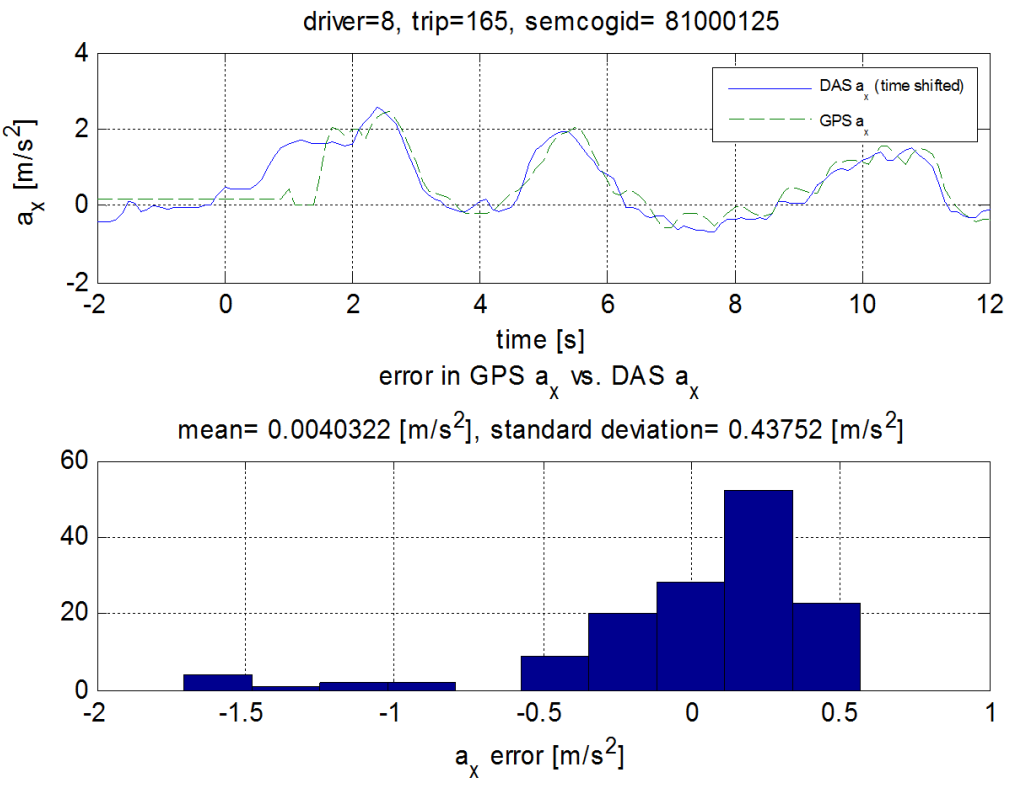

(a)

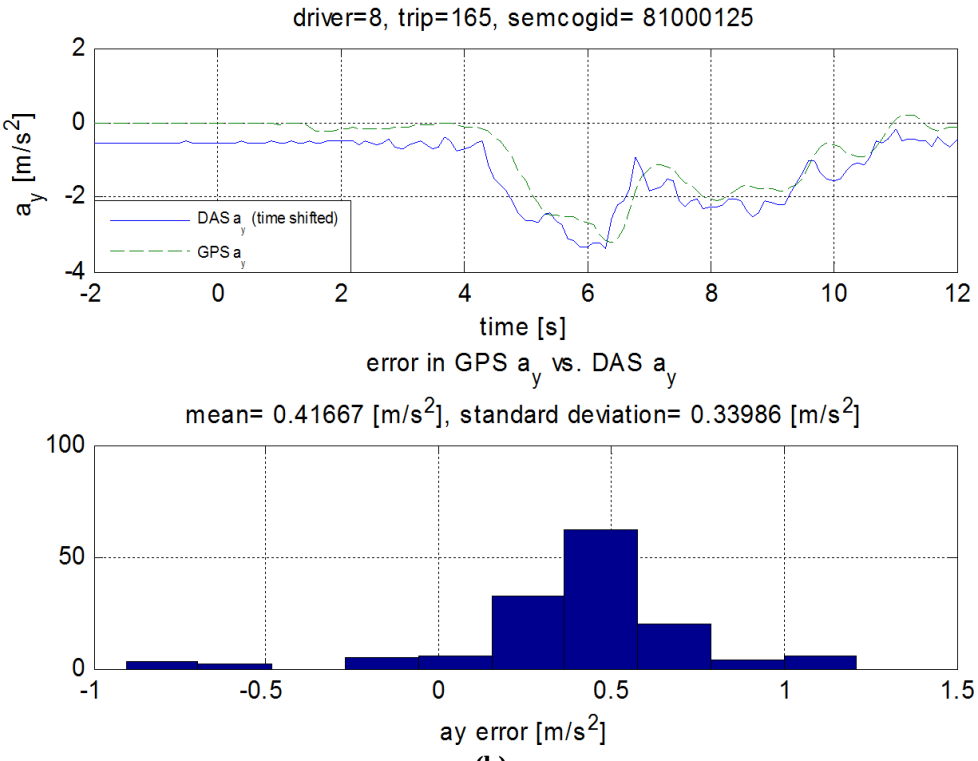

(b)

Figure 3.10 Comparisons of (a) longitudinal and (b) lateral components of the Kalman filter based acceleration vs. those of on-board measurement.

3.3 Trajectory Reconstruction for Principal Other Vehicles

3.3.1 Locating Target Points

By using the SV trajectory reconstructed in Section 3.2, the target points detected by the forward radars were located on the two dimensional plane. The radars gave information about the target motion by R, $\dot{R}$ and t_r (range, range-rate and lateral deviation – a surrogate for azimuth (Figure 3.11). The radars on the test vehicle were installed behind the fog light on each side located at 0.65m away from the mid-point of the frontal edge, with the center line of the field of view (FOV) canted 3deg outward. Therefore azimuth angle ϕ was calculated by the following equation,

$$\phi = \tan^{-1}\left(t_C / L\right) \tag{3.6}$$

where $t_C = R\sin\beta + 0.65,\ L = R\cos\beta,\ \beta = \alpha + 3\times\pi/180$ and $\alpha = \sin^{-1}\left(t_r / R\right)$.

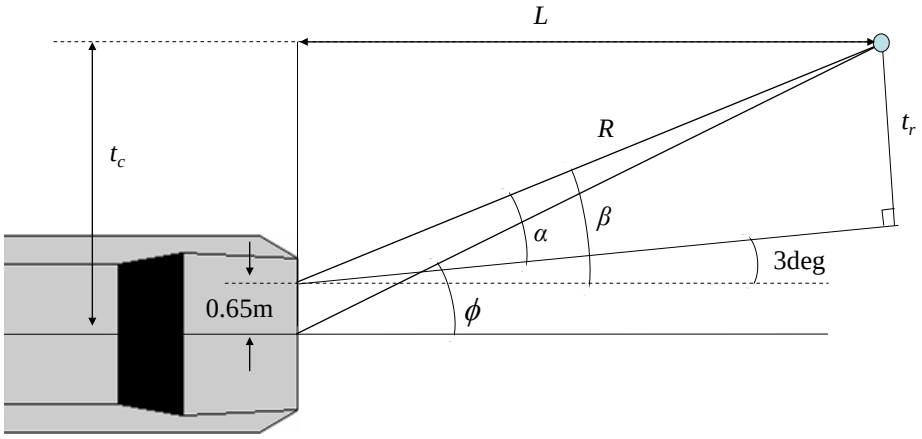

Figure 3.11 Geometry used in the azimuth calculation.

The ISO coordinate system was used for both radars while the SAE coordinate system was applied to all other parts in the analysis.

A resulting target point distribution is shown in Figure 3.12. In the figure, LF and RF indicate the radars on the left and right respectively and stationary objects (triangles)

detected by the radars were also plotted for use in the next section to remove the latency time difference between the GPS and radars. In this example, there were two vehicles confirmed by video observation: a truck in front of the SV and a POV approaching the intersection. Previously, Δt_1 was used as an estimate for the latency time difference between the SV motion based on the GPS position and DAS, but it might not be the best choice – see the distorted POV trajectory in Figure 3.12. This result brought a need for a second adjustment of the time difference between GPS and radar timing. This issue will be discussed in the next section.

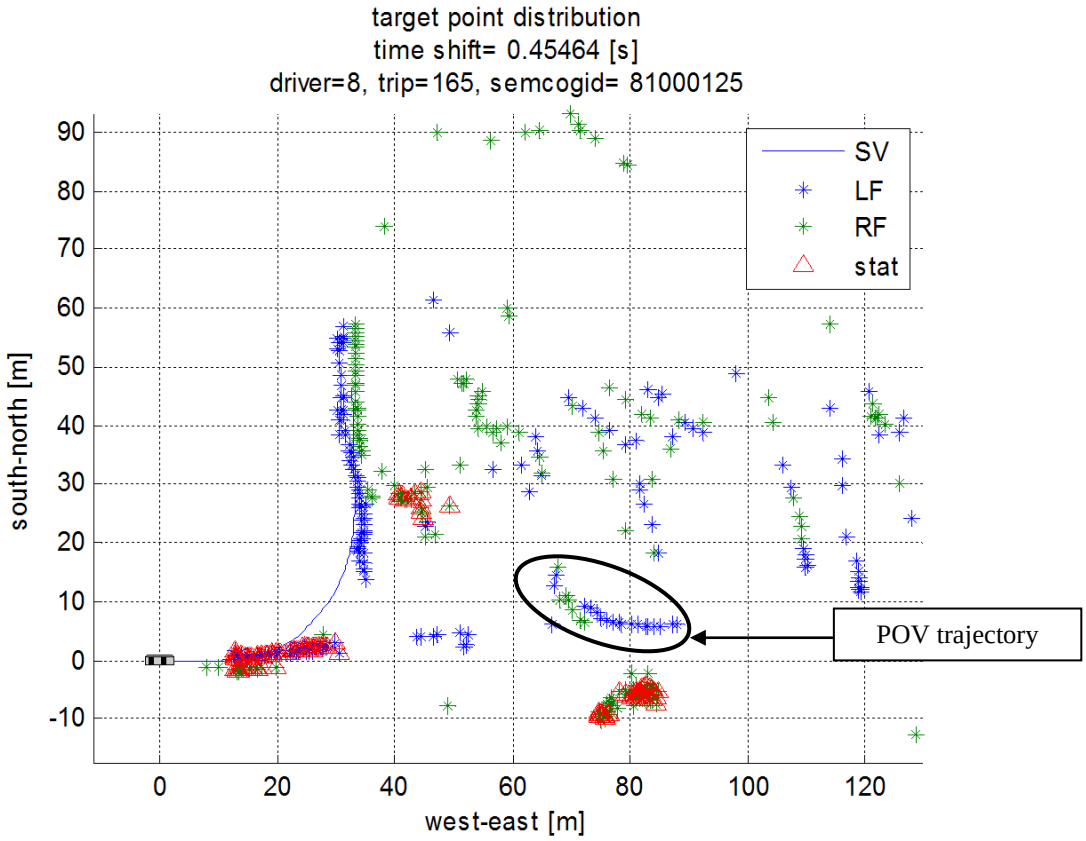

Figure 3.12 Target point distribution and detected static (slow) objects by using Δt_1 as the initial estimation of the latency time between the GPS and radars.

3.3.2 Latency Time Difference in GPS and Radars

It has been recognized that another latency time difference adjustment is needed, since this latency time difference is between the GPS and forward radar rather than the yaw

rate sensor. This issue was confirmed by both a scenario in which an SV was driven straight and going to stop at a red signal behind a car already stopped and waiting as well as the bent POV trajectory in Figure 3.12. The distribution of the stopped car was not condensed but stretched as if it had been moving with its direction being the same as that of the SV trajectory. Therefore, a second optimization problem is to be formulated in order to estimate another time shift Δt_2. This issue can be treated similarly to the calculation of Δt_1. However, the variable used here is the scattering of the target points which consists of stationary objects and the degree of the scattering of the target points is defined as the sum of the distances to the points of a stationary object from its geometric centroid. Therefore, for the *j*-th stationary object the cost function is defined as,

$$f_j = \sum_{k=1}^{n} \left\{ \left(x_{j,k}(\Delta t_2) - x_{j,c}(\Delta t_2) \right)^2 + \left(y_{j,k}(\Delta t_2) - y_{j,c}(\Delta t_2) \right)^2 \right\} \tag{3.7}$$

where $(x_{j,k}, y_{j,k})$ represented the *k*-th point in the *j*-th stationary object and $(x_{j,c}, y_{j,c})$ is the coordinates of the geometric centroid of the same object. Consequently, a multi-objective optimization problem is formulated for multiple objects, using the weighted sum method,

$$\min_{\Delta t_2} f = \sum_{j=1}^{m} w_j f_j \,, \tag{3.8}$$

where w_j is the weighting factor for the *j*-th stationary object and its value is defined as the reciprocal of the product of the average range $\bar{R}_j$ and number of points *N* in the object, i.e. $w_j = 1/(\bar{R}_j N)$.

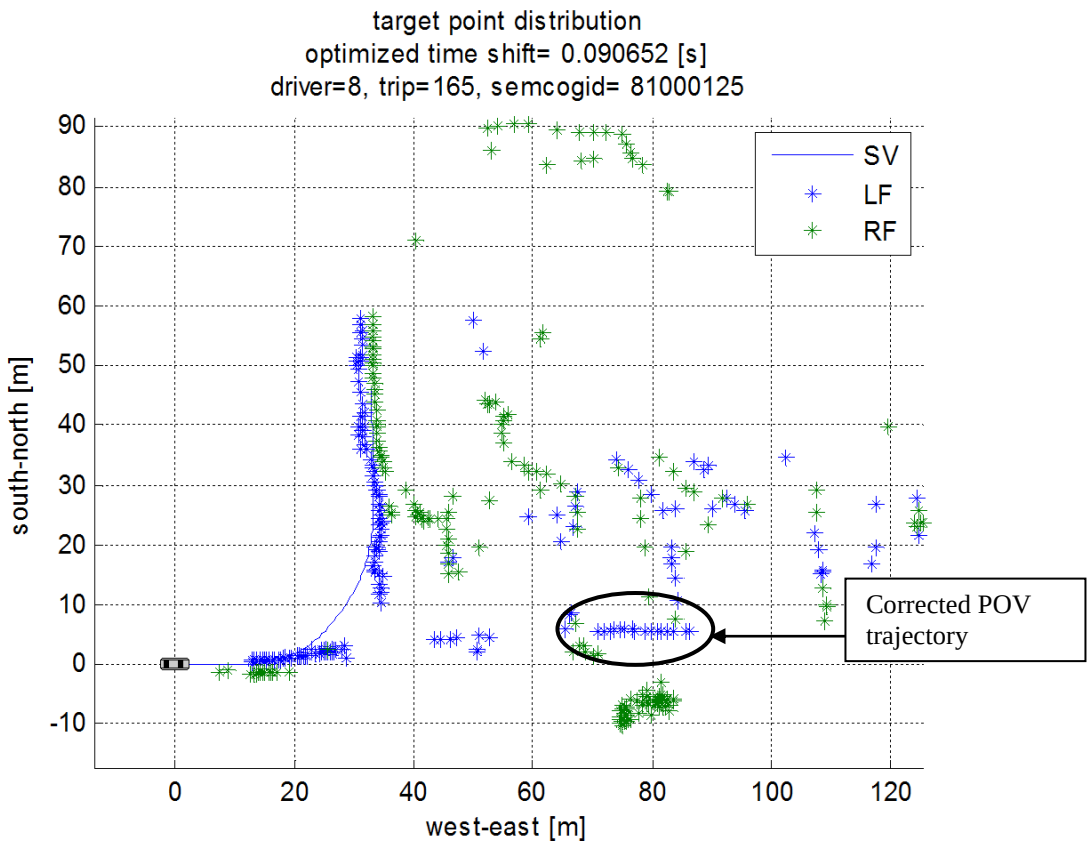

Figure 3.13 Result of the latency estimation by the multi-objective optimization to minimize the distributions of the static objects.

3.3.3 Target Point Association

The next step is to connect relevant target points to make POV trajectories. It can be achieved by the following 4-step procedure: 1) tracklet construction, 2) ambiguity resolution, 3) tracklet connection and 4) connection by kinematic variables. In the followings, the details of each step will be explained.

1) *Tracklet construction*

Tracklets were constructed on a one-time step basis using the following criteria – neighboring points are connected:

$$
\begin{aligned}
&\left|\Delta t_{r,i}\right| \le \varepsilon_1 \\
&\left|\Delta R_i\right| \le \varepsilon_2 \\
&\left|\Delta \dot{R}_i\right| \le \varepsilon_3 \\
&\left|\Delta R_i - \dot{R}_i' \Delta t_i\right| \le \varepsilon_4
\end{aligned}
\tag{3.9}
$$

where ε's are threshold values and

$$
\begin{aligned}
&\Delta t_{r,i} = t_r(t_{i+1}) - t_r(t_i) \\
&\Delta R_i = R(t_{i+1}) - R(t_i) \\
&\Delta \dot{R}_i = \dot{R}(t_{i+1}) - \dot{R}(t_i) \\
&\dot{R}_i' = \left(\dot{R}(t_{i+1}) + \dot{R}(t_i)\right)/2 \\
&\Delta t_i = t_{i+1} - t_i
\end{aligned}
\tag{3.10}
$$

The target point IDs of the predecessor and successor to be connected with a point in the current time step are then stored in a *connectivity matrix*. Then, to fully reconstruct the trajectories, the breadth first tree search method is applied. At this stage, all candidate paths are retained. The conceptual scheme is represented in the tree diagram in Figure 3.14.

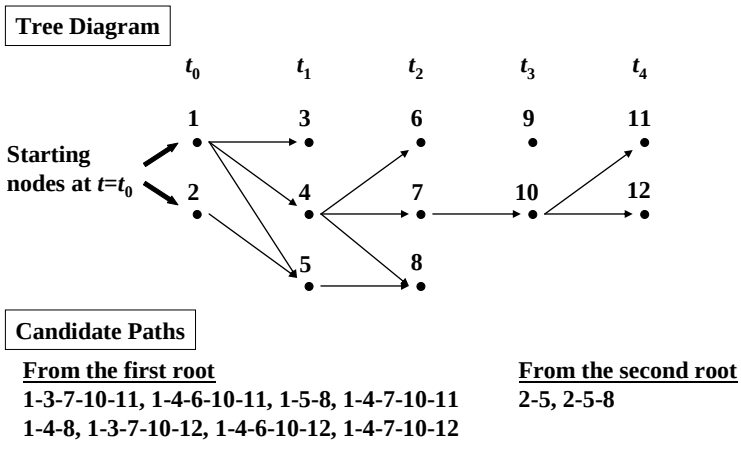

Figure 3.14 Tree diagram reflecting connectivity matrix information and resulted candidate paths to be screened by the ambiguity resolution to find the most likely one.

2) *Ambiguity resolution*

Possible split or merged segments produced by the tree search due to relatively loose threshold values for the connectivity criteria in the last step are eliminated by using the normalized distance squared (NDS) to the ambiguous node [58]. The ambiguous node is located at the point immediately after a split point or coincides with a merging point. The NDS was defined as,

$$d_{i,j} = d\mathbf{y}_{i,j}{}^{T}\mathbf{S}_i^{-1}d\mathbf{y}_{i,j} \tag{3.11}$$

where $d\mathbf{y}_{i,j} = \mathbf{y}_i(j) - \mathbf{y}_i(j-1)$.

The last equation for $d\mathbf{y}_{i,j}$ was the measurement residual and $\mathbf{S}_i$ was the innovation covariance at the j-th point (ambiguous node) of the i-th segment. The ambiguous node is assigned to the segment which cause the smallest $d_{i,j}$.

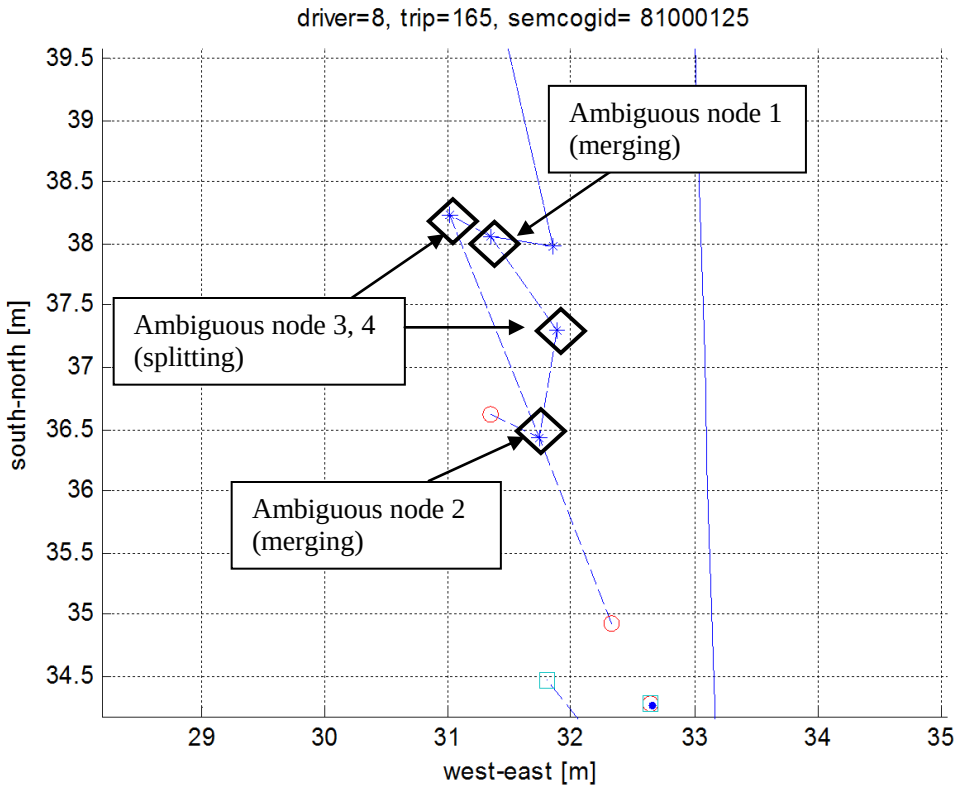

Figure 3.15 Detected ambiguous nodes.

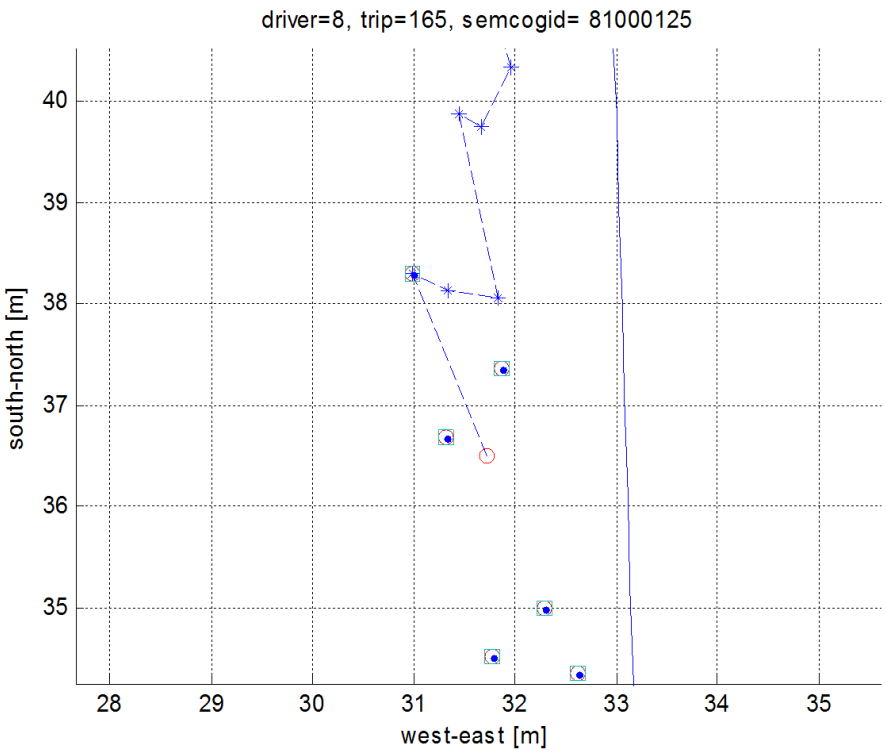

Figure 3.16 Ambiguity resolution.

3) *Tracklet connection*

Since an object might not be scanned at every time step, fragmented segments may occur. To resolve this, the same criteria used in (1) are adopted to connect split segments, but with an extended time range. When multiple choices are possible in the expanded admissible region, the ambiguity resolution described in (2) is employed.

4) *Connection by kinematic variables*

Speed between every two contiguous points in a segment was calculated geometrically using the target-point positions and, if there were any segments in which the speed was faster than a threshold value, the segment was separated at the points. This was continued until no separation was found. The issue which motivated the use of this filtering was that it was possible for target points from different objects while the SV is turning to be connected wrongly due to the lack of the angular speed of the azimuth. In other words, if there are points in distant locations for which R, $\dot{R}$ and ϕ of a point are close to those of

the other, they may be wrongly connected based on the methodology in the previous stage. There was one separation in the example case as shown in Figure 3.17.

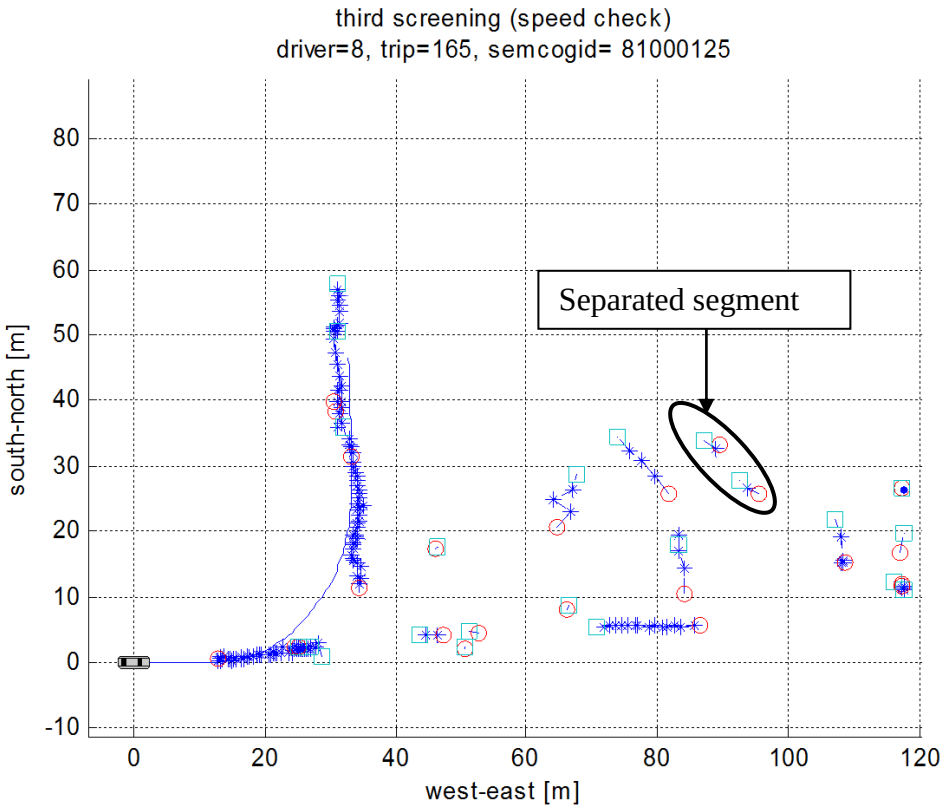

Figure 3.17 Segment separation by the speed filter.

Similarly, the acceleration was utilized to search possible additional connections between the segments. It was also found geometrically in the same manner as in the speed filter. In addition, since a length of one time-step (0.1 s) was considered for searching the target-point connectivity, it was expanded to a longer time period (e.g. 0.5 s).

For a pair of segments to be evaluated for their association, two acceleration values were calculated by choosing the last point from the first segment and the first two points from the second for the first acceleration; then the last two points from the first segment and the first point from the second segment were selected for the calculation of the second acceleration. Then, the difference of these values was compared with a threshold value. In the example case, there was no segment associations found, so the following result was taken from another left turn event (Figure 3.18).

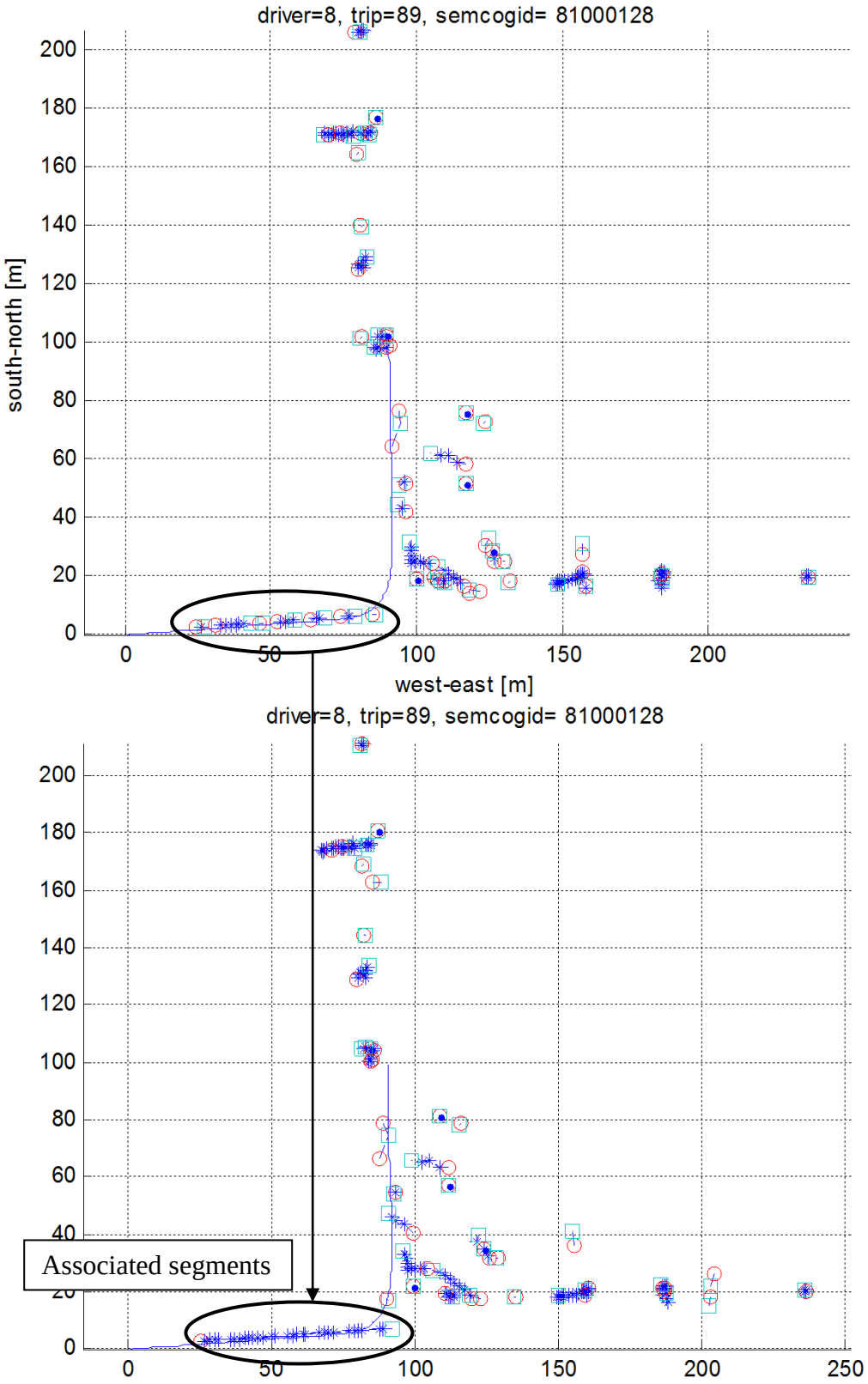

Figure 3.18 Segment association by the acceleration filter.

Finally, reconstructed POV trajectories made with the above methods are shown in Figure 3.19. This figure contains the result using the left radar only, since the right radar is not significant for detecting POVs which is on the left side of the SV before turning. However, the right radar is still useful for detecting stationary objects on the road side for the latency difference correction.

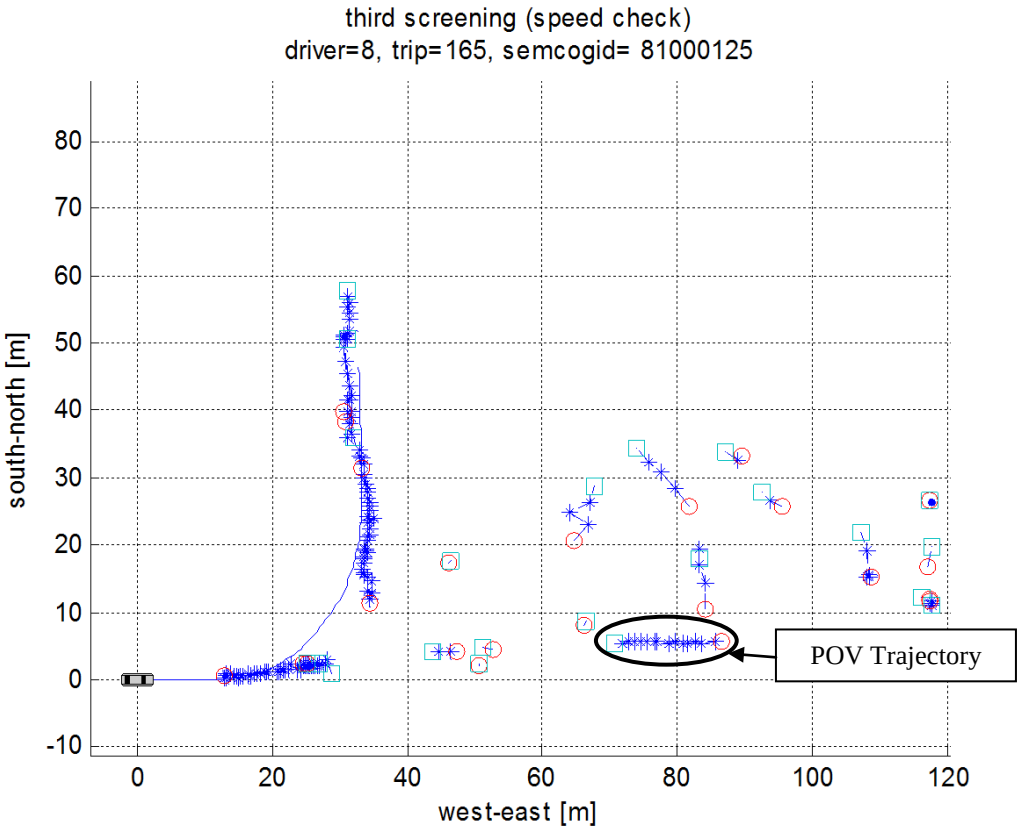

Figure 3.19 Reconstructed trajectory of the principal other vehicle.

3.3.4 X-Y Kalman Filter

The X-Y Kalman filter can be used for the POVs as well as for an SV to estimate their position, velocity and acceleration in global coordinates. Sufficiently accurate position and speed of the POVs are crucial for conflict metrics analysis. As convenient measures, distance and relative speed between the SV and POV derived from their global variables (Kalman filter estimates) can be used to compare with R and $\dot{R}$. Results have shown that, despite a fairly accurate distance, the relative speed tends to contain large errors. This is due to insufficient data points available in the POV tracks, and the backward

Kalman filter does not converge to appropriate initial estimates and state covariance for the forward Kalman filter. In order to resolve this issue, the velocity estimate is replaced with another velocity computed by the following equations using Kalman filter position estimate and $\dot{R}$.

$$\begin{aligned}
&\mathbf{r}_{POV/SV} = \mathbf{r}_{POV} - \mathbf{r}_{SV} = R\cos(\theta_{SV}+\phi)\mathbf{I} + R\sin(\theta_{SV}+\phi)\mathbf{J} \\
&\mathbf{v}_{POV/SV} = \mathbf{v}_{POV} - \mathbf{v}_{SV} = \left(U_{POV}\cos\theta_{POV} - \hat{U}\cos\theta_{SV}\right)\mathbf{I} + \left(U_{POV}\sin\theta_{POV} - \hat{U}\sin\theta_{SV}\right)\mathbf{J} \\
&\dot{R} = \mathbf{v}_{POV/SV}\cdot\frac{\mathbf{r}_{POV/SV}}{|\mathbf{r}_{POV/SV}|} \\
&U_{POV} = \frac{\dot{R}+\hat{U}\cos\phi}{\cos(\theta_{POV}-(\theta_{SV}+\phi))} \\
&\therefore \mathbf{v}_{POV} = U_{POV}\cos(\theta_{POV}-(\theta_{SV}+\phi))\mathbf{I} + U_{POV}\sin(\theta_{POV}-(\theta_{SV}+\phi))\mathbf{J}
\end{aligned} \tag{3.12}$$

Since the current interest is only POVs on the other traffic before the SV turns, the POV heading angle is assumed to be $\theta_{POV} \approx \theta_{SV} + \pi$.

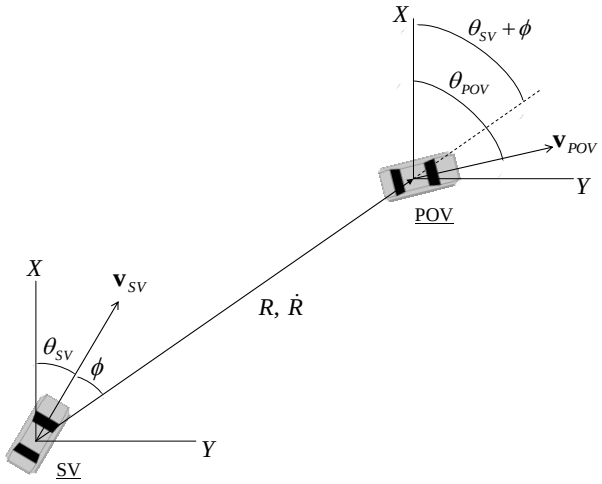

Figure 3.20 Orientations of the subject and principal other vehicles.

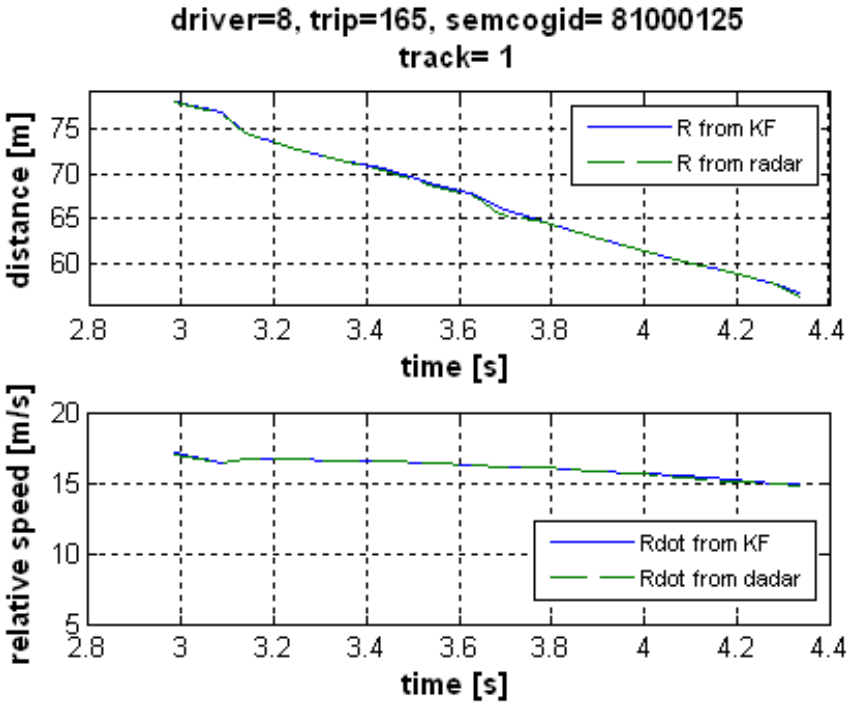

Figure 3.21 Modified results of the X-Y Kalman filter for the through vehicle with the alternative velocity.

3.3.5 Extrapolation of Principal Other Vehicle Trajectory

With the field of view of the forward radars (8 degree), the POV cannot be detected all the time while the SV is turning, but its future trajectory must be predicted for the conflict metrics. Extrapolation of the trajectory was achieved by assuming that the POV kept the velocity of the last point of the trajectory after it disappeared from the radar, with some adjustment made to keep the POV in its current lane. Such assumptions appear inevitable since the POV motion is not available once the SV has turned.

As mentioned, a primary issue in the extrapolation process using the POV velocity is direction rather than speed- the final part of such POV trajectory may direct it off the road and cause a significant error in an extrapolated trajectory. Hence, for extrapolation, the magnitude of the velocity vector was used, and, for the direction, the POV was assumed to travel on an imaginary straight path which was created by connecting two points: the last point of the POV trajectory and a point defined at 3.6 m (typical lane

width) away from the left turn lane where the SV was located to the left of the SV in its lateral direction. This is illustrated in Figure 3.22.

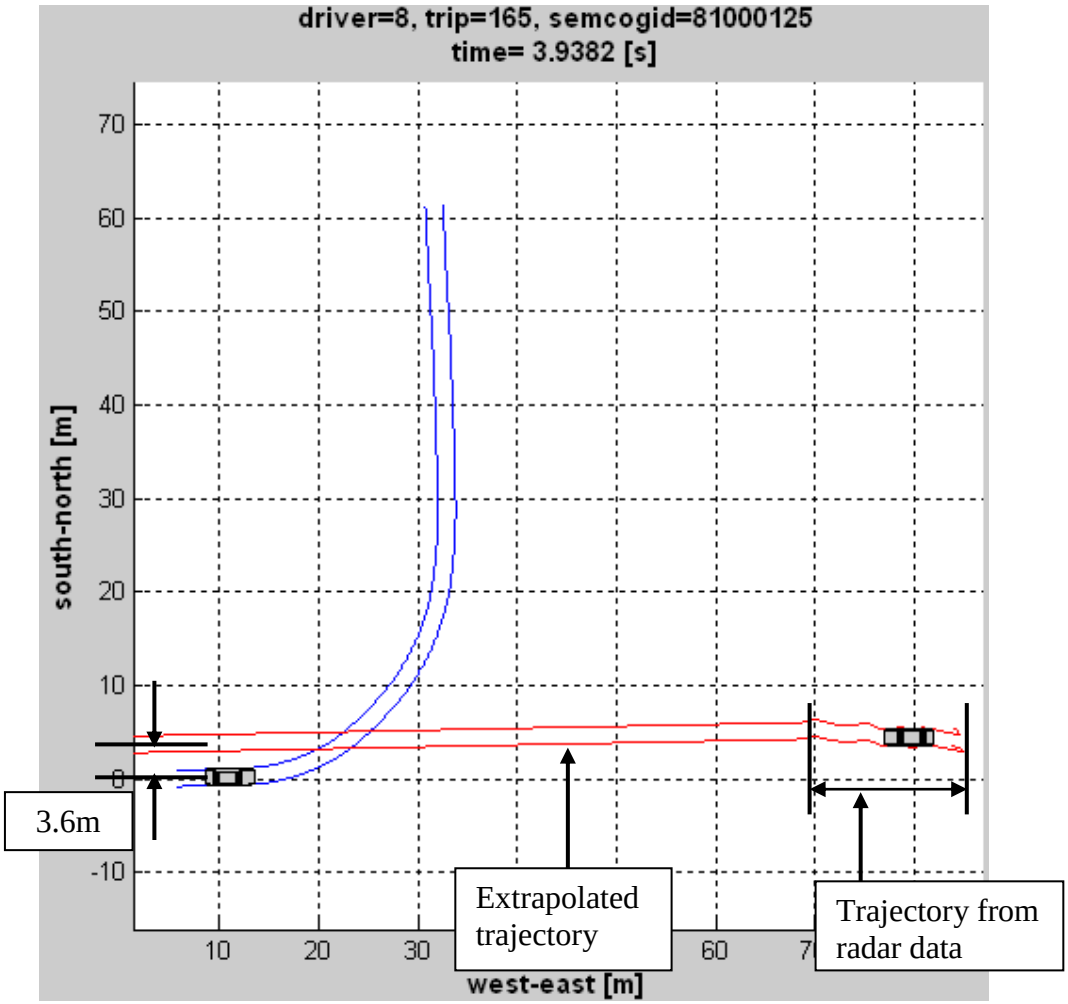

Figure 3.22 Extrapolated trajectory of the principal other vehicle.

3.4 Example Result

Figure 3.23 shows examples of completed trajectories in each of which an SV and two POVs drawn on an aerial map of an intersection. It can be noticed that vehicle trajectories did not fit in the traffic lane perfectly due to errors in the GPS and map data. Nevertheless, it seems fairly acceptable for conflict metric analysis. Besides, in terms of the relative positions between the SV and POV, the result shows an acceptable linear extrapolation to compensate for the error in the lateral position of the POV.

SEMCOGID#81000125
Rawsonville Rd@ Willis Rd
Washtenaw County, Michigan

Driver=8, Trip=165
Start time=41000,
End time=42000

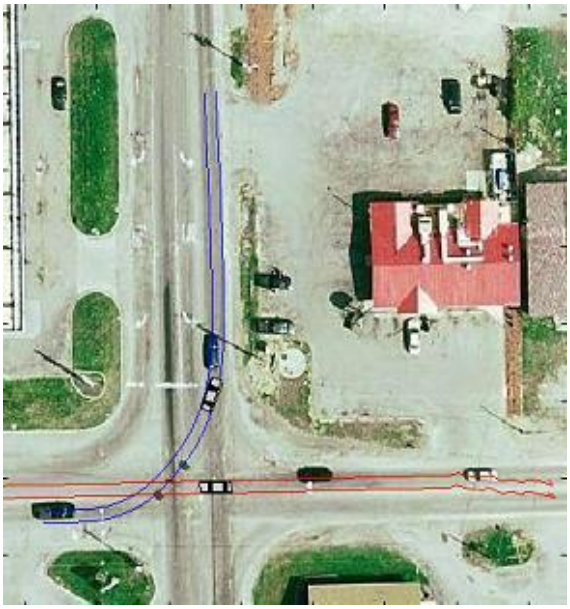

SEMCOGID#81000083
Huron River Dr@Superior Rd
Washtenaw County, Michigan

Driver=39, Trip=25
Start time=37000,
End time=38000

SEMCOGID#81000148
M153@Prospect Rd
Washtenaw County, Michigan

Driver=39, Trip=42
Start time=79000,
End time=80000

Figure 3.23 Examples of reconstructed trajectories.

Chapter 4
Conflict Analysis

4.1 Leading Buffer and Trailing Buffer

The LB and TB are calculated at distinct conflict points as mentioned earlier, but the computation schemes are exactly identical (see Section 4.2.2). Moreover, the LB/TB is analogous to the GT [7, 8] representing the "spare time" between the two vehicles. A significant advantage of the LB/TB over the GT is its way of predicting the SV speed. Although the original definition of the GT states that it can be used for both cases when the SV crosses first and second [7], its use of constant speed assumption can cause an infinitely large estimated time if the SV speed is very low. An alternative way to estimate the SV motion is based on a nominal acceleration and speed [4]. In this study, the reference speed profile (U_{ref}) is an experimentally derived speed profile by averaging available "free turns" (meaning that the SV turns without being forced to stop by a POV, signal and/or pedestrian). It is to be found for each direction of a left turn for an intersection. It is intended to predict the time reasonably from any SV speed (see Section 4.2.1). The varying conflict point location depending on the vehicles' configuration (Figure 1.2) is also a benefit adopted in the LB/TB. Caution must be taken; both the LB and TB must be calculated for all approaching POVs until finding a pair of POVs between which the SV will make a left turn with an acceptable gap in order to find which conflict point represents the more critical measurement for each POV. Example applications of the LB/TB are discussed in Section 4.5.

4.2 Calculation of the Leading Buffer and Trailing Buffer

4.2.1 Reference Speed Profile and Predicted Speed Profile

For the SV, the reference speed profile, U_{ref}, represents a free turn motion. It is created by averaging actual free turns with no conflicts where, even if they exist, the first POV will still take a long time to reach an intersection. By considering potential effects from intersection geometry, U_{ref} is made for each intersection and each direction within the intersection. The resulting U_{ref} is a function of position only along a left turn path with an origin located at the stop bar on the original road where the SV is located before making a left turn (Equation (4.1) to (4.5)).

$$U_{ref}(s) = f_1(s)\Phi(s_{c1} - s) + f_2(s)\{\Phi(s - s_{c1}) - \Phi(s - s_{c2})\} + f_3(s)\Phi(s - s_{c2}) \tag{4.1}$$

$$f_1(s) = \mathrm{Re}\left(\sqrt{2p_1(s - p_2)}\right), \ (p_1 < 0) \tag{4.2}$$

$$f_2(s) = U_{th} \tag{4.3}$$

$$f_3(s) = \mathrm{Re}\left(\sqrt{2q_1(s - q_2)}\right), \ (q_1 > 0) \tag{4.4}$$

$$\Phi(x) = \begin{cases} 0, & x < 0 \\ 1, & x \geq 0 \end{cases} \tag{4.5}$$

where s is the path coordinate of the SV, p_1, p_2, q_1 and q_2 are shape parameters, U_{th} is threshold speed, s_{c1} is the abscissa of the intersection between f_1 and f_2 and s_{c2} is that between f_2 and f_3.

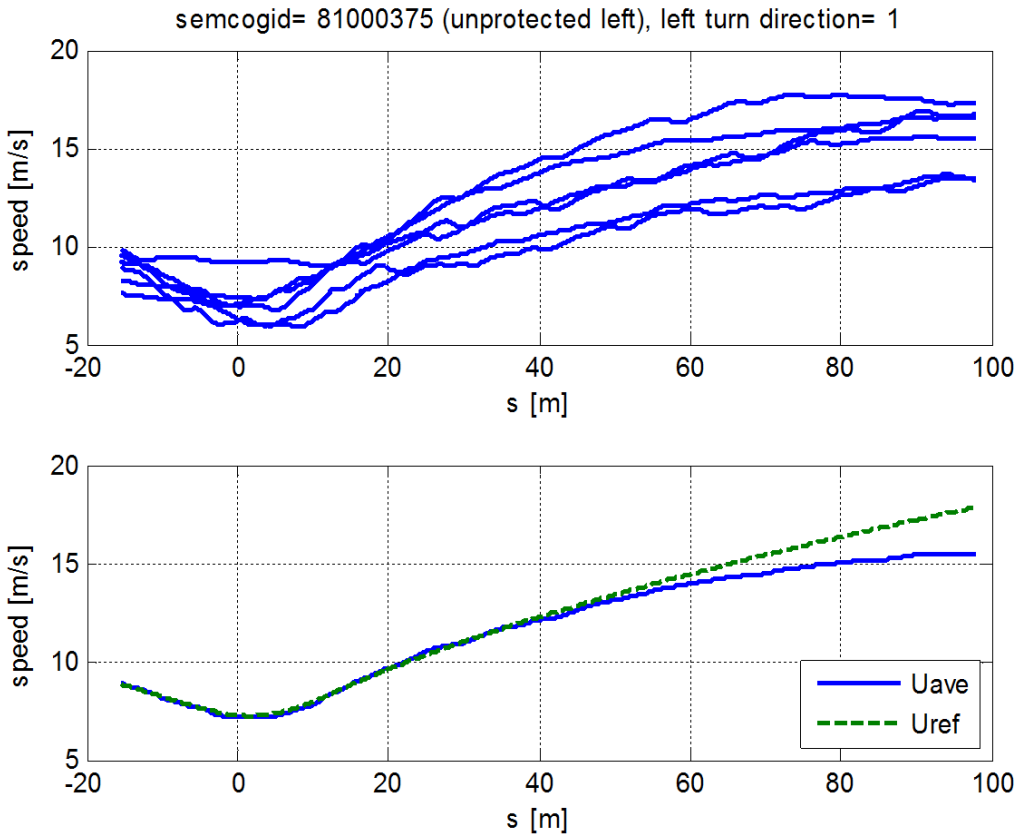

Figure 4.1 Preparation of the reference speed profile. Free turns at a single intersection from data (top), and averaged speed profile and its curve fit result (bottom).

As a result, the predicted speed profile, U_{pred}, can be constructed by using U_{ref} in the following equation.

$$U_{pred}(s;s_0) = \left(k_1 - U_{ref}(s_0)\right)e^{-k_2(s-s_0)} + U_{ref} \tag{4.6}$$

where s_0 is a SV position at which the LB/TB will be computed and k_1 and k_2 are parameters. The first parameter is set to the speed at $s=s_0$ (i.e. $k_1= U(s_0)$) so that the coefficient of the exponential part specifies the speed difference at that point ($s=s_0$) and the second parameter is a constant (e.g. $k_2=0.3$). This function converges to the U_{ref} exponentially to compensate for speed deviation and to provide a predicted speed profile. It is to be updated at each location on the SV path. Figure 4.2 shows that an example U_{pred} curve was found using the initial SV location along a time axis.

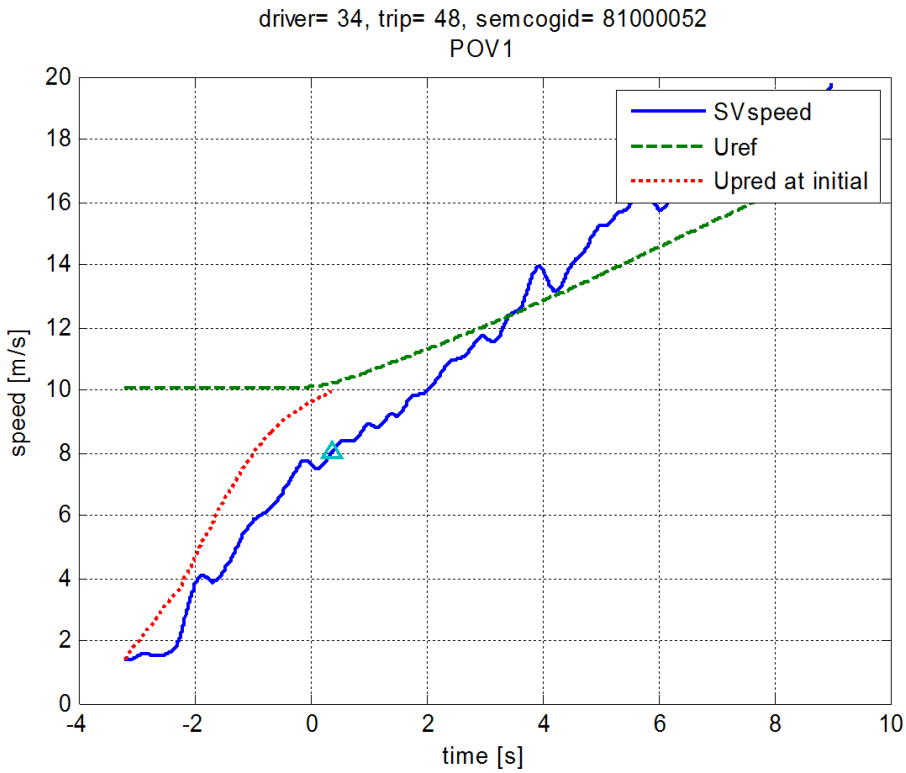

Figure 4.2 Example of the predicted speed profile.

For POVs, it is considered rather trivial since they are unlikely to change their speeds greatly. Therefore, the speeds of POVs have been assumed to be constant.

4.2.2 Application of Predicted Speed Profile

The U_{pred} explained above is used to predict $T_{C(SV)}$ (time when the SV is arriving at the conflict point for an LB case or leaving that point for a TB case) and can be computed by integrating the inverse of U_{pred} along s;

$$T_{C(SV)}(t) = \int_{s_0|_{t=t}}^{s_C|_{t=t_C}} \frac{ds}{U_{pred}(s; s_0)} \tag{4.7}$$

where s_0 is the longitudinal track coordinate at t (time of LB/TB computation) and s_C and t_C are those for the SV at the conflict point. $T_{C(POV)}$ can be calculated in a similar way, but

the result becomes a straight line because of the POV trajectory extrapolated using a constant speed as mentioned in Section 4.2.1. Therefore,

$$T_{C(POV)}(t) = \frac{D(t)}{U_{POV}} \tag{4.8}$$

where $D(t)$ is the length of the path between the POV and conflict point at the time of LB/TB computation and U_{POV} is the POV speed, that is constant. The LB/TB can be calculated now by the equation

$$\mathrm{LB/TB} = T_{C(POV)}(t) - T_{C(SV)}(t). \tag{4.9}$$

where the value is defined to become negative if a left turn scenario is an LB case.

It is worth clarifying the relationship between the order of the SV's crossing encroachment zone and the LB/TB. Although the terms "TB (or LB) case" and "SV crossing first (or second)" can be used interchangeably, the LB and TB can be computed for either vehicle configuration in Figure 1.2. It is a matter of fact that the TB is the more significant measurement than the LB in the case of the SV crossing first and the LB is the more suitable conflict metric than the TB in the other case. In this case, the sign of a non-significant measurement would be opposite if it were a significant one. In practice, both measurements are to be computed, since which measurement is more important than the other is not known in advance.

4.3 Post Encroachment Time for Accuracy Check

The Post Encroachment Time (PET) is now computed using the vehicle trajectories reconstructed from the driving data, and distributions from the results are to be shown for all detected left turns with POVs. Further analysis will be undertaken to see which factors influence the PET distributions. Attention is limited to factors that are directly available in the objective data: POV speed and driver types. Other factors may be of interest, including the size of the oncoming vehicle, visibility and road condition; but these factors are not directly available in the driving database and will not be analyzed here.

4.3.1 Overall Post Encroachment Time Distributions

Among the unprotected left turn events mined from the naturalistic driving database (RDCW-FOT) (Table 2.4), 530 through POVs were involved which confirmed those left turn events as unprotected LTAP/OD scenarios at signalized intersections. A distribution of the PET is shown in Figure 4.3 for each of the cases of the SV crossing first and second. Since the detections of POVs were made relatively to the SVs in the trajectory reconstruction, which were often not completely stationary even when they turned second after a POV, the resulted POV motion can contain larger error than another setup where fixed radars are used at selected intersections. Nevertheless, at the 20th percentile of the distributions in Figure 4.3, the PETs for the crossing first and second cases are $2\,\mathrm{s}$ and $-1\mathrm{s}$ respectively which are the same as those reported in another research using site-based radars at selected intersections [9] and would be considered as critical spare times for typical left turns in the LTAP/OD scenarios.

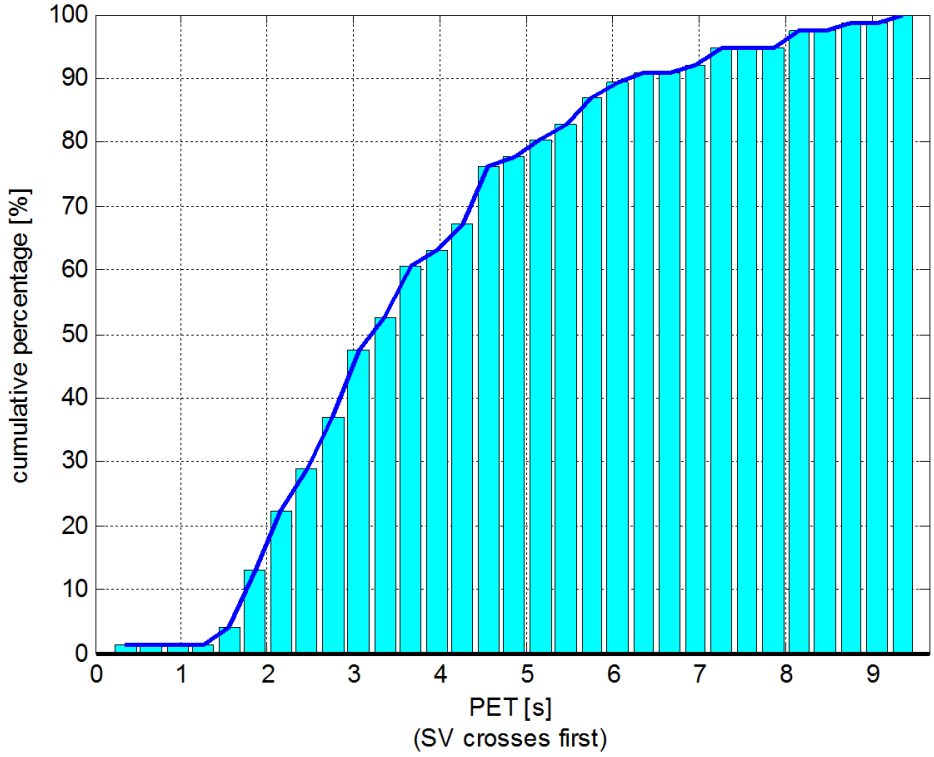

(a)

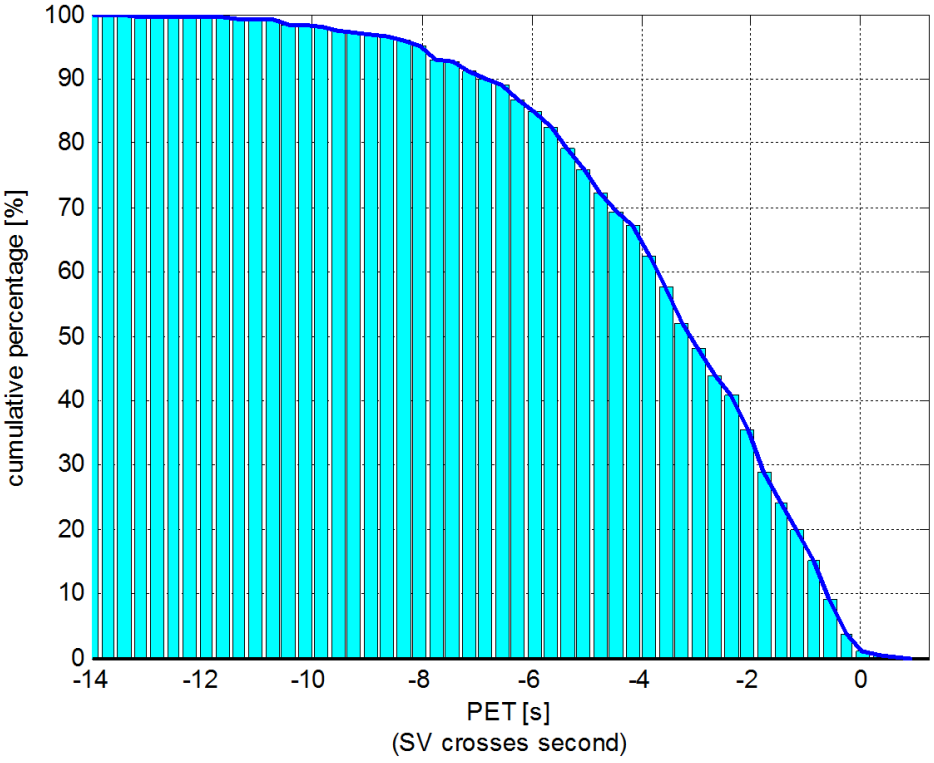

(b)

Figure 4.3 Cumulative percentage of the post encroachment time: (a) subject vehicle crosses first and (b) second.

4.3.2 Effect of Principal Other Vehicle Speed

It is expected that driver acceptance of an available gap varies depending on the POV speed due to a potential increase of the threat level the driver feels as the POV speed increases. Figure 4.4 shows distributions for different speed ranges. Since a speed limit of each road is unavailable, actual POV speed was used to classify the left turn events into two sets with slow and fast POVs respectively. A threshold speed to distinguish slow and fast POVs was set to 30 mph or 13.33 m/s. Clearly, the ratio of the number of positive PETs to the number of negative PETs in left turn events with fast POVs is less than that in the events with slow POVs. For the distribution made for slow POVs, 41.9 % is attributed to the SV turning first. On the other hand, 17.5 % accounted for the SV turning second for the fast POVs.

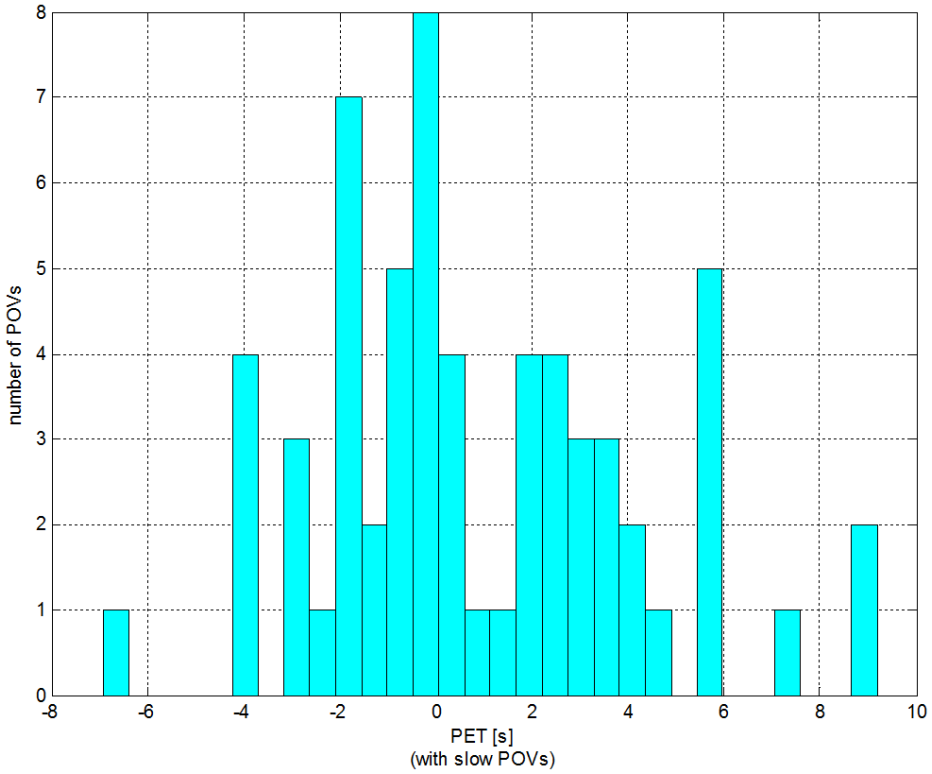

(a)

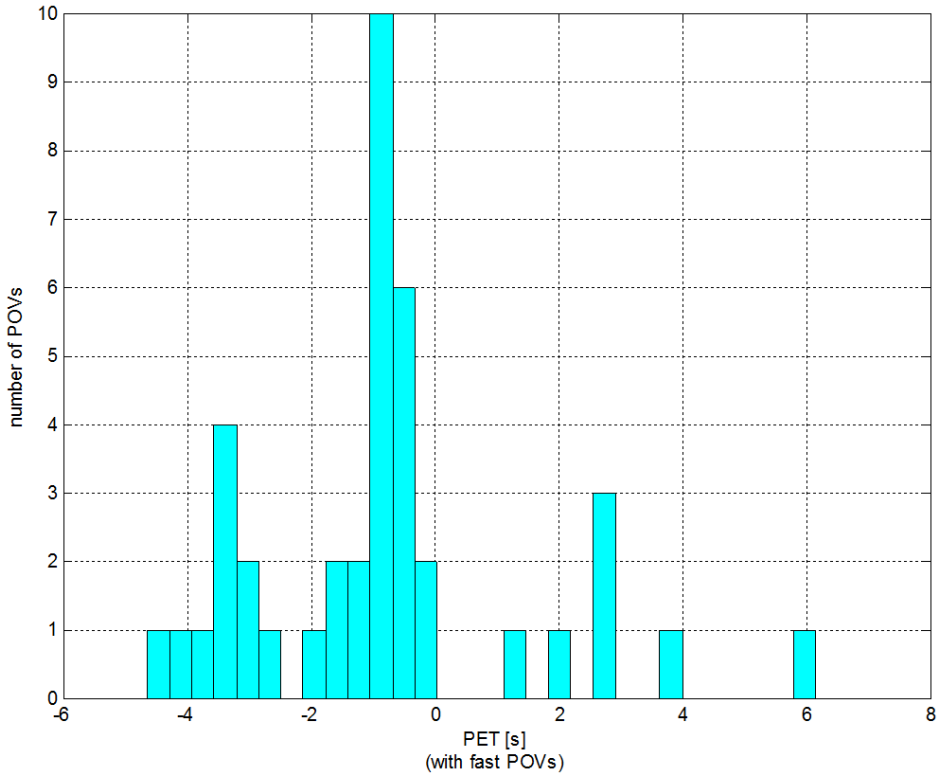

(b)

Figure 4.4 Histograms of the post encroachment time for different speed ranges of principal other vehicles: (a) slow and (b) fast.

4.3.3 Age and Gender Effects

Figure 4.5 shows separate PET calculation results for younger, middle and older age groups, and Figure 4.6 for male and female groups. In both cases, no clear difference can be observed. Of course, error in the results can be a reason for this, but there could be other factors related to the drivers' ability to estimate the gap accurately and vehicle control skill. For example, previous studies showed that human drivers consistently underestimated the TTC [59-66], and the degree of underestimation is the largest in the older driver group [67, 68]. However, this fact did not result in larger PET values which correspond to safer decisions. Instead, the threshold of the accepted PET for the older drivers is not different from the other age groups'. In fact, the crash rate among older drivers is not significantly less than among the other age groups [1]. In [65], it is said that the lack of the potential beneficial outcome of reducing the number of accidents in which older drivers are involved occurred because the underestimation of the approaching

vehicle is irrelevant to the judgment of whether a potential collision would occur or not. Alternatively, driving ability is considered to affect gap acceptance behavior [66] in which it was observed that the older drivers selected a larger gap between two POVs in left turn into path (LTIP) events due to slower speed than the other age groups. Although our study focuses on the LTAP/OD scenarios only, a similar gap acceptance tendency may exist since it is required to estimate the time taken to clear the encroachment zone for the self vehicle. Table 4.1 shows the mean and standard deviations of the maximum lateral acceleration in left turns calculated for each age/gender group as a brief measure of the speed selections of the drivers during driving in intersections. The mean values consistently decreases across the age groups. It indicates that older drivers select slower speeds in an intersection compared to younger drivers. It could be implied that an underestimated time to arrival of a POV by an older driver is cancelled out by the time of exiting the encroachment zone to have the same PET as younger drivers.

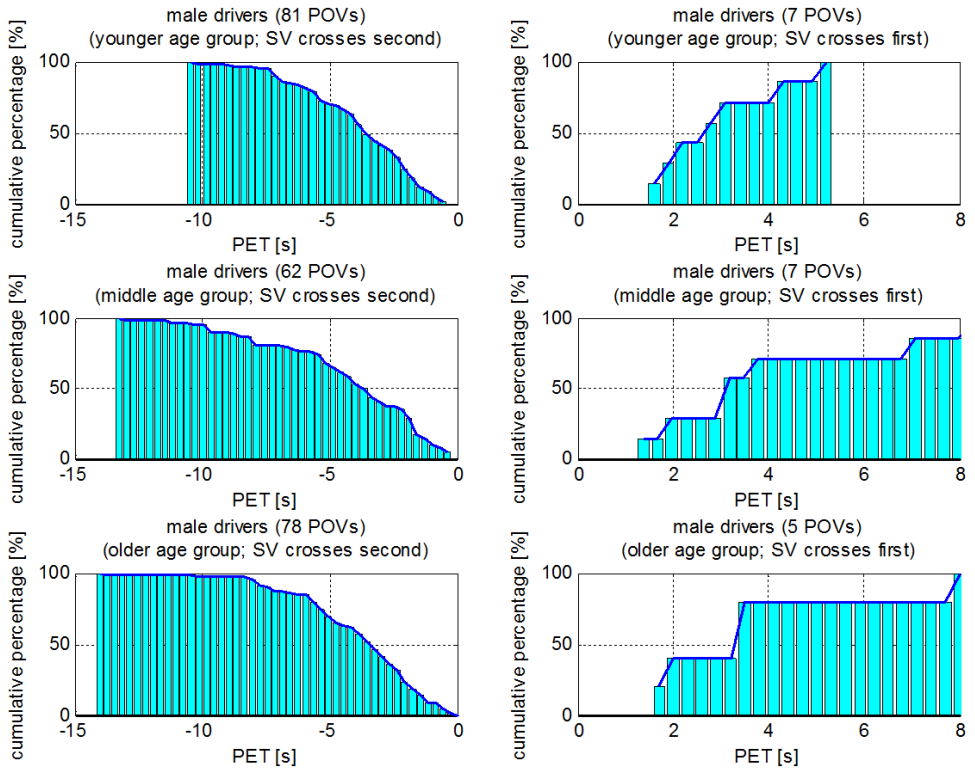

(a)

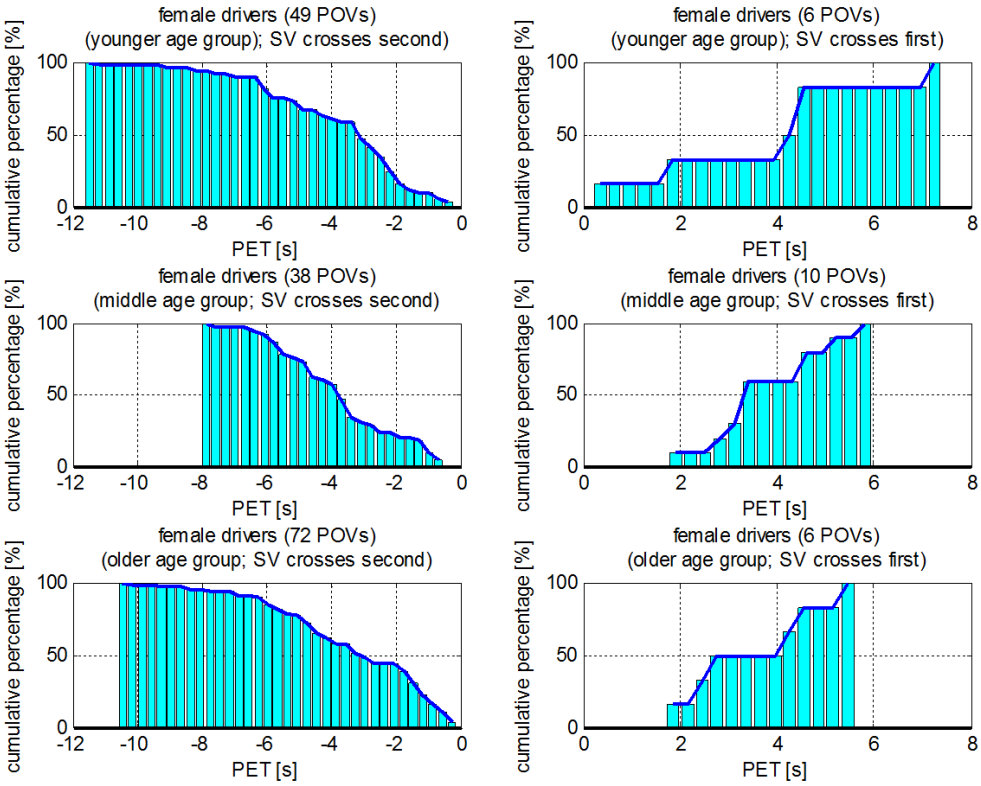

(b)

Figure 4.5 Distributions of the post encroachment time by age: (a) male and (b) female.

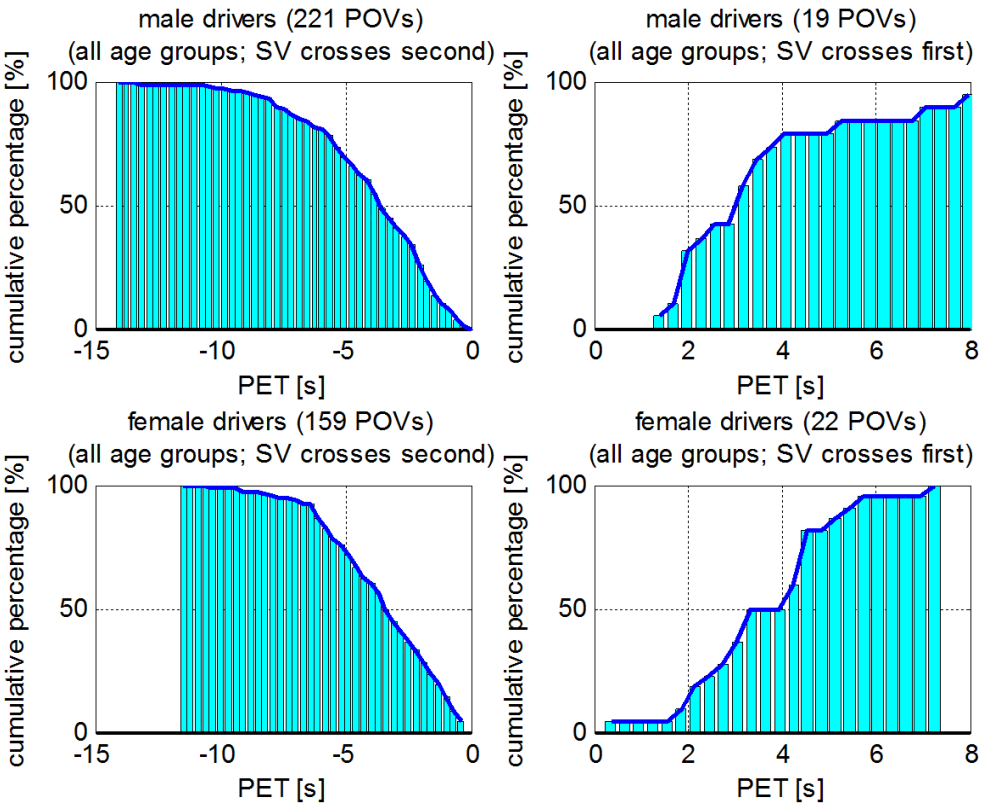

Figure 4.6 Distributions of the post encroachment time by gender.

Table 4.1 Average maximum lateral acceleration in left turns by age and gender.

		Younger	Middle	Older
Male	μ [m/s^2]	3.80	3.64	3.36
	σ [m/s^2]	0.84	0.67	0.54
Female	μ [m/s^2]	3.68	3.08	3.18
	σ [m/s^2]	0.72	0.67	0.54

4.4 Buffer Bands for Multiple Principal Other Vehicle Cases

If there is only one relevant POV, the significant conflict metrics will be the TB. This is because it is a relatively simple task for the SV to cross the encroachment zone after the POV without causing a collision. In this case, the LB might be used only to determine when a warning by the assistance system should be turned off. On the other hand, if there are multiple POVs, the LB needs to be evaluated as well as the TB because it is crucial to establishing suitable gaps for a safe left turn between POVs of a particular pair. In this

section, the buffer band is introduced. With these concepts, available gaps between POVs can easily be visualized for the purpose of finding an acceptable gap. There are a few important facts about the LB/TB; 1) the LB must be negative if the SV crosses second, 2) the TB must be positive if it crosses first, and 3) TB is always smaller than the LB when computed for any single POV (this can be proven easily by computing the difference, LB minus TB, using times to reach or leave the conflict point of the vehicles for any configuration of the SV and POV as long as the assumptions in Section 1.2 are maintained). As a result, the following relations hold; $0 < \mathrm{TB} < \mathrm{LB}$ for the case of the SV crossing first and $\mathrm{TB} < \mathrm{LB} < 0$ for the other case. Consequently, the buffer band is created by the LB curve (upper bound) and TB curve (lower bound) for each POV, and the SV is unable to start a left turn when the condition, $\mathrm{TB} < 0 < \mathrm{LB}$, is true. In other words, a left turn is achievable only when both have the same signs.

For a multiple POV case, if there is an enough gap between two POVs with which a safe left turn can be expected, the conditions for this situation are,

$$\begin{cases} \mathrm{LB}_i \le \Delta_{\mathrm{LB}} \\ \mathrm{TB}_{i+1} \ge \Delta_{\mathrm{TB}} \end{cases}, \ (1 \le i \le n-1). \tag{4.10}$$

where n(>2) is the number of approaching POVs, LB_i is the LB of the i-th POV, TB_{i+1} is the TB of the (i+1)-th POV which follows i-th POV, Δ_{LB}(<0) is that for maximum acceptable LB and Δ_{TB}(>0) is a threshold for minimum acceptable TB. As a result, a relationship, $\mathrm{TB}_i < \mathrm{LB}_i < 0 < \mathrm{TB}_{i+1} < \mathrm{LB}_{i+1}$, holds for an acceptable gap. The band gap between the buffer bands of the two POVs lies across the horizontal line at the ordinate of 0 s on the predicted-time vs. time plot.

Δ_{LB} and Δ_{TB} are crucial parameters in the intersection assistance system since safety judgment is directly affected by these values as shown in expression (4.10). However, a result of the LB/TB calculation always contains an error, so it is required to adjust Δ_{LB} and Δ_{TB} properly so as to minimize the effect of the error between PET and LB/TB on the assistance system performance. This issue is the main objective in Chapter 6; virtual free

left turn events with POVs created by the Monte Carlo simulations are used for which it is evaluated how accurately LB/TB can judge whether the events are safe or unsafe by comparing with their PET values. Then, system parameters are tuned to optimize the system performance for relevant design criteria.

4.5 Example Events

In the following, two examples with multiple POVs are considered. The first example contains two POVs. The SV turns between these POVs. In the second example, there are also two POVs, but the SV makes a left turn after both POVs leave the encroachment zone. In both examples, we assume thresholds $\Delta_{\mathrm{LB}} = -1\,\mathrm{s},\ \Delta_{\mathrm{TB}} = 2\,\mathrm{s}$ and hence the difference between these threshold is 3 s, which represents the thickness of the prohibited area across which the buffer bands cannot lie when the SV turns left.

In the first example, the PET of the POV1 (leader) was $-3.9\,\mathrm{s}$ and that of the POV2 (follower) was $1.32\,\mathrm{s}$. At $t = -1.17\ \mathrm{s}$, at which the POV2 was detected, $\mathrm{LB}_1 = -3.67\,\mathrm{s}$ and $\mathrm{TB}_2 = 1.34\,\mathrm{s}$. Thus, $\mathrm{LB}_1 < \Delta_{\mathrm{LB}}$, but TB_2 did not satisfy the second condition in expression (4.10). Consequently, although the SV actually turned between these POVs, it would have been advisable to have made the turn earlier, if possible; given the "late start" of the executed turn, and the parameters assumed above, the assistance system would naturally have advised against making this particular left turn.

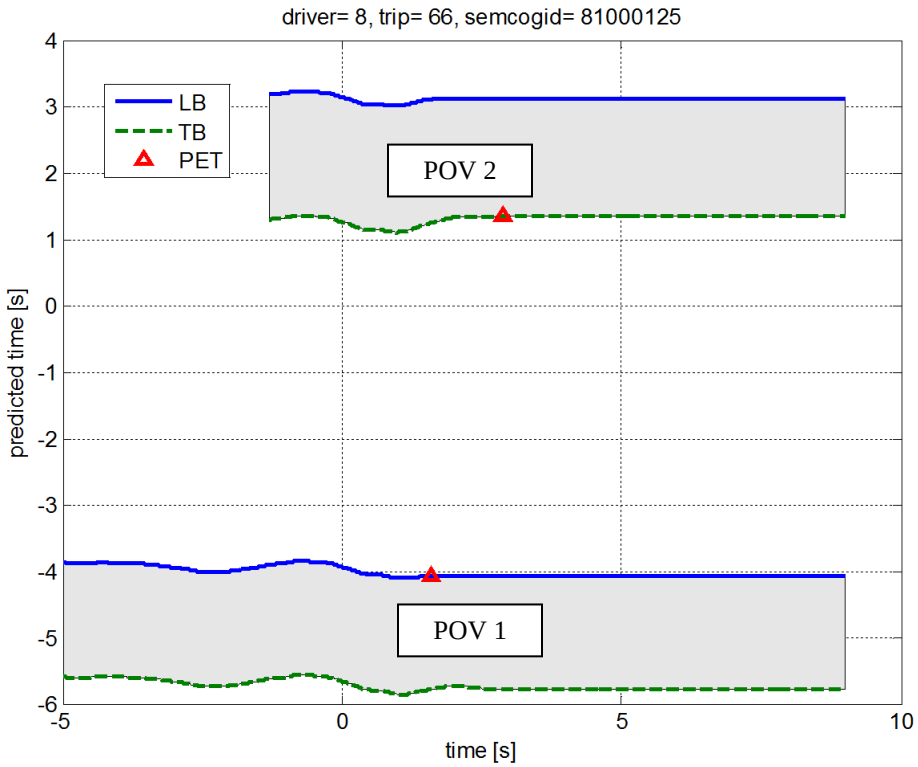

Figure 4.7 Buffer bands for two principal other vehicles (Example 1).

In the second example, both POVs crossed the encroachment zone earlier than the SV, so PET values of POV1 and POV2 were $-1.91\,\text{s}$ and $-0.32\,\text{s}$, respectively. In Figure 4.8, a noticeable difference from the last example can be seen in the overlapping region. This indicates the SV could not turn between these POVs since it is impossible to satisfy both of the conditions in expression (4.10). As a result, the SV crossed the encroachment zone after both the POVs did. At the initial time ($t = 1.01\,\text{s}$), the union set of the two buffer bands spread from $-2.57\,\text{s}$ to $1.41\,\text{s}$ – crossing the zero time and hence making the turn infeasible (Figure 4.8). As the SV waited, the whole band shifted downward until it became completely on the negative side at $t = 4.06\,\text{s}$. The SV started turning about $t = 4.8\,\text{s}$ as indicated by the change of the slope of the LB_2 curve and reached the conflict point at $t = 6.54\,\text{s}$ with $\text{PET} = -0.32\,\text{s}$ as described above.

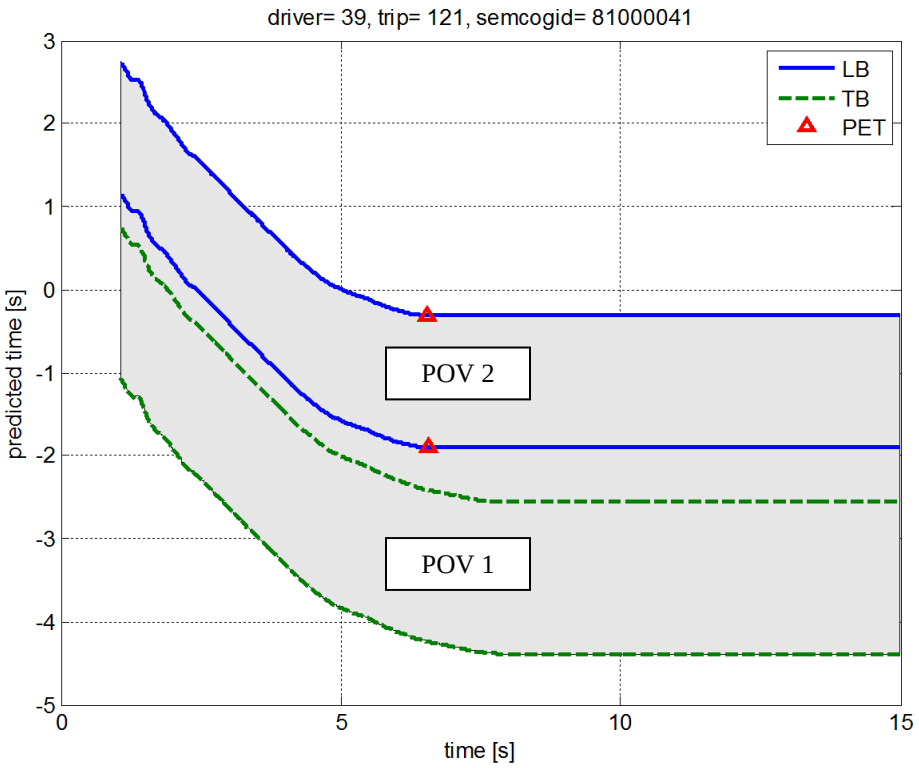

Figure 4.8 Buffer bands for two principal other vehicles (Example 2).

These two examples indicate a plausible analysis method for setting true gap acceptance where the gap is to be between a pair of POVs, not just a gap time relative to a single POV. In congested traffic conditions this is an important consideration, especially as the existence of a steady stream of oncoming traffic naturally leads drivers to look for gaps and potentially take risks to avoid what are perceived as excessive delays. Objective information on gap feasibility would undoubtedly help the driver, particularly if this information were available early to allow smooth execution of the turn.

4.6 Effect of Intersection Geometry on Reference Speed Profile

It may be reasonable to anticipate that the turning time varies depending on the intersection geometry since it affects the length and curvature of a turning path. In this section, a possible relationship between parameters for the intersection geometry and those for the reference speed profile is investigated.

The size of an intersection is specified by the lengths of segments connecting the intersection node and stop bar node and the shape is defined as the angle made by those segments. In Figure 5.4, point A is a stop bar node on a road on which the SV is initially located, point B is a stop bar node of the other road onto which the SV is turning, and point C is the intersection node. The length d_1+d_2, the sum of the lengths of segments AC and BC, is selected to indicate the intersection size, and the angle δ is the angle between those segments to represent the shape of the intersection.

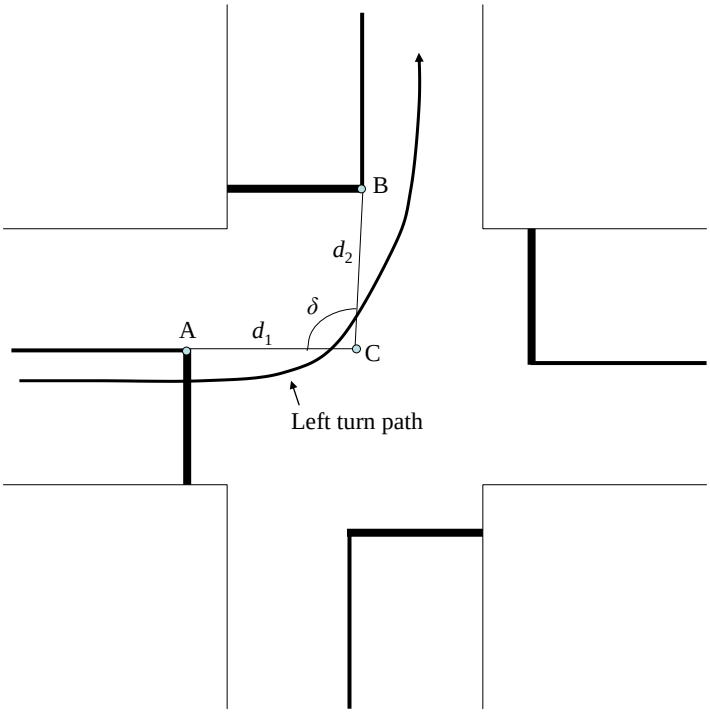

Figure 4.9 Intersection geometry.

Figure 4.10 shows relationships between the parameters for the reference speed profile, p_1, q_1, and U_{th} and those for the intersection, d_1+d_2 and δ. Note that p_1 and q_1 are acceleration values in the deceleration and acceleration phases during a left turn.

Contrary to the original expectation, neither the size nor shape of the intersection shows a clear and direct relationship to the parameters in the reference speed profile except for U_{th}, which becomes larger as d_1+d_2 increases or δ decreases. While it might be concluded that, within the range of intersections considered, the turning vehicle follows a uniform

reference speed profile, it is also clear that the variations in the parameters are large compared to the mean. These variations could be arising from sampling errors (since in many cases the samples are small), or from other factors such as road class, traffic density, presence of pedestrians, road roughness, lane marking quality etc. Most likely, both sources of variation are present, so the approach taken is to treat each intersection (and indeed each turning movement within that intersection) as a distinct case that requires the construction of a unique reference speed function.

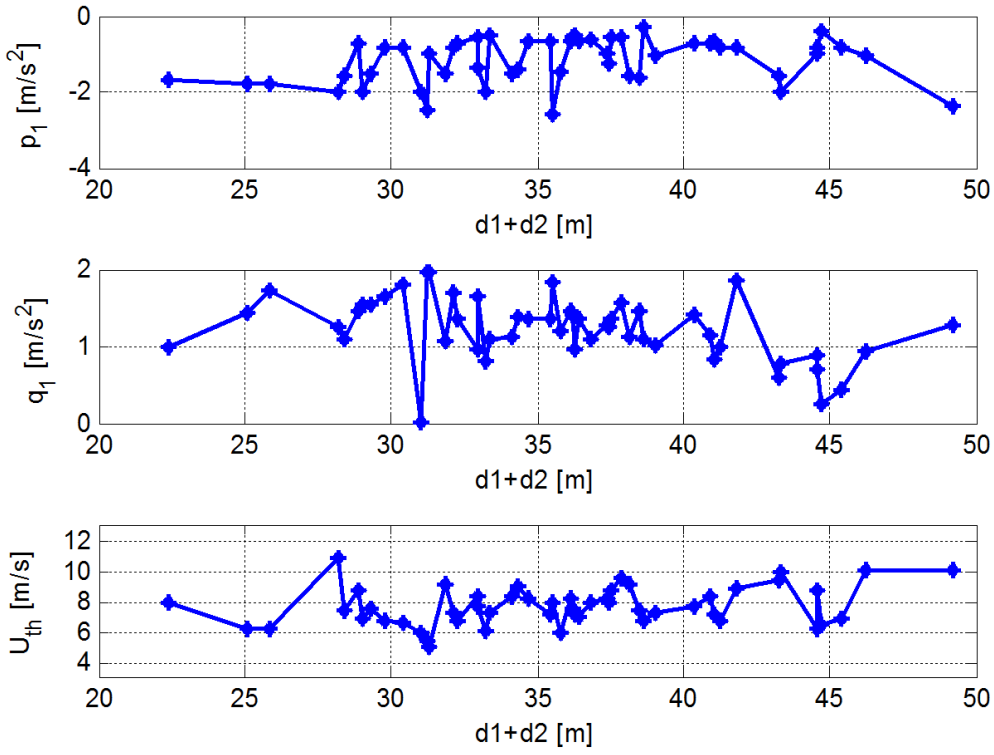

(a)

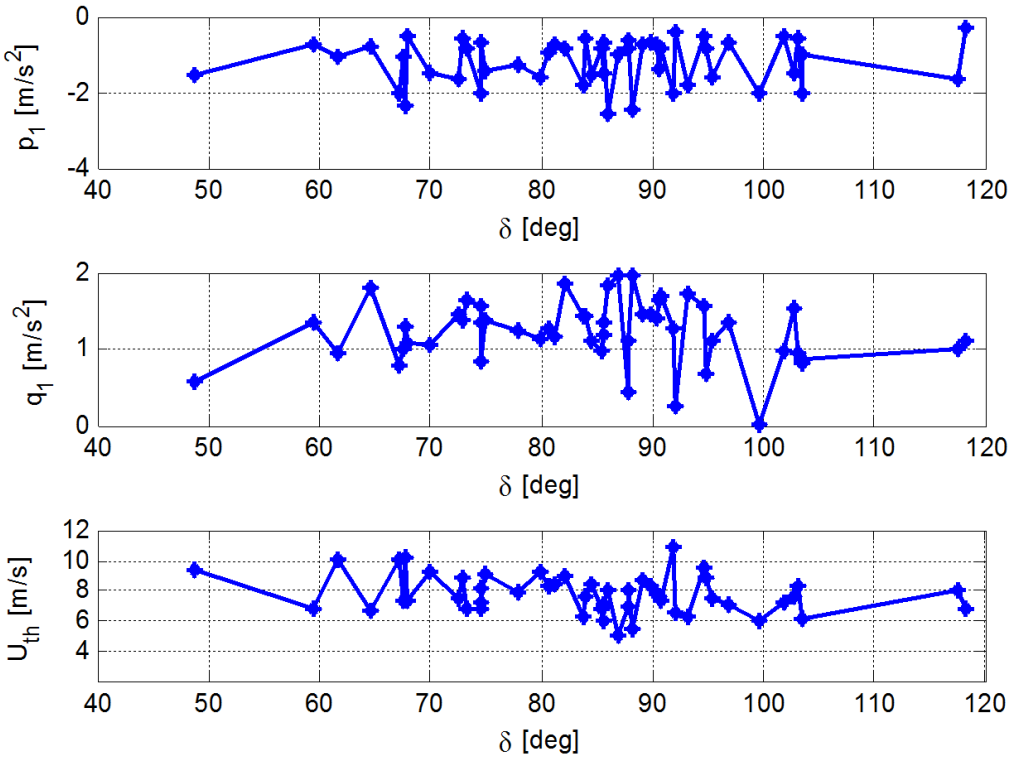

(b)

Figure 4.10 Relationship of the reference profile parameters with intersection geometry: (a) the intersection size and (b) shape.

Chapter 5
Driver Model for Intersection Left Turns

5.1 Overview

In this chapter, the driver model including both the longitudinal and lateral controls is constructed. The speed control model is based on the anticipated acceleration reference, $\hat{a}$, which is computed solely from visual preview information. The relationship between $\hat{a}$ and resulting vehicle accelerations are studied for both stopping and turning events using the naturalistic driving data. It unifies the two types of risks in controlling speed, braking to rest at the stop bar and turning left, by monitoring them at their respective preview points. A closed-loop model without the lateral control is used to tune the model parameters. The lateral control is based on a path following model in which a desired path to be followed is predetermined (Section 5.5). The driver cue for the control is the yaw rate error between the vehicle yaw rate and desired yaw rate at the preview point found from the visual cue.

In the following sections we define the anticipated acceleration reference (AAR), which may be based on lateral acceleration (AAR = $\hat{a}_y$), longitudinal acceleration (AAR = $\hat{a}_x$) or in some combined form $\hat{a}$. Detailed analysis of AAR and its contribution to a closed-loop control model are conducted. Section 5.2 focuses in more detail on the overall speed control model, and the concept and definition of AAR. In Section 5.3, AAR time-histories are extracted and analyzed for both straight-line braking to rest and for making intersection left turns. In Section 5.4, system identification is conducted, optimizing closed-loop simulations against measured driving data; in this way real-world parameter ranges are determined. Section 5.5 shows Monte Carlo simulations using a full simulation

model which is enhanced to include a detailed vehicle model and steering control of the driver in addition to the speed control. Section 5.6 summarizes additional important characteristics of left turning drivers and briefly considers the possibility of extending AAR to model speed control in curves.

5.2 Speed Control Based on Anticipated Acceleration Reference

As mentioned above, for unprotected intersection left turns, the driver is aware of two possible outcomes – braking to rest if there is no sufficient gap (or if the signal changes to red), or reducing the speed to be low enough to attempt the turn. During the intersection approach, both outcomes may be anticipated simultaneously. Perception of acceleration is a primary factor relevant to speed choice; for example, the human drivers accept higher lateral accelerations in a fixed-base driving simulator compared to a motion-base counterpart [32]. Here it is a basic modeling hypothesis that speed control during the approach to an intersection is directly related to *anticipation* of lateral or longitudinal acceleration. It is assumed that this reference is repeatedly updated based on current speed and distance information, and is also defined in a way that is common to both stopping and turning. The need for a suitable reference is clear – it enables a driver to avoid excessively high speed leading to severe braking or turning to avoid collisions with other vehicles or fixed obstacles. On the other hand, excessively slow approach speed causes delay, possible frustration for passengers, as well as for drivers of following vehicles.

We classify a left turn into three stages: (a) *approach* stage, where speed is mostly reduced and lateral accelerations are small (b) *turn* stage, where lateral accelerations dominate over longitudinal accelerations, and (c) the *exit* stage when forward acceleration in positive and path curvature is progressively reduced. As mentioned above, the anticipated acceleration reference (AAR) takes account of the possibility that either a turn is made or the vehicle is to be brought to rest – simultaneously addressing potential longitudinal and lateral conflicts. One or both of the anticipated accelerations may be active in the control loop at any time *t*, and we denote this by $\hat{a}(t)$.

Figure 5.1 shows a block diagram of the overall longitudinal control system. Here the vehicle is simply represented as a pair of integrators ("longitudinal vehicle dynamics") with input equal to the applied acceleration; this simple model is considered sufficient for identification and validation of the driver model. On the other hand, for detailed simulation a more realistic model will be used in Section 5.5. The driver's control signal u_x equals the rate of pedal motion (brake or accelerator pedal) which conveniently assigns $u_x = 0$ when speed is kept constant. The saturating integrator converts pedal motion to applied vehicle acceleration, taking account of limited friction and engine power.

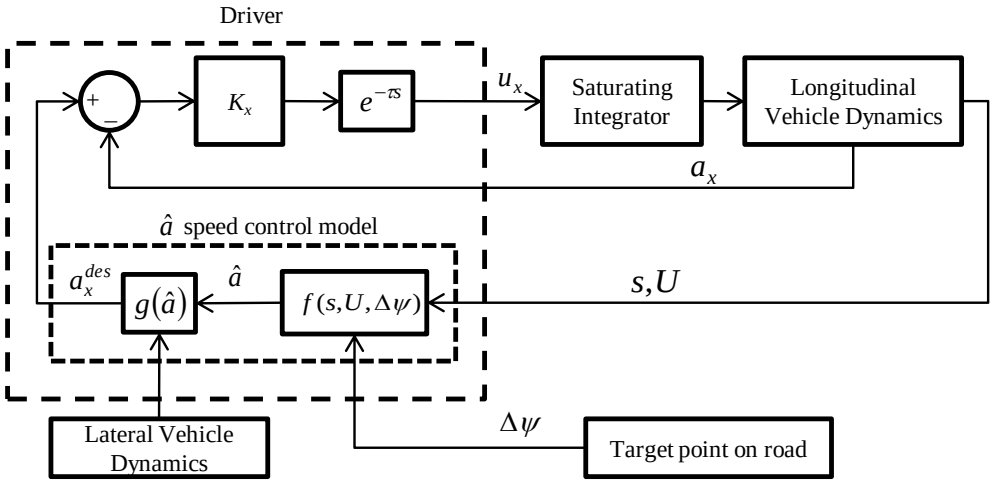

Figure 5.1 Block diagram of the closed-loop model.

The upper half of the driver control block ("driver") is simply a proportional gain K_x combined with a time delay τ, having transfer function $e^{-\tau s}$. In the lower half is the speed control model which outputs a desired longitudinal acceleration a_x^{des}; the difference between this and the forward acceleration a_x from the vehicle is fed back into the proportional gain and time delay. The sub-model for desired acceleration, $a_x^{des} = g(\hat{a}, a_y)$, determines how quickly the driver wishes to respond to changes in anticipated acceleration (and current lateral acceleration a_y, where relevant); this is

formulated in Section 5.4. Now we focus on the anticipated acceleration sub-model for AAR, $\hat{a} = f(s, U, \Delta\psi)$.

AAR is initially defined based on anticipation of making a future turn, given the current vehicle speed *U*. The expression for $\hat{a}$ includes *s* to represent the longitudinal position of the vehicle on its path. The severity of the turn is represented by the change in heading angle, $\Delta\psi = \psi_Q - \psi$, between the current value ψ and a future value ψ_Q; *Q* is the driver's chosen target point (Figure 5.2). For a left turn at a simple 4-leg intersection we expect $|\Delta\psi| = |\psi_Q - \psi| \approx 90^\circ$, assuming the target point is chosen close to the exit of the intersection and the target direction is parallel to the exit road. However, the model will also use smaller values of $|\Delta\psi|$, especially if the vehicle has begun to turn and the target point is somewhere near the apex of the turn. *Q* is notionally the gaze point where the driver directs his or her visual attention, and this is expected to be updated, especially during the turn phase. Based on an assumed constant rate of turn (Figure 5.2) we easily obtain the equation:

$$\hat{a}_y = \frac{U^2}{R} = \frac{2U^2 \sin(|\Delta\psi|/2)}{d} \tag{5.1}$$

where $d = |PQ|$ is the distance to the target point and *R* is the radius of turn. Here *d* depends on position *s* and the strategy adopted by the driver for selecting *Q*. For simplicity we assume that the driver selects *Q* so that a constant radius path is feasible or reasonably anticipated. Note that this definition of AAR is determined by immediately available visual information; it requires no predictive analysis (e.g. prediction of speed changes or estimating future vehicle motion) and is available even when the vehicle is being driven on a straight line path – it is only necessary to *anticipate* turning, by selecting a target point, for its use to be feasible.

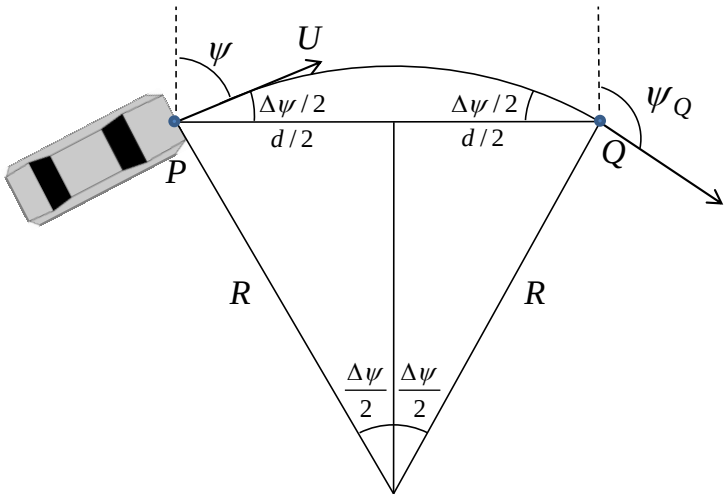

Figure 5.2 Geometry for $\hat{a}$ calculation based on circular path and constant speed.

Equation (5.1) requires no complex analysis of vehicle dynamics or prediction of combined slowing and turning. There is no expectation that the driver actually computes this formula; since it is simple and kinematically-based, it is reasonable to assume a driver builds a corresponding associative map between the visual stimulus derived from $(U, \Delta\psi, d)$ and the following response $\hat{a}_y$, based on repeated experience, including driving through curves and through experience as a passenger. Equation (5.1) is then a mathematical expression approximating such a map.

There is a similarity between this expression for $\hat{a}_y$ and the required deceleration for the simpler case of speed control for braking to rest. In [36] Levison presents a stopping distance model where the driver is assumed to predict the constant acceleration required to brake to rest. In this case the required acceleration becomes a longitudinal acceleration reference

$$\hat{a}_x = \frac{U^2}{2d}. \tag{5.2}$$

The same reference was previously shown to be applicable to straight-line braking by Lee [69], in this case based on the concept of a constant "tau-dot" strategy. In the present

paper, equations (5.1) and (5.2) are interpreted in a consistent manner: the driver is presumed to react and reduce speed once the anticipated acceleration (or deceleration) reaches a critical limit, and brake pedal effort is continuously modulated to prevent $\hat{a}$ (i.e. $\hat{a}_x$ or $\hat{a}_y$ as appropriate) exceeding this limit. Again, the learning process for equation (5.2) is presumed to be similar to that of equation (5.1) – based on visual preview and learned over many similar events. Comparing (5.1) and (5.2), the two reference accelerations become equal for a particular change in yaw angle:

$$\frac{2U^2 \sin\left(|\Delta\psi|/2\right)}{d} = \frac{U^2}{2d} \tag{5.3}$$

or

$$|\Delta\psi| = d\psi_0 \equiv 2\arcsin(\tfrac{1}{4}) \approx 29° \tag{5.4}$$

When considering the intersection approach stage, we assume that both AAR values are monitored simultaneously by the driver, though only one should be active in the control loop. If one AAR reference renders the other irrelevant (e.g. stopping is possible so speed can be sufficiently reduced for turning) we say it is *dominant*. We also assume that the gaze point for stopping (expected to be near the stop bar) and turning (expected to be closer to the planned intersection exit) may be different, and denote them as Q_x and Q_y respectively.

For heading angle changes less than $29°$, deceleration based on $\hat{a}_y$ can be less severe than for stopping, while for $|\Delta\psi| > 29°$ the dominant strategy is to act as if braking to rest is required. During the initial approach to a typical intersection, we expect the latter case to hold (target points, or expected "gaze points", for stopping and turning are close together and $|\Delta\psi| > 29°$). Later, in close proximity to the turn, the target point Q_y may be further away than Q_x. As long as $\hat{a}_x < \hat{a}_y$ no firm decision is required from the

driver; since stopping is feasible, speed can be reduced to zero, and therefore made sufficiently small to eventually complete the turn. However, at a crossover point, where $\hat{a}_x = \hat{a}_y$, it becomes necessary to commit to turning or stopping; higher speeds can be maintained for turning than for stopping and (assuming there is no obstacle to turning) $\hat{a}_y$ provides the dominant strategy.

Thus, we propose there is a switch in driving mode, from approach stage to the turn stage, at the crossover point where the values of $\hat{a}_x$ and $\hat{a}_y$ are equal. In Section 5.3, we test this idea using naturalistic driving data. To be specific, Q_y is selected at a pre-defined location, where the vehicle path reaches the lane centre adjacent to the stop bar of the exit road; ψ_{Q_y} is defined by the direction of the exit road. On the other hand, Q_x is obtained by a best-fit procedure: it is placed at the stop bar of the entry road, and then the precise location is adjusted to minimize the difference between the maxima of $|a_x|$ and $\hat{a}_x$ during the approach stage.

Additionally, the second driving mode switch, from the turn stage to exit stage, is assumed to be at the point of maximum curvature in the naturalistic driving data. Equivalently, for use in the closed-loop simulation model (Section 5.5), switching takes place when the steering angular velocity is reversed. The exit stage is included for completeness, and is not reliant on the AAR model.

The point of the second mode switch was selected from three possible variables: 1) point of maximum curvature, max|*c*|, 2) maximum yaw rate, max|*r*|, and maximum lateral acceleration, max|a_y|. For each of these, the offset values were measured from manually-detected exiting points of actual free left turns. Each of the manually-detected exiting points was found at the point at which $a_x = 0\,\text{m/s}^2$ after starting to release the brake pedal. Resulting distributions (Figure 5.3) show that the one with respect to max|*c*| location has the sharpest and the closest peak to $0\,\text{m}$. Therefore, max|*c*| was selected as the onset point of the exit stage. The mean and standard deviation are $-0.19\,\text{m}$ and $6.13\,\text{m}$, respectively.

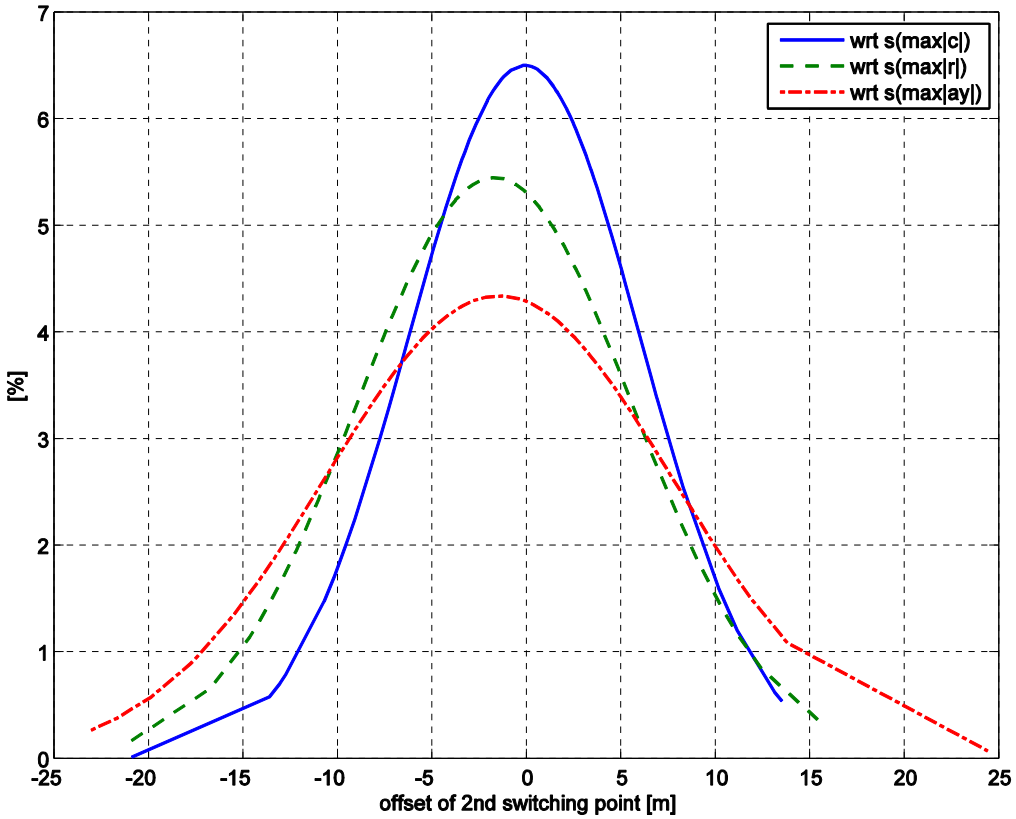

Figure 5.3 Distributions of offsets of selected measurements for the exit stage.

5.3 Calibration of the Speed Control Strategy

In this section the full speed control model of Figure 5.1 is not used; rather the reference $\hat{a}$ is computed directly from the naturalistic driving data to test whether it is suitably controlled by human drivers, and hence can be validated as a plausible control reference.

5.3.1 Braking to Rest

Figure 5.4 shows a comparison between $\hat{a}_x$ and vehicle longitudinal acceleration a_x for an event involving braking to rest at the stop bar for a red traffic signal. In this example, there was an initial coast-down deceleration of 0.5 m/s^2 due to aerodynamic and other drag effects, followed by actual braking at around $s = -107\,\text{m}$. Braking started when $\hat{a}_x$ reached approximately $1.45\,\text{m/s}^2$ and it can be seen that $\hat{a}_x$ was regulated between an upper bound ($1.7\,\text{m/s}^2$) and lower bound ($1.4\,\text{m/s}^2$) until the vehicle speed became slow near the stop bar. These upper and lower bounds were determined as the maximum and

minimum decelerations respectively between the time of first brake application and the time when the vehicle was within 5 m of the final stopping location. The last 5 m before stopping was excluded since the control of speed and acceleration are highly variable in close proximity to the stopping point. It is especially important to note that while the reference $\hat{a}_x$ is controlled within tight limits the actual vehicle acceleration fluctuates considerably. This suggests that $\hat{a}_x$ is a plausible control reference, while other dynamics may generate larger variations in actual vehicle response. Similarly, even though equation (5.2) is derived from constant decelerations, the vehicle deceleration is far from being constant at all times. The example shown is typical of many straight-line braking events, but it should be noted that there exist individual cases do not fit the model so well. We return to the question of driver variability and goodness of fit when considering the full model for intersection left turns (Section 5.4).

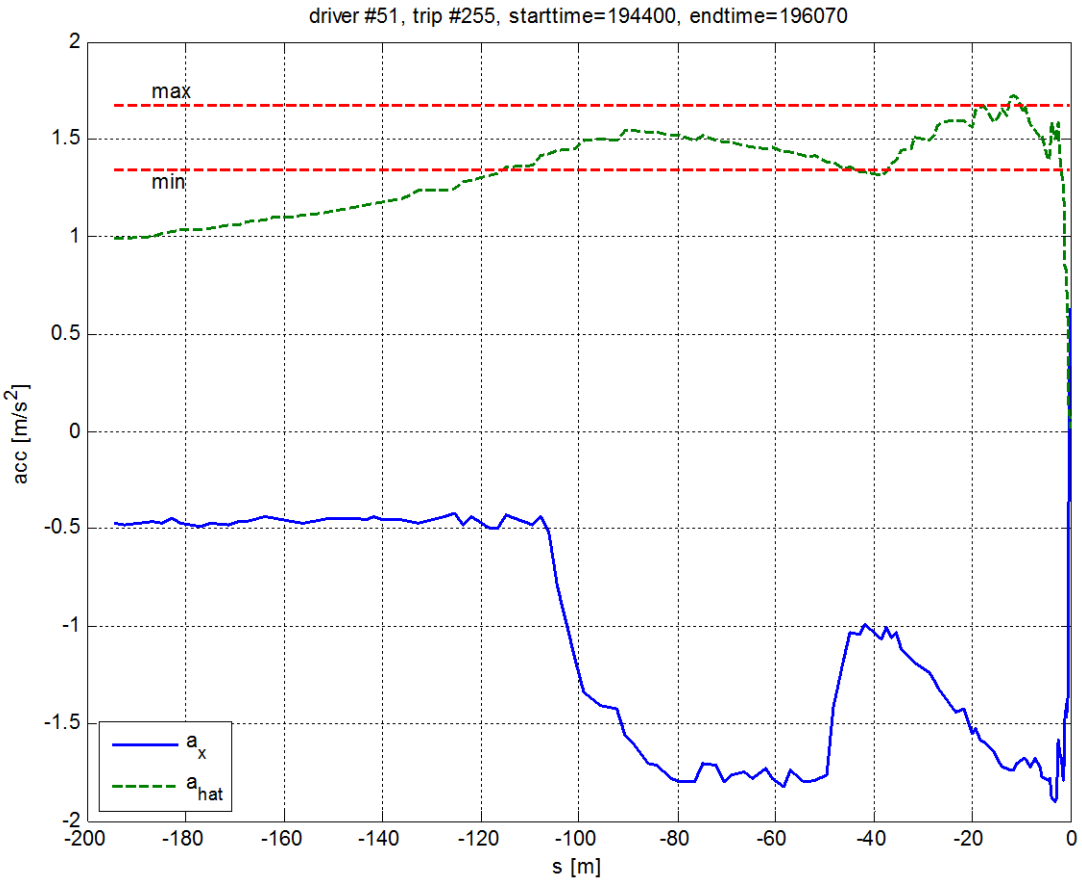

Figure 5.4 Vehicle acceleration a_x and anticipated acceleration $\hat{a}_x$ for an event of braking to rest. (note: for consistency, $\hat{a}$ is shown positive)

5.3.2 Intersection Left Turns

For a selected left turn event, Figure 5.5 shows an aerial photograph of the intersection and the measured vehicle trajectory; review of video recorded from an onboard camera confirmed the absence of other traffic etc. that might bias the speed control. The circle shows the assumed location of Q_x (target point for $\hat{a}_x$) and the triangle denotes the assumed position of Q_y located next to the stop bar. In addition, the squares indicate the start and end locations of the turn motion, defined as the interval when yaw rate *r* satisfies the condition $|r| \leq 0.1$rad/s.

(a)

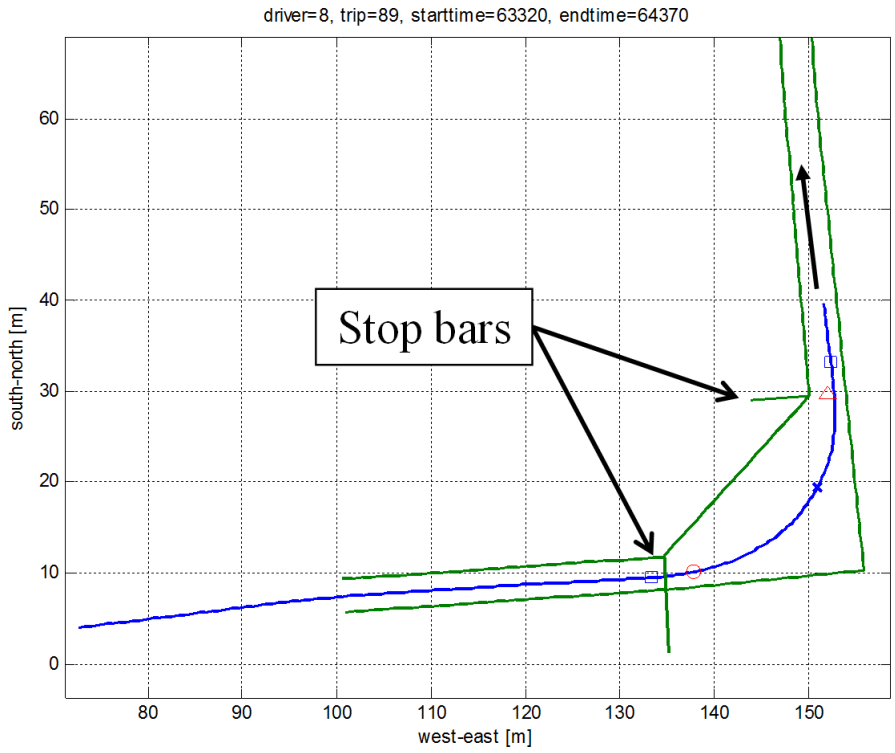

(b)

Figure 5.5 Example intersection left turn: (a) aerial photo of the intersection and (b) free turn vehicle path with the path boundaries. (○: first gaze point, △: second gaze point, ×: point of maximum curvature, ☐ = left turn start and end locations)

Figure 5.6 shows the traces of a_x, a_y, $\hat{a}_x$ and $\hat{a}_y$ for this event, with path longitudinal distance *s* used as independent variable. The markers are the same as for Figure 5.5, with the addition of the diamond to show the crossover between $\hat{a}_x$ and $\hat{a}_y$. The approach stage is based on the same model as the braking-to-rest event as shown by $\hat{a}_x$. It can be confirmed that the trend in $\hat{a}_x$ is very similar to that in Figure 5.4, i.e. $\hat{a}_x$ saturates at a value close to the actual peak deceleration value. As seen in the figure, in the approach stage, $\hat{a}_x$ is dominant until the crossover is reached at $s = 53\,\text{m}$, which closely corresponds to the timing of releasing the brake pedal. Then, the "threat" from $\hat{a}_y$ becomes dominant and the turn stage starts with the speed control based on $\hat{a}_y$. Finally, the exit stage begins at the × located at about $s = 82\,\text{m}$. In the figure, $\hat{a}_x$ and $\hat{a}_y$ become indeterminate close to their respective gaze points, and the computation shows this

tending to infinite values; neither case affects the control and for clarity the limit points are shown at $\hat{a} = 0$.

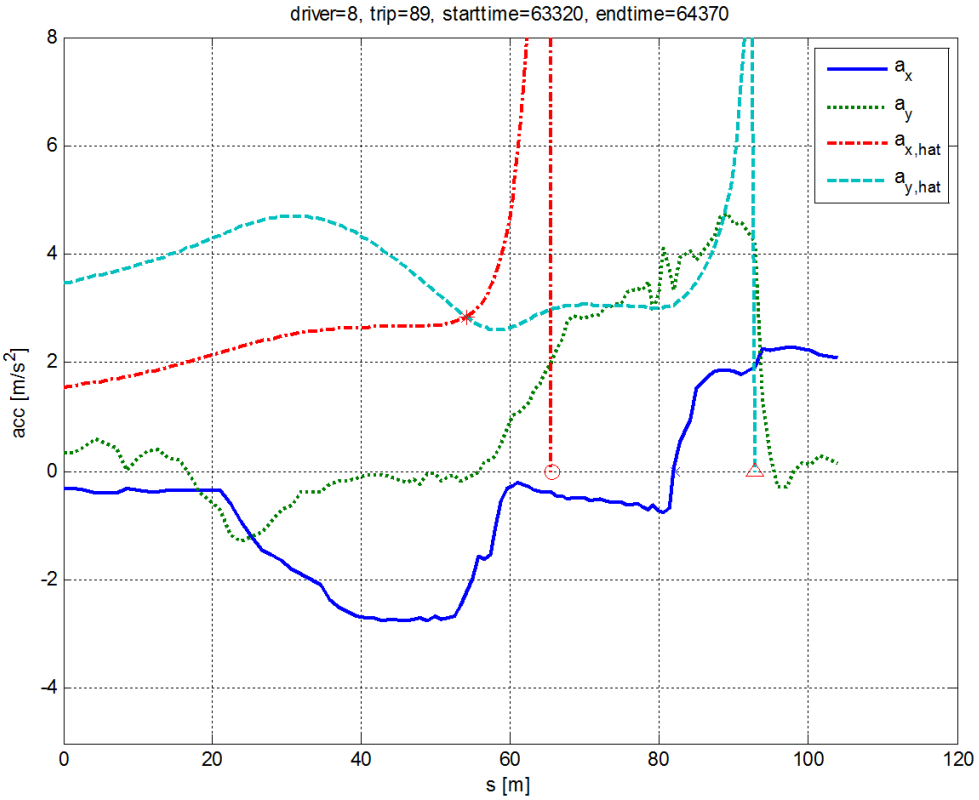

Figure 5.6 Acceleration plots for a left turn event.

5.4 System Identification and Validation of the Speed Control Model: Closed-loop System Dynamics

In this section we complete the definition of the full speed control model of Figure 5.1 and apply parameter optimization to estimate model parameters. The MATLAB® function *fminsearch* was used to minimize the sum of squared errors between the speed responses from the simulation and driving data. Two example cases are presented for each type of maneuver, braking to rest and left turn, and further results are analyzed from a larger event set.

5.4.1 Feedback Control Model

To support parameter estimation and validation, the simple vehicle model from Section 5.2 is included, while a measured trajectory is used to constrain the degree of freedom of lateral motion. Referring to Figure 5.1, the inner loop includes the driver delay, $\tau = 0.2\,\text{s}$. The desired acceleration a_x^{des} is derived from $\hat{a}$ via a piecewise-linear control function *g*(.) in the outer feedback loop. This is essentially a proportional control, but includes saturation at the upper and lower limits. For the approach phase it assumes the driver has lifted the accelerator pedal, generating a gentle coast-down deceleration a_0. As shown in Figure 5.7, when $\hat{a}$ exceeds a certain threshold, *lb*, a_x^{des} decreases below a_0 and the brakes are applied. Proportionality holds until an upper bound (*ub*) on $\hat{a}$ is reached, at which point the demand is saturated, limiting the maximum braking effort to a level the driver is assumed comfortable with. Similar functions are used for the approach and turn stages, though for the turn stage positive values of a_x^{des} can be required, and the driver may react to both actual and anticipated lateral accelerations, so the input variable $\max(\hat{a}_y, a_y)$ is used in place of $\hat{a}_y$ – see Figure 5.7. To best match the data, independent parameters are used according to the two stages.

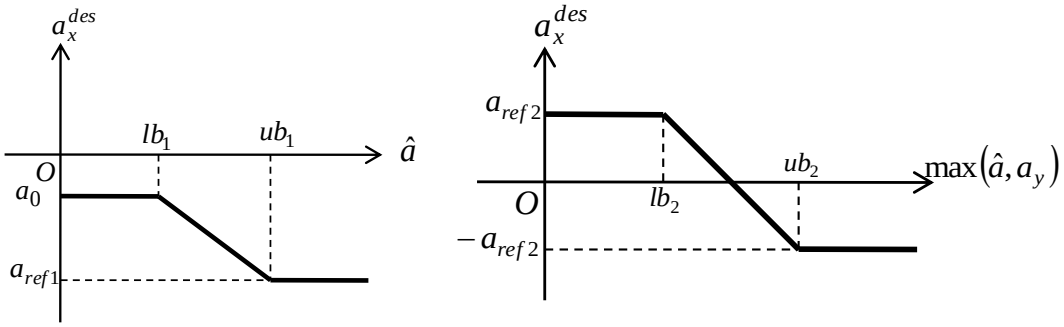

(a) **(b)**

Figure 5.7 Nonlinear control function g(.): (a) the approach stage and (b) turn stage.

Coast-down decelerations is obtained from a polynomial function

$$a_0(U) = c_1 + c_2 U + c_3 U^2 \tag{5.5}$$

This accounts for deceleration due to engine torque when the accelerator is not depressed, as well as rolling resistance and aerodynamic drag. Model parameters are determined by least-squares fitting to several events (all using the same vehicle type) to obtain: $c_1 = -105.2\ \mathrm{ms}^{-2}$, $c_2 = -16.70\,\mathrm{s}^{-1}$ and $c_3 = -0.4789\ \mathrm{m}^{-1}$.

For completeness, speed control is applied at the exit stage, but this is not a primary focus of this paper; in fact $\hat{a}$ and a_y both tend to zero as the vehicle completes the turn, so additional driver attributes determine behavior in this third stage. For the exit stage a constant desired acceleration is assumed:

$$a_x^{des} = a_3 \tag{5.6}$$

All initial conditions for simulations (position, speed and acceleration) were obtained directly from the driving data at the start time of the chosen event.

5.4.2 Braking to Rest at Stop Bar

Two example cases were analyzed, and resulting parameter values are given in Table 5.1; corresponding plots are shown in Figure 5.8 and Figure 5.9. The horizontal lines in Figure 5.8(c) and Figure 5.9(c) specify the locations of ub and lb. It is worth noting that ub and lb are the *model parameters* mentioned in Section 5.4.1 and are not expected to coincide with the upper and lower bounds of Figure 5.4. In a braking to rest scenario, only one speed control mode exists, i.e. the approach stage, so Table 5.1 comprises a reduced set of parameters. As shown in the figures, the model can fit the data very well. In these results, $\hat{a}$ is controlled around $1.5\,\mathrm{m/s^2}$ and $1.1\,\mathrm{m/s^2}$ respectively until the release of the brake pedal is initiated.

Table 5.1 Driver parameters for braking to rest.

Symbol	Quantity	Value	
		Ex. 1	Ex. 2
K_x [s^{-1}]	proportional gain	0.723	0.873
ub_1 [m/s^2]	upper bound of the desired $\hat{a}$ range	1.47	0.993
lb_1 [m/s^2]	lower bound of the desired $\hat{a}$ range	1.19	0.840
a_{ref1} [m/s^2]	lower saturation value of the saturation block	−1.66	−1.09

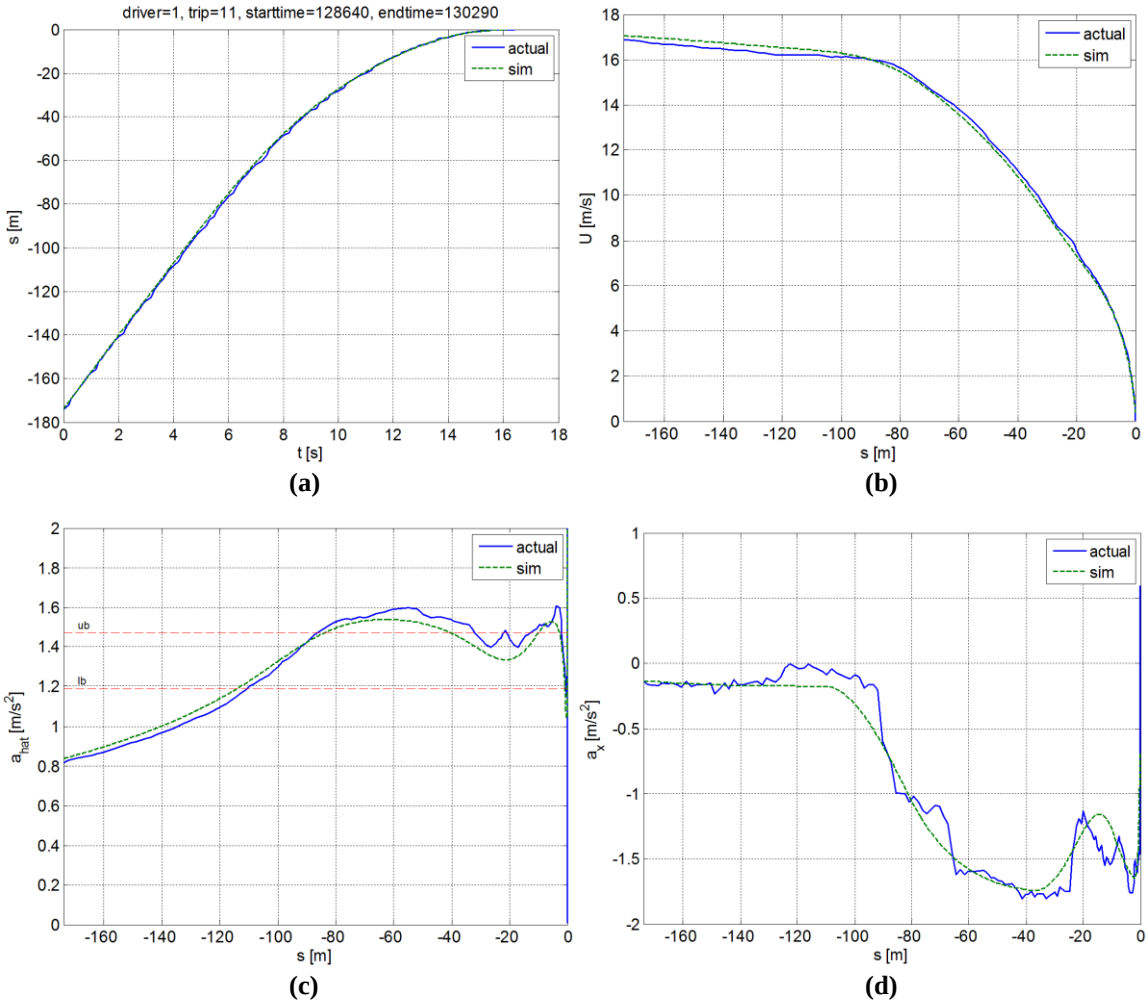

Figure 5.8 Simulation results for braking to rest (Example 1).

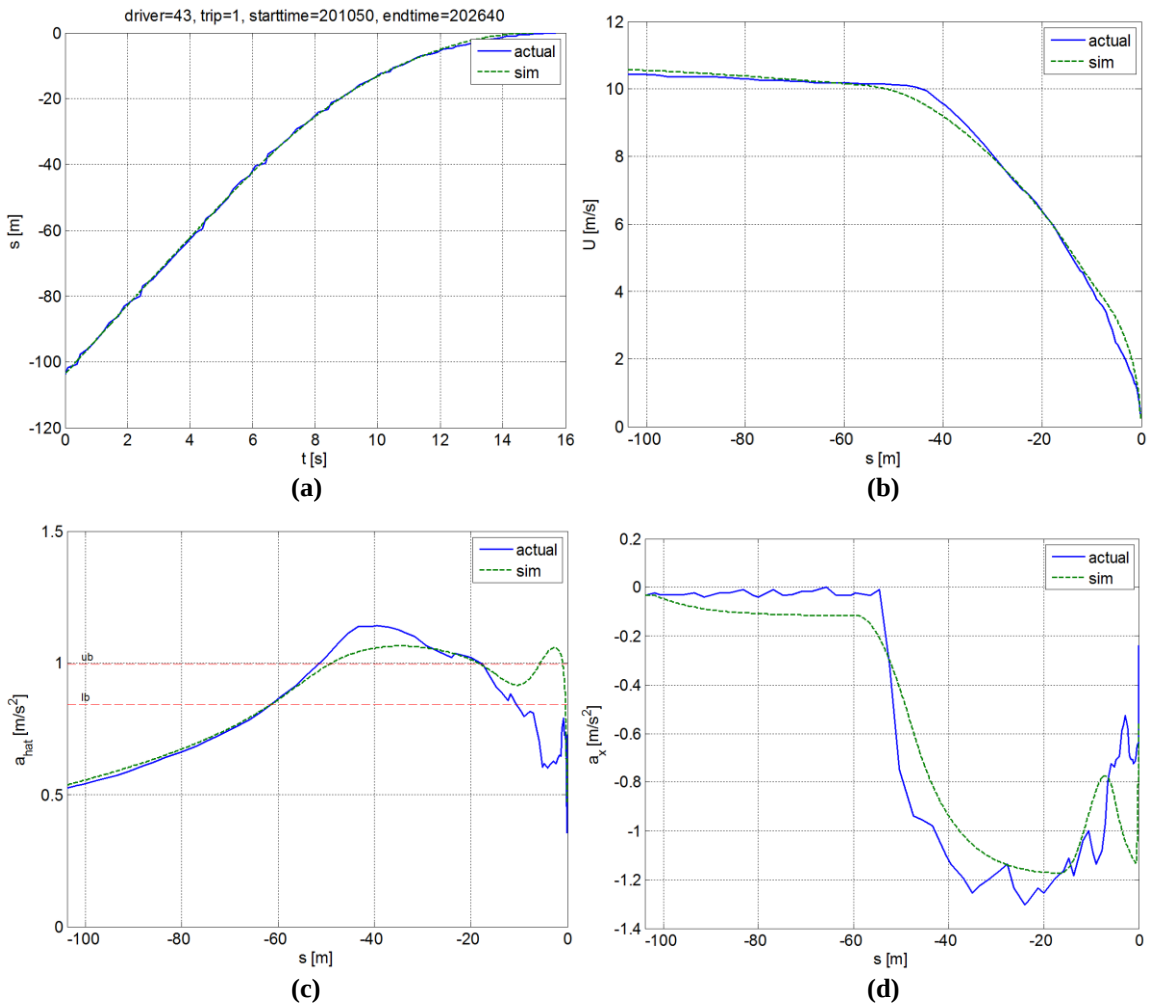

Figure 5.9 Simulation results for braking to rest (Example 2).

5.4.3 Intersection Left Turns

Similar results from LTAP/OD events are shown in Figure 5.10and Figure 5.11. The measured vehicle path is assumed, and now two sets of parameters are optimized (one for approach and one for turning), plus a_3 for the target exit acceleration. The resulting parameter values for this example are given in Table 5.2. While it is hard to exactly match vehicle longitudinal accelerations with the simple vehicle model, the overall match between measurement and simulation is again seen to be very good. Crucially, the model respects the crossover point, when $\hat{a}_x = \hat{a}_y$, which almost exactly matches the timing of crossover in the experimental data. This is in spite of the fact that gaze point Q_y was

fixed *a priori* (near the stop bar on the exit road, see Section 5.2) and not estimated from data.

Regarding the parameter values, those in Table 5.2 are significantly larger than those in Table 5.1, the events being under different conditions and with different drivers. Clearly, the measured vehicle decelerations are also larger in the left turn events than in braking to rest, suggesting that different control thresholds are employed. It might be that the driver's sense of urgency or risk is very different between the two cases. Another factor may be the greater need for precision in longitudinal positioning when braking to rest, and therefore a more conservative set of acceleration thresholds are used. Even though the parameters ranges are different, the same mechanism, based on AAR, give results that are consistent between the two driving situations.

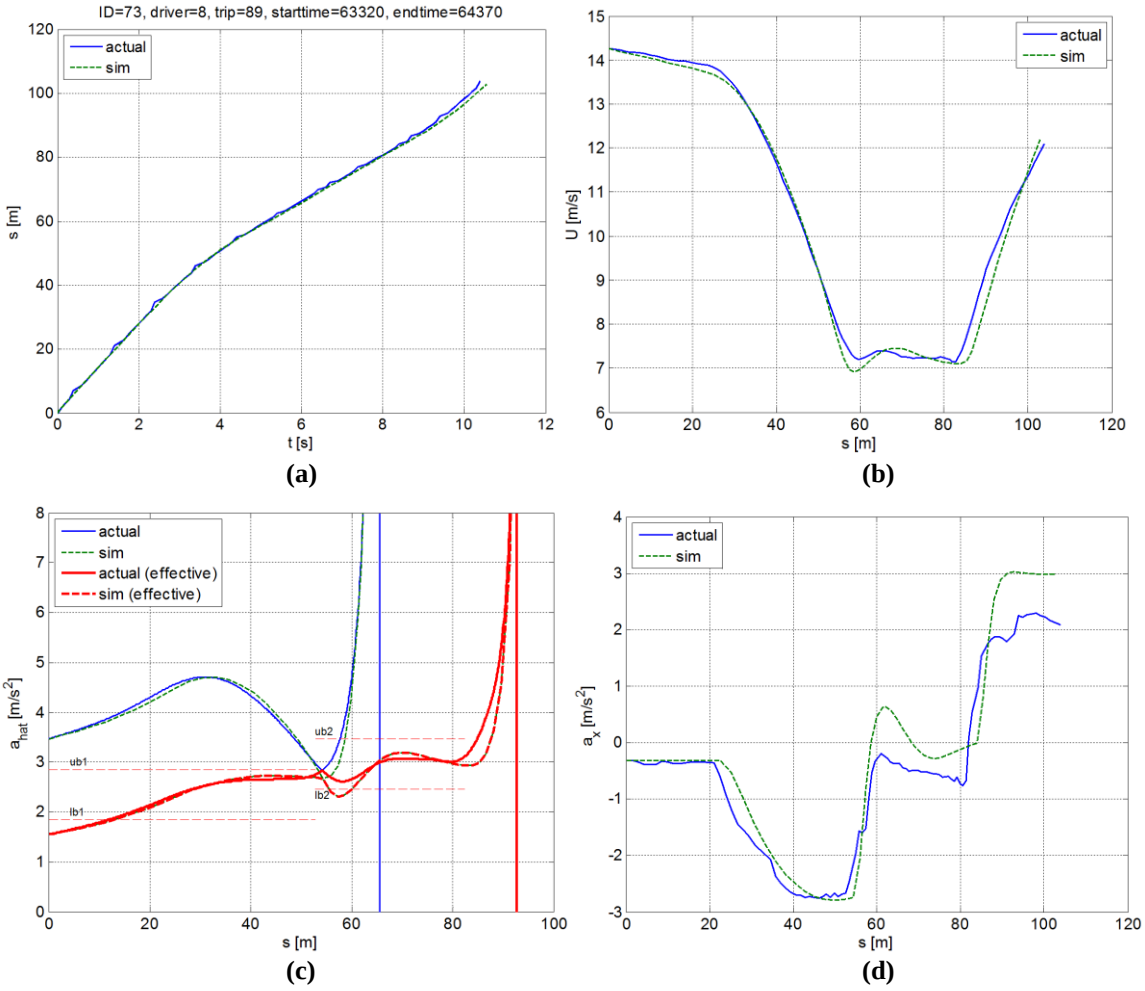

Figure 5.10 Simulation results for left turn (Example 3).

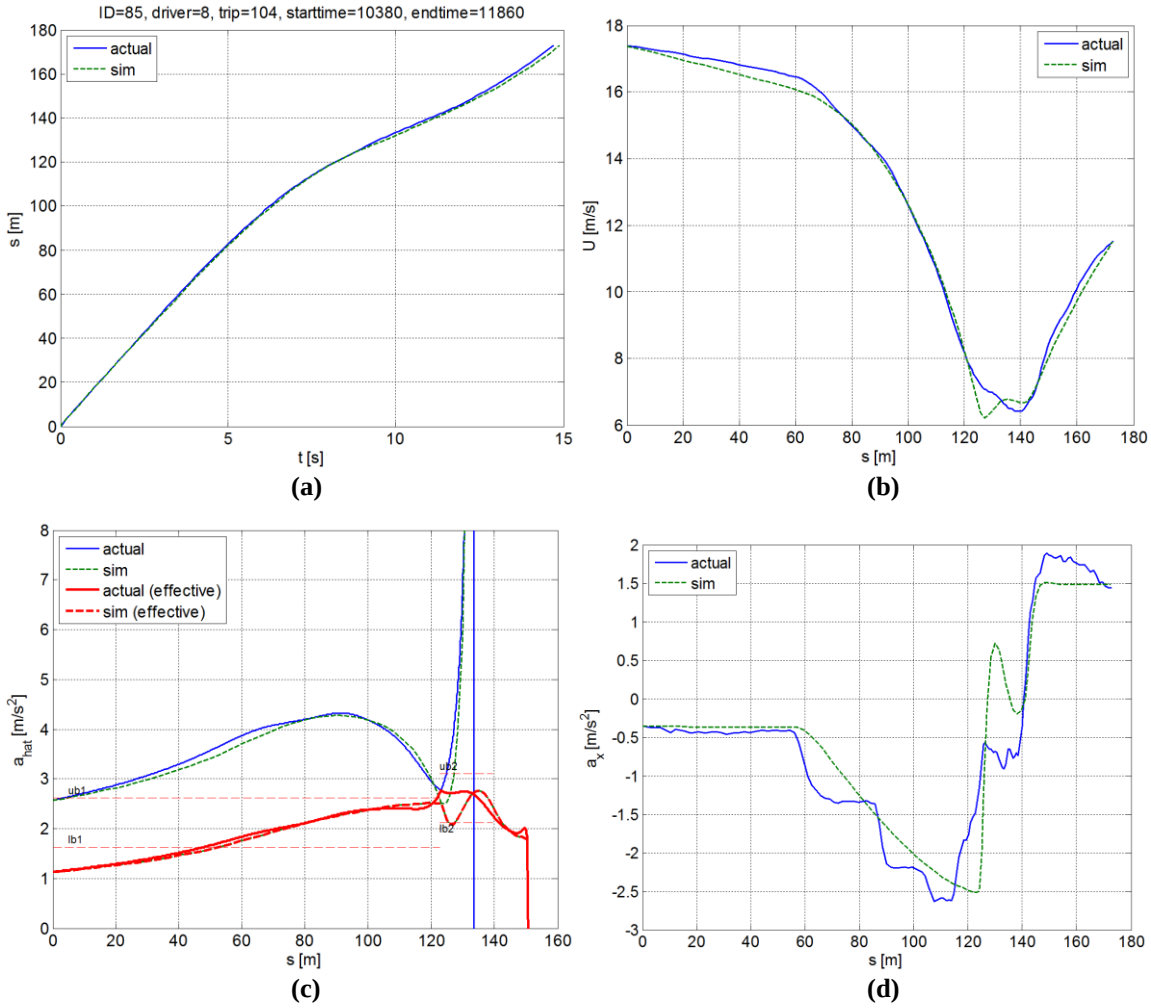

Figure 5.11 Simulation results for left turn (Example 4).

Table 5.2 Driver parameters for left turns.

Symbol	Quantity	Value	
		Ex. 3	Ex. 4
K_x [s^{-1}]	proportional gain	2.18	2.18
ub_1 [m/s^2]	upper bound of the desired $\hat{a}_x$ range	2.85	2.62
lb_1 [m/s^2]	lower bound of the desired $\hat{a}_x$ range	1.85	1.62
ub_2 [m/s^2]	upper bound of the desired $\hat{a}_y$ range	3.46	3.11
lb_2 [m/s^2]	lower bound of the desired $\hat{a}_y$ range	2.46	2.11
a_{ref1} [m/s^2]	lower saturation value of the saturation block (approach stage)	−3.14	−2.77
a_{ref2} [m/s^2]	saturation value for the turn stage	0.602	0.748
a_{ref3} [m/s^2]	constant desired acceleration for the exit stage	2.98	1.49

5.4.4 Extended Event Sets

In the above we have seen that speed and other variables match well to selected measured events, and use this as evidence that AAR may faithfully reproduce human control behavior. On the other hand, human behavior is immensely variable, and we cannot expect to capture every event with high fidelity. Now we consider 108 straight-line braking events, randomly sampled from a large number (3927) of such events in the database. Similarly, for free left turns, an initial random selection of 81 events was made. Of these, 26 events were selected because they occurred at a set of eighteen intersections for which lane boundaries and stop bar locations had been digitized; Figure 5.5 shows one such example. No other criteria were applied in the selection process, and *no events were removed based on model fitting performance*. Comparisons between measurement and fitted model are given in Figure 5.12, which shows cumulative distributions of the root mean square error (RMSE) in speed for these events: (a) the 108 straight-line braking events, (b) the 26 free left turn events. The error is defined:

$$RMSE = \sqrt{\sum_{i=1}^{N} e_i^2 / N} \tag{5.7}$$

where e_i is the error between the speeds in simulation and measurement at the *i*-th positional point on the road, spanned by average intervals of about 1.4 m; *N* is the resulting number of data points in an event in either data set. For both types of event, RMSE is mostly less than 1 m/s (roughly 90% of cases have RMS error less than 1 m/s). This indicates that the previous examples are not especially unique. It appears that in the absence of extraneous factors (e.g. major visual distractions or competing influences on the driver) the AAR model is capable of representing the variety of human speed control behavior when making intersection approaches.

Traditionally, after system identification, an independent set of data would be used to validate the model; but with human driver modeling it is not reasonable to expect that a fixed set of parameters will apply across many events. Therefore, instead, we consider

comparisons between Monte Carlo simulations (using the parameter ranges obtained above) and make comparisons at the level of the resulting population.

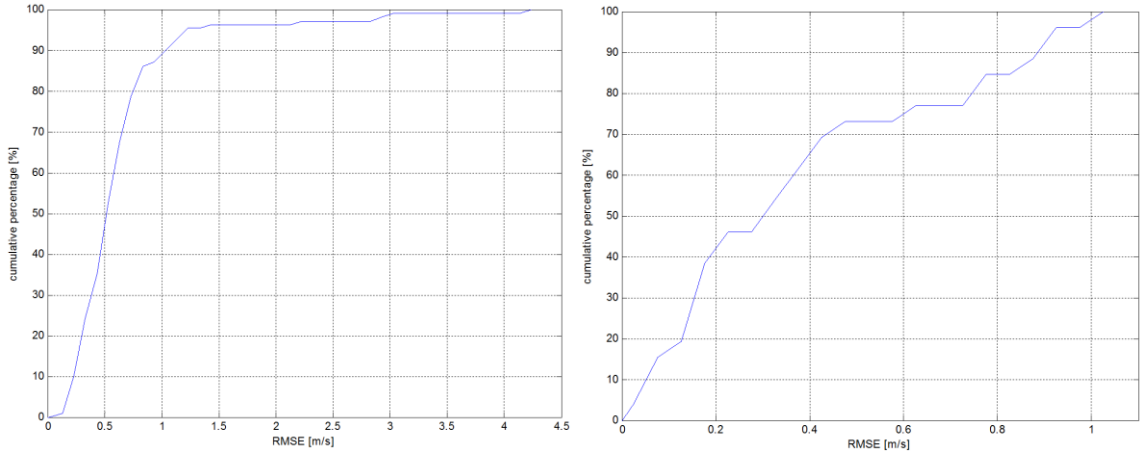

(a) **(b)**

Figure 5.12 Root mean square error in speed: (a) straight braking to rest and (b) free left turns.

5.5 Monte Carlo Simulations Including Lateral Control

As mentioned in the introduction, a key motivation in model development is for the test and development of future intersection safety systems, where human decision and control, as well as event timing, are critical. Data relevant to decision making behavior has been obtained in previous studies, particularly in terms of metrics of gap acceptance between the SV and POV via conflict metrics such as the time to collision (TTC) [69], gap time (GT) [7, 8] and leading and trailing buffers (LB/TB) [5, 9, 10]. In the future, such data may be used to perform system identification on decision making sub-models.

Here we limit attention to control aspects, and perform batch simulations for cases where the decision to complete the left turn is assumed to have been made. Monte Carlo simulation is applied by uniform sampling from the parameter ranges obtained from the analysis in Section 5.4.4. Parameter ranges are shown in Table 5.3, where the "population" values are used for Monte Carlo simulation; these are unbiased estimates of population limits, having a slightly wider range than the sample values [70].

Table 5.3 Ranges of driver parameters for Monte Carlo Simulation.

Parameter	Sample Minimum	Sample Maximum	Population Minimum	Population Maximum
ub_1 [m/s^2]	2.03	3.53	1.97	3.59
ub_2 [m/s^2]	2.6	5.1	2.50	5.20
a_1 [m/s^2]	−3.98	−1.83	−4.07	−1.74
a_2 [m/s^2]	−0.89	−0.06	−0.92	−0.03
a_3 [m/s^2]	0.4	2.98	0.30	3.08

To improve model validity, we adopt the commercial vehicle dynamics simulation software CarSim® (Version 8) to replace the simple vehicle model of Section 5.2. This has the advantage that realistic friction limits and vehicle responses are obtained. On the other hand, we must now introduce a lateral control model to conduct Monte Carlo simulations. This is implemented as a simple path-following steering model, using a predetermined intended path. The path is prescribed by joining two straight segments with a circular arc as shown in Figure 5.13.

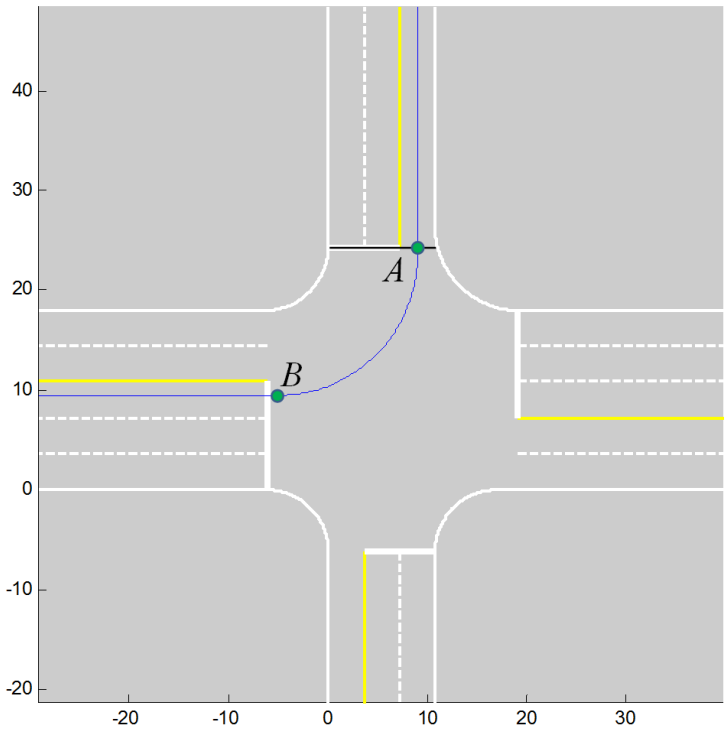

Figure 5.13 Intended left turn path using constructed from two lines and one arc segment.

The steering control model is of the *preview tracking* type [43] formulated for simplicity and applicability to large angles of turn. It has two levels, similar to the speed control model, where the upper level defines a desired yaw velocity, r_{des}, and the lower level is designed to track that reference. Reference yaw velocity is firstly determined by the requirement to track a target point on the intended path. For an assumed constant radius arc and preview distance *d* (see again Figure 5.2) the desired yaw rate is determined by visual preview

$$r_{des} = r_{\Delta\psi} = \frac{2U\sin(\Delta\psi/2)}{d} \tag{5.8}$$

This is equivalent to $\hat{a}_y$ in equation (5.1), with the factor *U* converting between yaw rate and lateral acceleration (assuming vehicle sideslip angles are small). In addition to this feed-forward (preview) reference, path corrections may be required, as determined by the local yaw angle error $\tilde{\Delta}\psi = \psi - \psi_P$, where ψ_P is the instantaneous vehicle yaw angle and ψ is the geometric yaw angle of the circular arc shown in Figure 5.14. This requires the addition of a feedback term:

$$r_{des} = r_{\Delta\psi} + K_r \frac{U\tilde{\Delta}\psi}{d} \tag{5.9}$$

written so the feedback term has a dimensionless gain K_r.

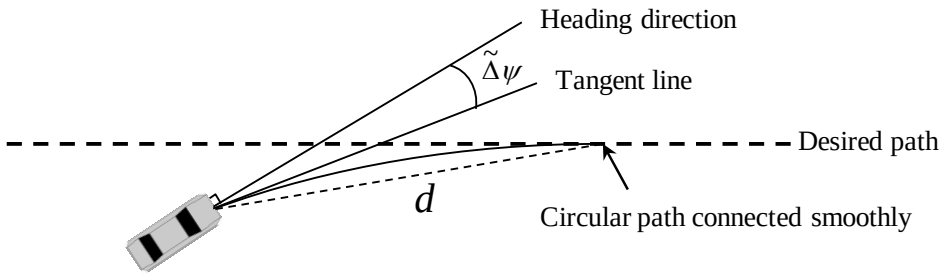

Figure 5.14 Heading error for additional yaw rate requirement.

At the lower level, steering rate u_y (angular velocity of the steering wheel) is found by proportional control of the error in yaw rate:

$$u_y = K_y e^{-\infty}\left(r_{des} - r\right) \tag{5.10}$$

where again the feedback gain, K_y, is dimensionless.

The feedback gains, K_r and K_r as well as the preview time, T_p, are tuned in Appendix E. For T_P, the corresponding preview point is located on the intended left turn path and different from the gaze points, Q_x and Q_y.

The above model was applied to an intersection with 90˚ turns, as shown in Figure 5.15. To induce more realistic lateral variability in the path, the location of *A* was selected randomly within a 5 m sample domain that includes the position shown in Figure 5.13. In the figure, point *A* varied between 3.33 m to the North (further from the intersection) and 2.67 m to the South; then point *B* is uniquely defined to smoothly connect the first segment and the arc at point *B*.

One thousand left turn events were simulated, and for illustration Figure 5.15 shows a sample of 100 results in the form of spatial trajectories and speed curves; corresponding results from measured driving data are show in Figure 5.16. Here only six events were found at the single specific location modeled. Both the spatial trajectories and speed curves are seen to be broadly similar. In particular, the speed curves are similar in two important characteristics: (a) the wide dispersion in speed during the approach stage converges to a narrower range near the minimum speed; (b) the locations of the minimum speed are consistent between the simulations and data, i.e. they occurred slightly after the stop bar of the entry leg (located here at $s = 0$ m).

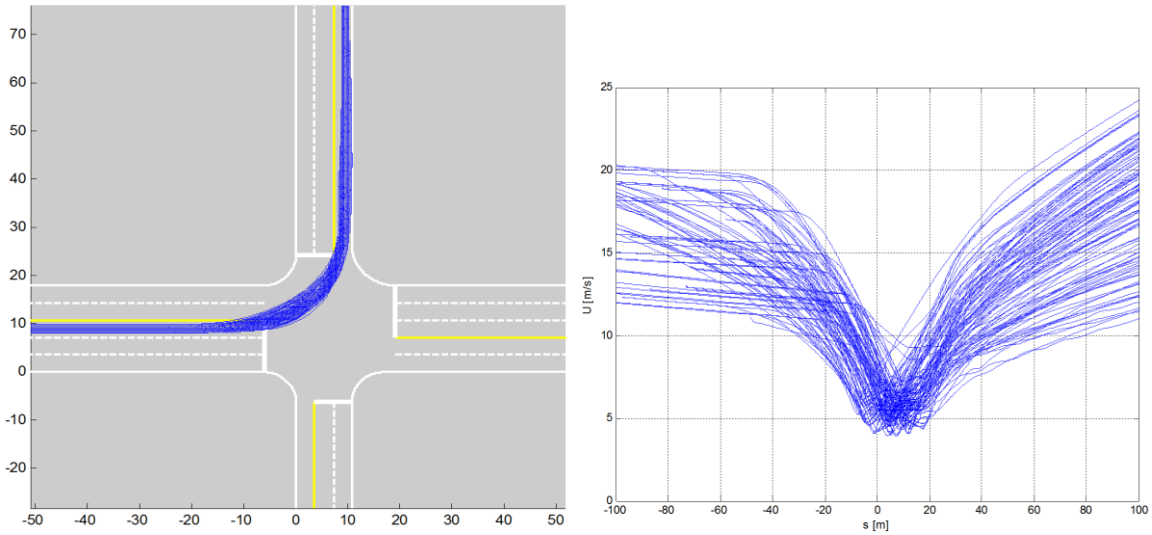

Figure 5.15 Free left turn trajectories and speed curves from Monte Carlo simulations.

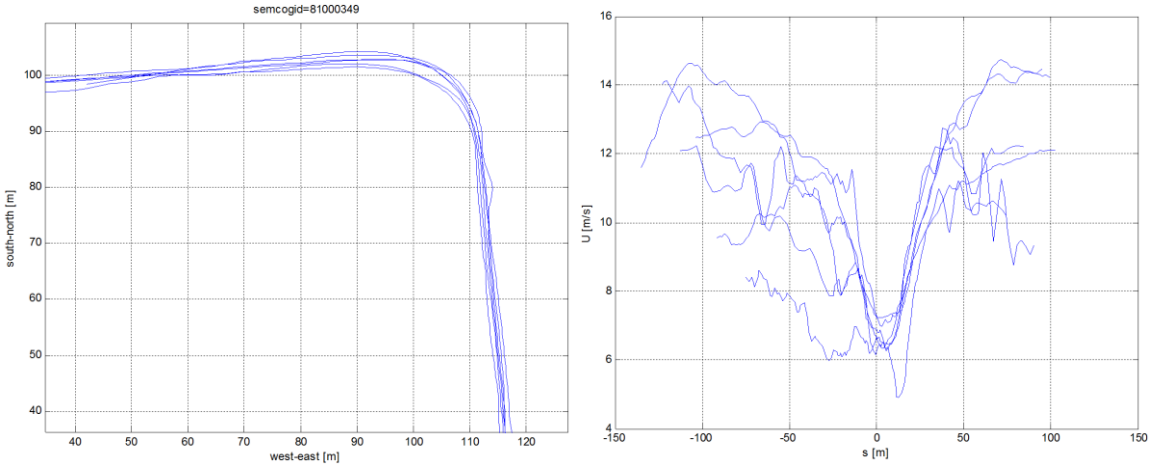

Figure 5.16 Free left turn trajectories and speed curves from driving data.

Now we make comparison with a larger number of turning events in the data; 46 events were found, using 22 different intersections considered broadly similar to the geometry used in above simulation. This was based on the criteria that the turn angle was within the range 90˚±20˚; from video review, traffic interactions were also required to be minimal. Detailed digitization of the intersection geometry was not required since only speed distributions are to be compared. The initial position and speed for the simulations were randomly sampled from a list of pairs of those measured in the actual events. These initial conditions were taken at the instant 10 m before braking occurs in order to avoid

including erratic speed variations before the intersection approach dominates speed choice. Since different intersections were used, and the stop bar location was not always known, the distance variable was set so the datum ($s = 0$ m) occurs at the point of minimum speed. This was used to co-locate all events, simulated and measured.

Figure 5.17 shows a comparison between the 1000 simulation results and actual events. In each case mean values and "error" bars ($\pm \sigma$) are shown. As mentioned, only six of these events occurred at the intersection used in the simulation, so some variation between measurement and simulation is expected. The overlap is best during the approach stage, which is the most critical stage for this study; the deceleration rate is similar to measurement and speed variability is also of a very similar magnitude. This indicates that parameter value ranges were satisfactory. The simulation model has a lower minimum speed within the intersection, and a higher acceleration during the exit stage. The lateral control model used a very simple desired path, and also the variations in intersection geometry are likely responsible for the minimum speed differences; and, as mentioned above, the exit phase was not modeled in detail, being determined by a single reference acceleration and using the same control gain as for braking, which is likely too simple. Overall, the match appears satisfactory, given that the model is being used to idealize highly variable human driving behavior.

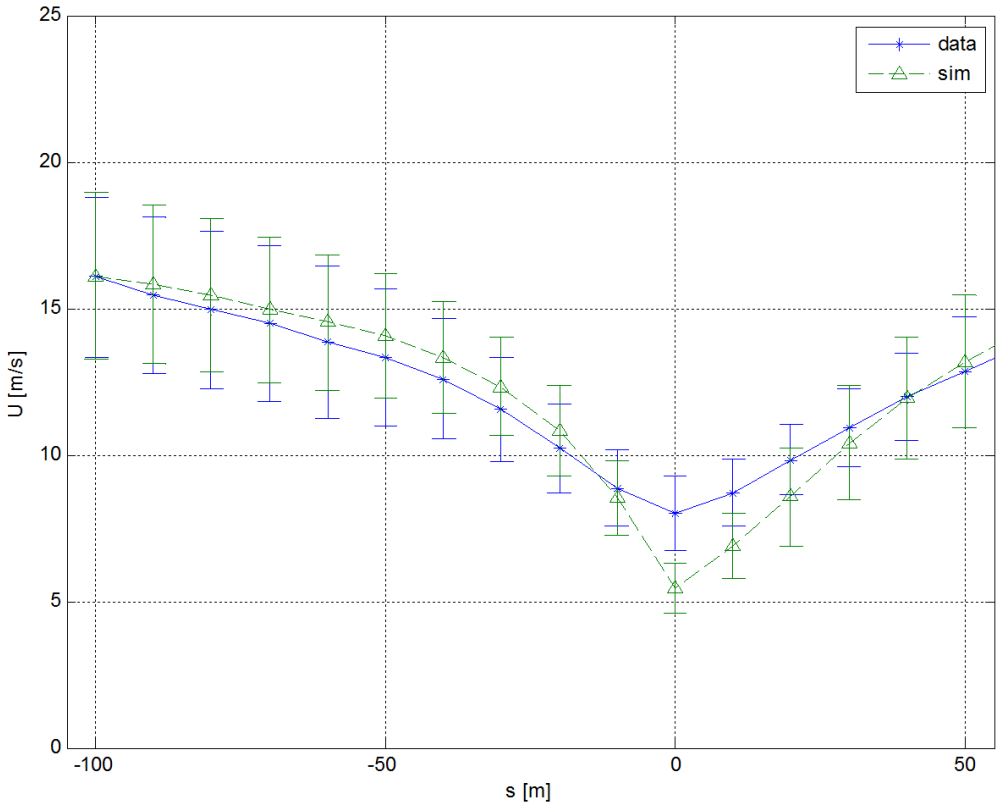

Figure 5.17 Comparison of speed between data and simulation results.

5.6 Discussion

This chapter has presented a speed control model based on an anticipated acceleration $\hat{a}$ and confirms its consistency with speed and longitudinal acceleration time histories seen in naturalistic driving data. Initial analysis showed that drivers do regulate AAR within tight limits during intersection approaches, so it is a plausible variable to apply as a control reference in modeling and simulation. Closed-loop simulations were performed for two types of model, one including only the longitudinal control only and the other including lateral control and a high fidelity dynamic model of the vehicle. The first model was used for parameter estimation of the AAR model, and for initial validation for individual cases of straight-line braking and free left turn events; the full simulation model extended the validation and demonstrated the use of Monte Carlo simulations to create a population of virtual left turns at a given intersection. The Monte Carlo approach can be used as a tool for investigating intersection safety, and evaluating intersection safety systems where the driver may stop or complete the turn. Decision making and

initiating a turn from rest were not included in the model, but there is scope to expand the model in the future.

Regarding the decision point to make a free left turn, Figure 5.18 shows the distribution of the crossover point between $\hat{a}_x$ and $\hat{a}_y$ with the stop bar location as its datum, which is assumed to be a switching point of the driving mode from the approach stage to turn stage. The crossover point will not occur until the SV reaches close to the intersection, which is likely to make it difficult to predict whether a driver is actually intending to make the turn or come to rest. For the present model we can assume that the decision is not fully made until the crossover point. This is substantiated by other research [48] where it was attempted to capture the intention to make a left turn by monitoring the motions of various body parts. Their result shows that while the rate of true positive is about 75 % at around 0.5 s before the left turns were started, the rate of true positive drops rapidly when making a prediction point earlier – it becomes 30 % (with the same false positive rate) if the prediction is made at 1.5 s before the turn. Therefore, from these results, it might be implied that human drivers does not show a clear evidence of the left turn decision until they reach sufficiently close to the intersection, consistent with the present model formulation that options to turn or stop remain open during the approach. In addition, the positive values in the distribution may be related to the intersection geometry as well as the driver variations, e.g. the relative locations between the stop bar and the shape and size of the intersection.

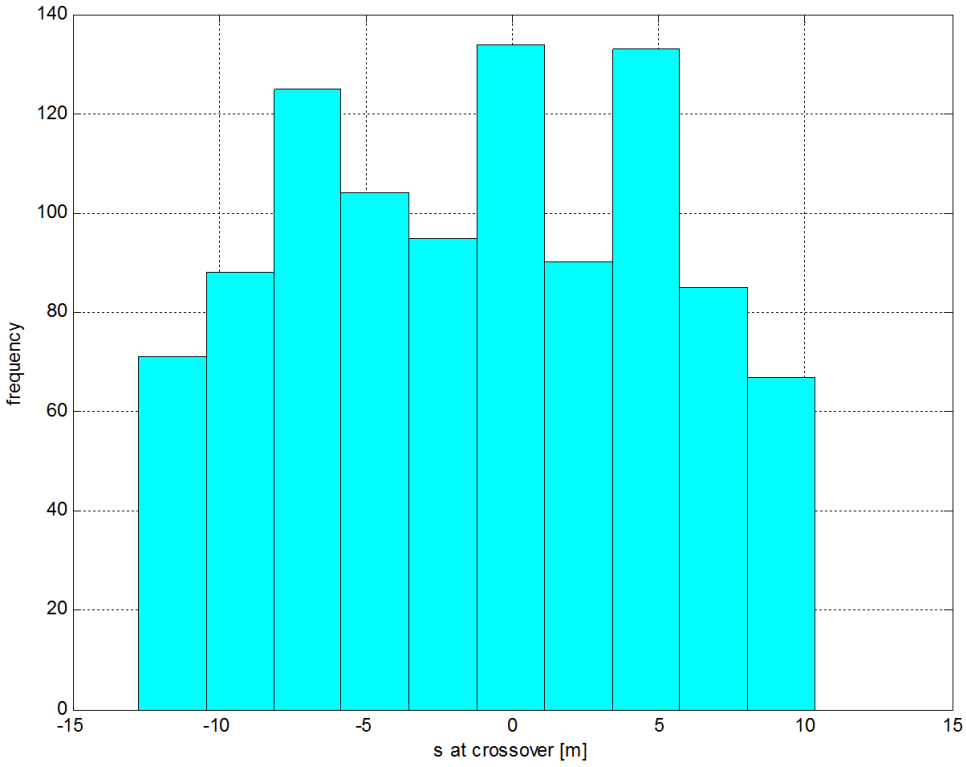

Figure 5.18 Distribution of the crossover point between $\hat{a}_x$ and $\hat{a}_y$.

Aside from the intersection safety focus of this dissertation, speed control based on AAR may be directly applicable to modeling the regulation of speed in curves. A key difference from intersection left turns is the definition of gaze point; for intersection left turns use was made of the stop bar locations for the entry and exit lanes for $\hat{a}_x$ and $\hat{a}_y$ respectively. For speed control in curves is it more appropriate to use a single gaze point using the line of the "apex", the line from the drivers eye to a tangent point on the inner curve boundary [71]. Figure 5.20 shows a complex turn where a slight curve (*P*) precedes a sharp turn. The blue solid curves are the lane boundaries and the red dashed curve is the measured vehicle trajectory. In contrast to speed control on an intersection approach, here $\hat{a}_y$ is dominant in the beginning period until a crossover occurs at $s \approx 100$ m. At this point the driver brakes and for the remainder of the approach to the sharp curve $\hat{a}_x$ is dominant. Deceleration continues until $s \approx 280$ m where both $\hat{a}_x$ and $\hat{a}_y$ decrease rapidly, due to passing the apex of the turn and the gaze point recedes from the driver; it follows that speed is no longer constrained by $\hat{a}$ and the driver accelerates.

This example suggests how the speed control model, based on anticipated acceleration derived from road geometry, can be applied more widely in the future.

Moreover, the reciprocal relationship between the lateral acceleration and vehicle speed is an interesting characteristic in general curve driving situations; in steady-state turns with various degrees of road curvature, the lateral acceleration decreases monotonically as the vehicle speed increases [32, 72-76]. A possible reason for this might be the driver's risk taking behavior; the influence of errors in the estimated road curvature is intensified as the vehicle speed increases and it decreases the available safety margin [32].

It is noted that this reciprocal relationship is not observed in left turn cases. Instead, the drivers achieved the same a_y regardless of U as can be seen in Figure 5.19 which shows a distribution of maximum a_y vs. corresponding U for free left turn events. The maximum a_y was detected within the left turn period defined between the time when the steer angle magnitude became more than 0.02 rad for the first time and the time when it returned to 0.02 rad. The resulting maximum a_y ranges between approximately 3 and $5\,\mathrm{m/s^2}$ with an average at about $4\,\mathrm{m/s^2}$. There would be various reasons for this discrepancy from regular curve driving, e.g. a lack of pre-defined road boundaries, lack of a clear steady-state period due to a short period of time required to complete a left turn, and low vehicle speed. This study will not investigate on this further, but it is interesting for a future study.

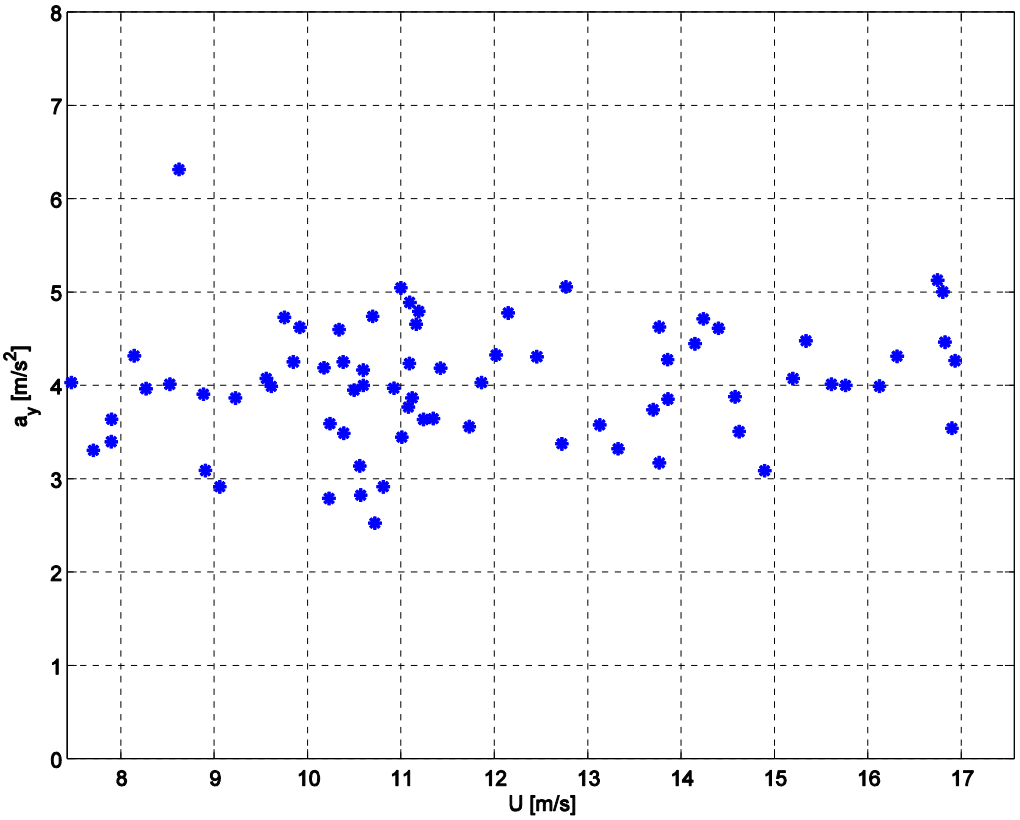

Figure 5.19 Distributions of maximum lateral acceleration vs. corresponding vehicle speed during left turns.

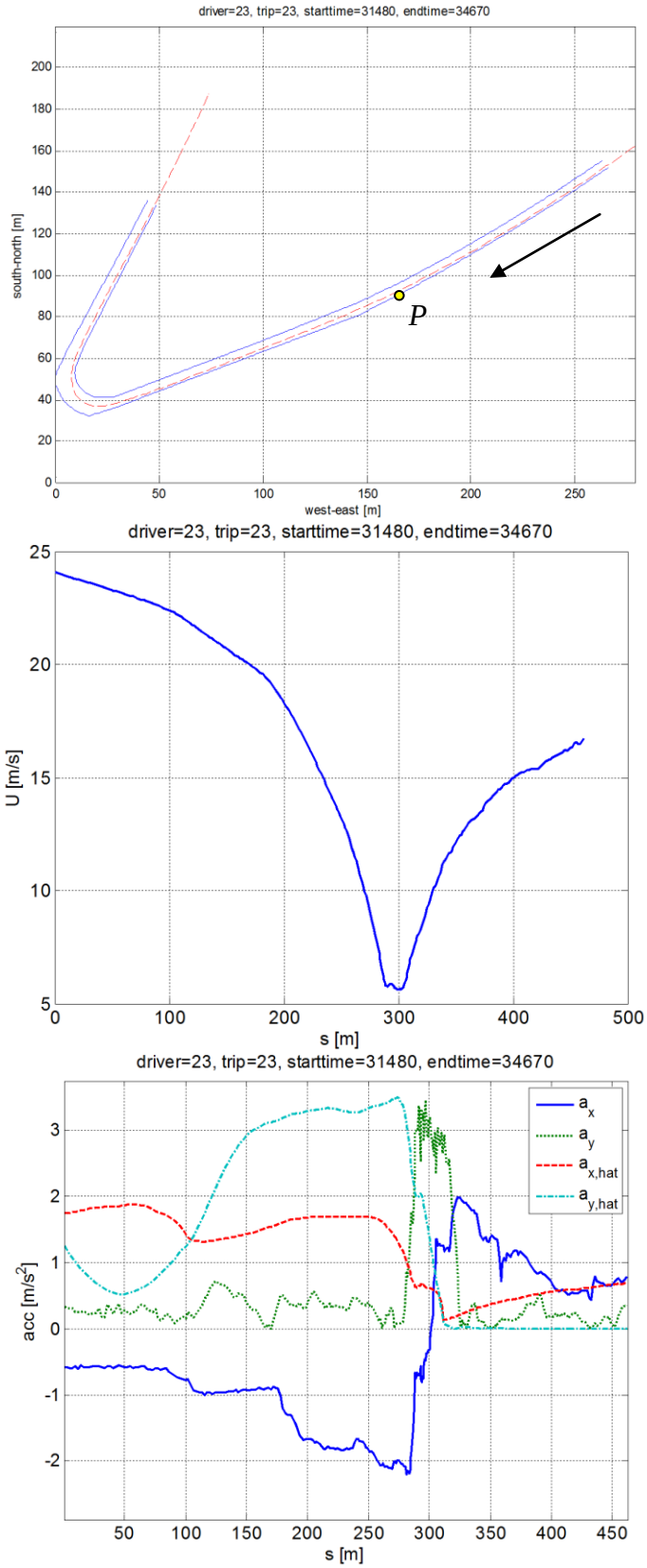

Figure 5.20 Driving on a sharp curve with a prior slight curve.

Chapter 6
Driver Assistance System for Intersection Left Turns

6.1 Overview

The main objective in this chapter is to investigate the viability of the proposed design framework for free left turn based on a candidate assistance system. Each LTAP/OD event with a free turn SV represents the scenario in which the SV driver fails to detect an oncoming POV ("looked but did not see") since the driver is assumed to make a left turn regardless of the available gap with the POV. Therefore, the driver's decision process is ignored. Nevertheless, the structure of the proposed framework can be applied to other left turn scenarios, e.g. misjudgment of available gap, once the LB/TB can be calculated appropriately taking into account the driver's decision process.

The design framework consists of event sampling to create a large set of LTAP/OD events in which POVs are superimposed over the free left turn events obtained from the Monte Carlo simulations. Then LB/TB calculations are made for each LTAP/OD event to estimate the safety type of the LTAP/OD event, and whether an alert should be given. Then the warning system parameters are to be optimized in a Pareto optimal sense. Analyses of the SV driver's reaction time before braking are to be included in the analysis.

The analysis will focus on the functional performance and parameter tuning, rather than detailed hardware and interface design; aspects of system architecture including selection of mechanical and electrical components, human machine interface (e.g. visual, auditory and haptic) which would affect the attention level and reaction time of the driver are not considered [53, 77, 78].

In the following, Section 6.2 gives a description of the assistance system proposed, while procedures of event preparation and preliminary analyses necessary for the design process are provided in Sections 6.3 - 6.4; Section 6.5 presents an optimization procedure to select values for system parameters and Section 6.8 shows results.

6.2 Left Turn Assistance System

The assistance system is assumed to give a warning when a potential conflict is detected using the LB/TB at a specific vehicle location. The system parameters to be optimized are: two thresholds, Δ_{TB} and Δ_{LB} (see expression (4.10)) and the distance D_w between the SV position and stop bar from which LB/TB is calculated. These parameters affect the system performance in different ways – Δ_{LB} and Δ_{TB} determine P(TP) and P(FP) with the probability density distribution unchanged, while D_w shifts the locations of the distributions, i.e. the degree of overlapping between these distributions varies. For example, as D_w approaches 0 (i.e. the stop bar), the LB/TB results are expected to become more accurate (less overlapping), and as a result, the trade-off between TP and FP can be mitigated. However, if a warning is given too late, there may not be an enough distance for the SV to stop safely and the assistance system becomes meaningless. Therefore, the warning location is also included in the system parameters. Let us define successful braking (SB) as a case in which there is a sufficient distance to reach rest without going beyond the stop bar, and unsuccessful braking (UB) as a case in which the vehicle exceeds the stop bar during braking. Then the rate of successful braking under the condition of TP, P(SB|TP), increases as the warning timing is delayed, but at the expense of increasing the rate of unsuccessful braking, P(UB|TP).

A challenge in the left turn assistance system is that it cannot directly determine the driver's decision state while the SV is still sufficiently far from the intersection, i.e. whether or not the driver is going to continue braking to stop or proceed to turn left, since the SV always decelerates at this point in normal left turns. Specifically, if the driver intends to stop, a warning signal is unnecessary and may be recognized as an FP. Although resolving this issue is clearly important to reduce the annoyance of the driver,

this is beyond the scope of this simulation analysis, in which the driver is always assumed to be going to make a left turn.

6.3 Principal Other Vehicle Driver Behavior

As mentioned, it is assumed that the SV driver is unaware of the oncoming POV and the driver's decision process is ignored. Similarly, the POV is also assumed to be unaware of the SV and the POV does not make an evasive maneuver at any level of conflict with the SV. Although an appropriate POV intervention (e.g. honking, flashing headlights, braking, etc) may reduce the conflict level, the safety system design is made excluding the decision making of the drivers for simplicity. Moreover, it is unlikely that the POV driver takes a maneuver which increases risk. Therefore, the nominal condition of POV driver maintains constant speed is the natural assumption in the design condition.

6.4 Brake Reaction Time and Stopping Distance of the Subject Vehicle

The minimum distance that the SV driver needs to stop before the stop bar is defined by the sum of the distance traveled from when a warning signal is issued to when the brake pedal is depressed and the distance traveled during the following brake application period until the SV reaches rest.

In [79], a comprehensive review of existing literature revealed that the reaction time varies greatly depending on the driver's expectation that a specific event will occur as well as stimulus type, response maneuver, and experimental conditions. Obtained experimental distributions are often skewed and the distribution of the brake reaction time is approximated more appropriately by a lognormal distribution than by a normal distribution [80-82]. Previous studies considered not only the reaction time itself but also the movement time. In such studies the reaction time is defined as the time which the driver takes to release the accelerator pedal after a warning is given; then the movement time is the time taken to move the right foot to the brake pedal to decelerate once the accelerator is released. These results are not directly applicable to free left turns. A free left turn naturally involves braking to achieve the desired speed for the turn stage and the

brake pedal is likely to be depressed when a warning is given to the driver. Therefore, the movement time is not included here. In this study, the reaction time distribution is adopted from a simulator study for lane change scenarios [83], in which the drivers of the lane changing vehicles (the SVs) were told to abort lane change when a warning notified them that the vehicle was approaching the SV in the target lane. The subjects used steering control to avoid colliding with the vehicle following the SV at the rate of 99.1 % of all the lane abort responses. Although the similarity between the steering response in the lane change scenarios and the brake response in the LTAP/OD scenarios is vague, these responses are natural consequences in the driving scenarios, that is, steering control is more dominant than brake control in the lane change cases, while brake control is more prevalent than steering control in the LTAP/OD. Therefore, it is assumed that the movement time is sufficiently small and ignorable. A potential drawback of using the steering response result for the brake reaction time is that the difference between the arm motion and leg motion may cause significant influence on the reaction time. The reaction time distribution for the lane change abort by the lognormal assumption is shown in Figure 6.1.

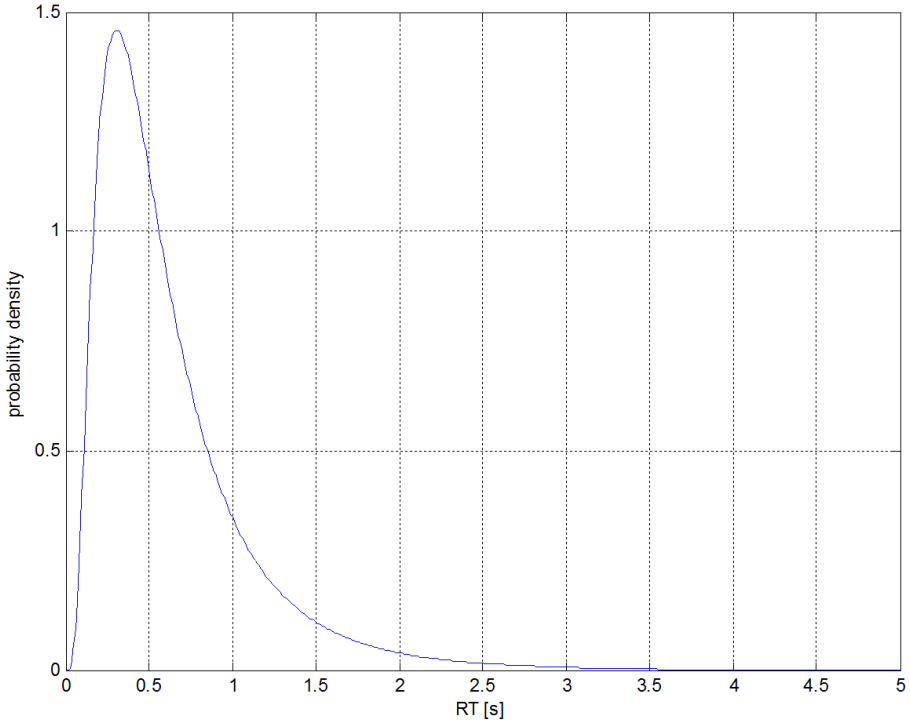

Figure 6.1 Reaction time by a lognormal distribution.

The stopping distance was computed using the braking control of the SV which was estimated from hard braking events found in the field operational test database of a previous project for the Automotive Collision Avoidance Systems (ACAS) [84]. A total of 88 such events were used in the analysis; for each of the deceleration profiles a first order response was fitted. This was identified by three parameters, amplitude A, time delay offset t_d and rise time t_r. Each parameter was assumed to follow a lognormal distribution. Details about developing the parameter distributions are available in Appendix F. Using the distributions of the braking parameters, simulations were run on MATLAB Simulink® with a CarSim® vehicle model for the speed range, [3, 40] m/s, with 1 m/s of intervals (i.e. 38 speeds in total). For each speed, 100 braking simulations were run for different model parameter values. Resulting distance traveled to reach rest was saved in a 38-by-100 array so that a stopping distance can be selected randomly from a row corresponding to the closest speed to the vehicle speed at the brake initiation.

6.5 Event Sampling

Each LTAP/OD event was created by pairing a free left turn event sampled from the batch simulation results prepared in Section 5.5 and a POV for which the initial position and speed were selected randomly. The POV speed was sampled from a normal distribution fitted to the distribution of the speed limit at crash sites found in the General Estimates System (GES) (Figure 6.2). Since a normal distribution is not bounded, certain limits needed to be imposed: if the sampled speed was slower than 15 mph (≈ 6.7 m/s) or faster than 65 mph (≈ 29.1 m/s), it was rejected and re-sampled. The GES data was queried with the following conditions: 1) left turn vehicle drivers coded "looked but did not see", 2) no violations by other vehicles and 3) events not in interchange area. It is noted that a potential discrepancy between the actual POV speed and speed limit in the crash event was not considered since vehicle trajectory data is not available in the GES, so they are assumed to be the same instead. The initial POV position p_0 was selected in a range $[p_{c1}, p_{c2}]$ where $p_{c1}$and p_{c2} corresponded to the PET threshold Δ_{PET} which was estimated in Section 4.3.1, i.e. −1 s in the case when the SV crosses second and 2 s in the case when the SV crosses first to distinguish safe and unsafe events. The PET range of interest for the event sampling was made by adding a time margin δ_{PET} to Δ_{PET} for each

case, i.e. $[\Delta_{\text{PET}} - \delta_{\text{PET}}, \Delta_{\text{PET}} + \delta_{\text{PET}}]$. Table 6.1 summarizes selected values for these parameters. The lower bound of the range where $p_0 = p_{c1}$ became $\text{PET} = -1 - 3 = -4\,\text{s}$ and the upper bound where $p_0 = p_{c1}$ became $\text{PET} = 2 + 3 = 5\,\text{s}$. Each of the created events was labeled as either a safe, near-miss or crash event depending on the PET value as shown in the conceptual schematic in Figure 6.3. In order to create each LTAP/OD event, a free turn event and the initial conditions for the POV were sampled separately until the PET of the obtained event became within the target range. Otherwise, the candidate LTAP/OD was discarded and another pair of free turn event and POV were sampled including the speed sampling for the POV. This process was continued until 1000 LTAP/OD events were created. Figure 6.4 shows a histogram of the PET of the LTAP/OD events, which is seen to be approximately uniformly distributed.

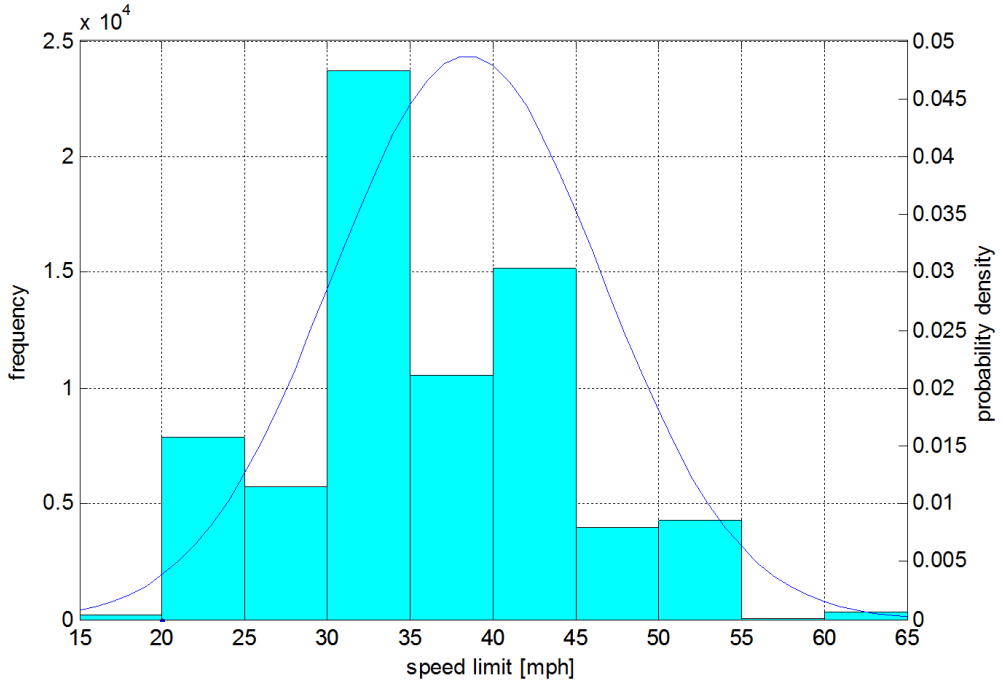

Figure 6.2 Distribution of speed limit from GES crash events and normal distribution fit.

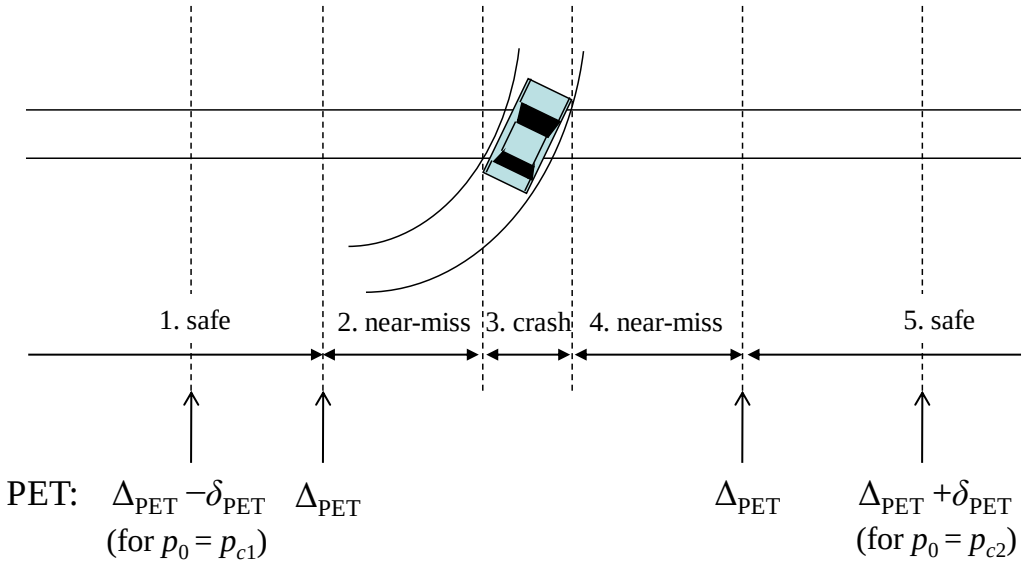

Figure 6.3 Schematic of the relationship between the range of the post encroachment time and the position the through vehicle when the left turn vehicle is at a conflict point.

Table 6.1 Values for Δ_{PET} and δ_{PET}.

	SV crossing second	SV crossing first
Δ_{PET} [s]	−1	2
δ_{PET} [s]	3	3
PET [s] at bounds	−4	5

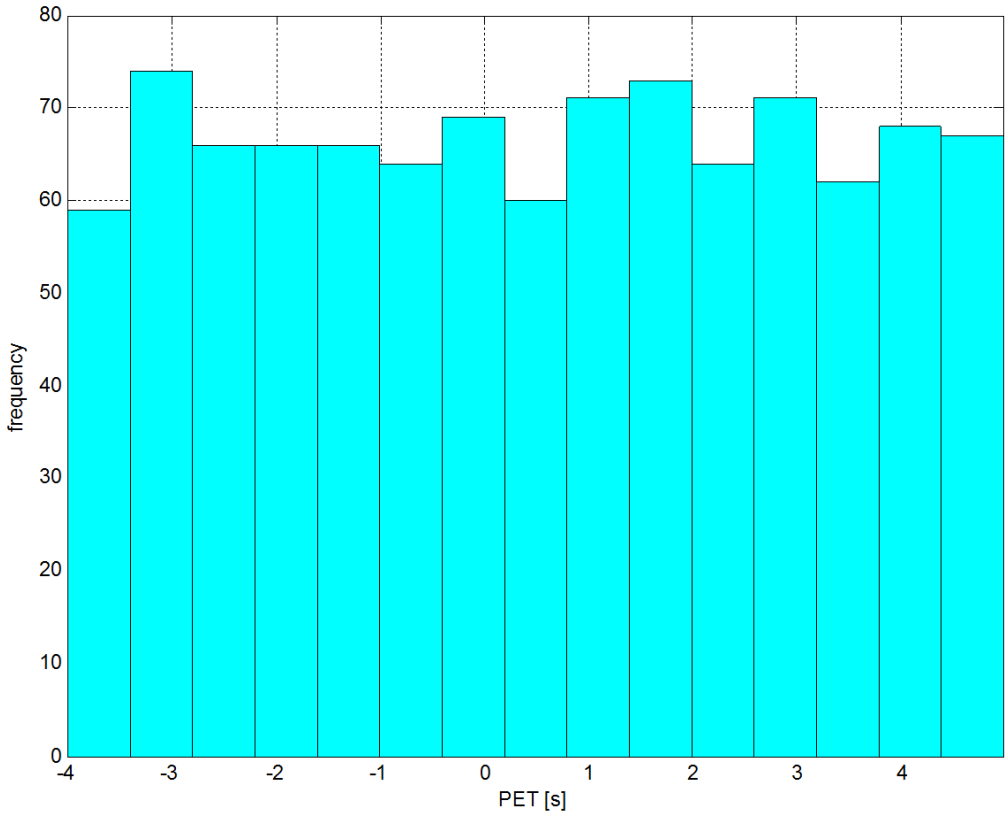

Figure 6.4 Distribution of the post encroachment time of the virtual LTAP/OD events.

6.6 Calculation of Conflict Metrics and Estimation of Event Safety

The LB/TB was calculated for the LTAP/OD events prepared in Section 6.5. The method of LB/TB calculation was as described in Section 4.2 except for the U_{ref} construction. Here, U_{ref} was made by averaging speed curves of all the simulated events at each vehicle position, since the simulations were run at the same intersection and the number of events was sufficiently large to obtain a smooth curve. Figure 6.5 and Figure 6.6 shows typical results of the LB/TB analysis. By assuming that Δ_{TB} and Δ_{LB} coincide with Δ_{PET} corresponding to the respective crossing type of the SV (i.e. $\Delta_{TB} = -1\text{s}$ and $\Delta_{LB} = 2\,\text{s}$), Figure 6.5 shows a buffer band made for an unsafe event which is a near-miss case with the SV crossing first as indicated by the PET specified by the triangle located between the horizontal lines at 0 and 2 s of the vertical coordinates. The buffer band correctly estimates the event as a near-miss case for the entire event, so a true-positive is expected at any instant. Figure 6.6 shows a false positive result for a safe event, since the buffer

band crosses the horizontal line at Δ_{LB} (= −1 s) predicting a near-miss case at any instant. The PET of this event is −1.8 s as shown in the figure in the case of the SV crossing second. The flat buffer bands in these examples indicate that U_{pred} predicts future speed very well in the free left turn cases in which there are not large deviations between the actual speed and U_{ref}. In addition, the accuracy of a safety estimation result depends on the location of the estimation. Figure 6.7 shows a buffer band for a near-miss event with a transition of safety estimation from safe to unsafe at $s = -23\,\text{m}$ at which the buffer band crosses Δ_{TB} line.

For each LTAP/OD event, various values for Δ_{LB}, Δ_{TB} and D_w were tested using the obtained LB/TB result. The ranges of these parameters were: $\Delta_{LB} \in [-3, 0]\,\text{s}, \Delta_{TB} \in [1, 4]\,\text{s}$ and $D_w \in [0, 100]\,\text{m}$. Uniform sampling intervals were chosen: 0.1 s for Δ_{LB} and Δ_{TB} and 2.5 m for D_w. As a result, 39,401 combinations of test points were obtained. For each of these combinations, the one-thousand free turn events created by the Monte Carlo simulations were classified into true positive (TP), false positive (FP), true negative (TN), false negative (FN), successful braking (SB) or unsuccessful braking (UB) to count the numbers of occurrence of these cases. It is noted that SB and UB can occur only under a true positive condition, i.e. the probabilities of these become $P(\text{SB}|\text{TP})$ and $P(\text{UB}|\text{TP})$. Six arrays, each of which was three dimensional and initialized by zeros, were prepared for TP, FP, TN, FN, SB and UB cases. These arrays hold the frequencies of the cases for all combinations of the parameter values in the corresponding elements. For example, the first example shown in Figure 6.5 indicates a TP with $\Delta_{LB} = -1\text{s}$ and Δ_{TB}=2s at $D_w = 40\,\text{m}$ (or $s = -40\,\text{m}$), so the corresponding element in the TP array is incremented by +1. After completing the arrays, the following equations were used to compute the probabilities,

$$P(\text{TP}) = nTP/(nTP + nFN) \tag{6.1}$$

$$P(\text{FP}) = nFP/(nFP + nTN) \tag{6.2}$$

and

$$P(\mathrm{SB} \mid \mathrm{TP}) = nSB/(nSB + nUB) \tag{6.3}$$

where *nTP*, *nFN*, *nFP*, *nTN*, *nSB*, and *nUB* are the numbers of corresponding detection types. The estimated probabilities were saved in separate 3D arrays and these provide the objective space for the optimization process in the next section.

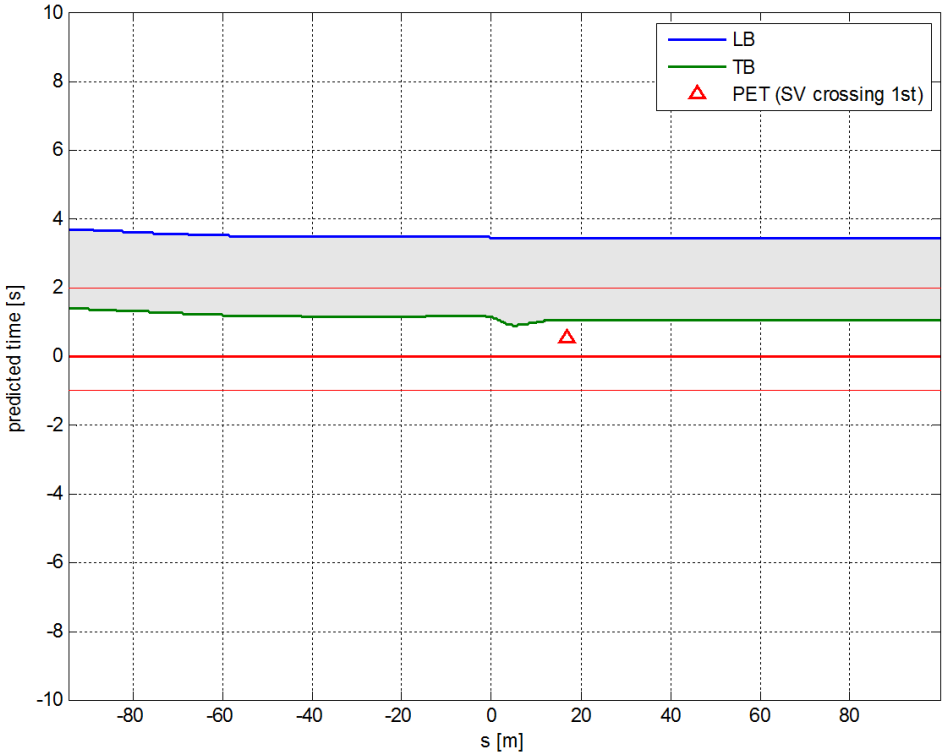

Figure 6.5 Unsafe event detected as unsafe (true positive).

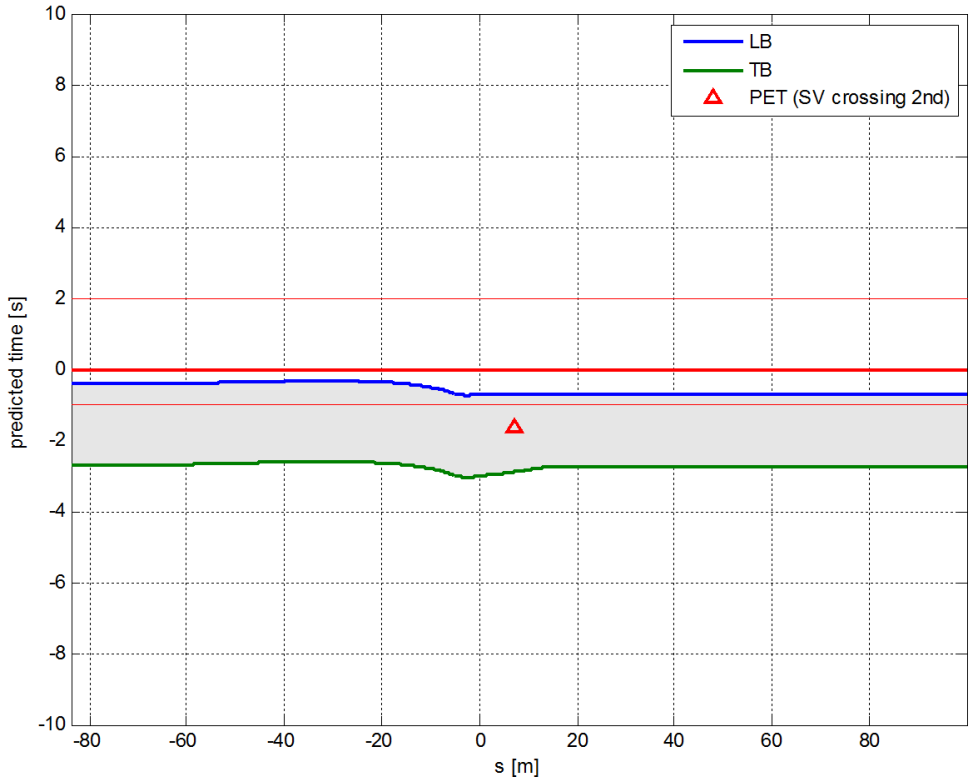

Figure 6.6 Safe event detected as unsafe (false alarm).

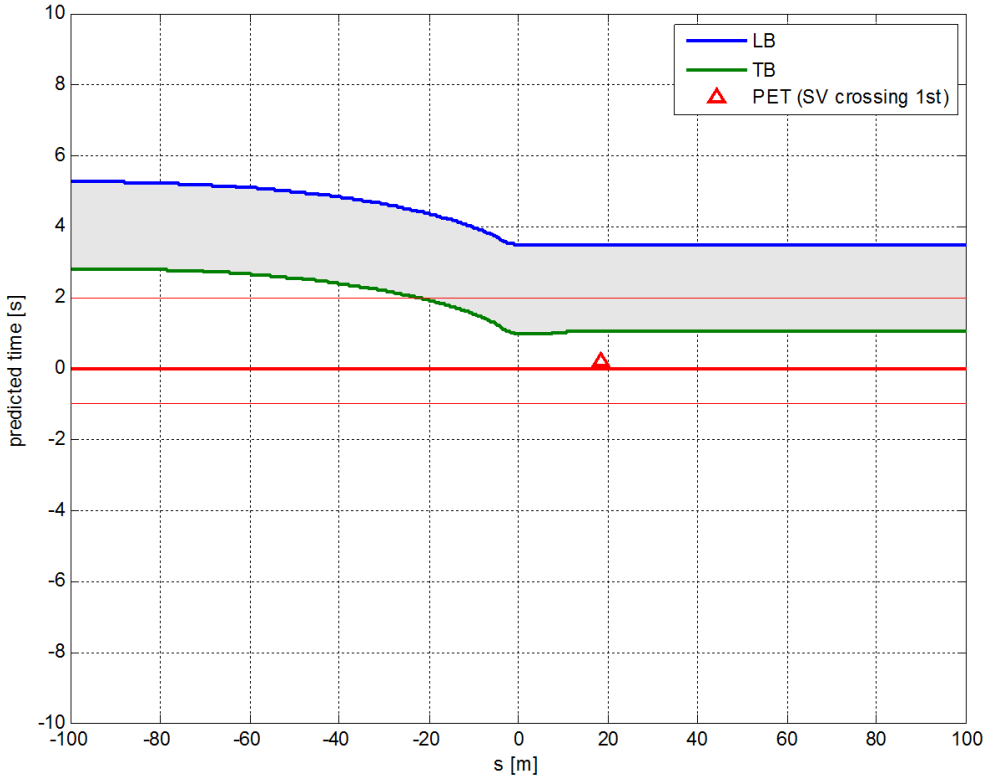

Figure 6.7 Unsafe event with variable safety estimation.

6.7 System Parameter Tuning by Pareto Optimality

In order to find optimal system parameter values, Δ_{TB^*}, Δ_{LB^*} and D_{w^*}, the following objective functions were considered: $f_1(\mathbf{x}) = -P(\mathrm{TP})$, $f_2(\mathbf{x}) = P(\mathrm{FP})$ and $f_3(\mathbf{x}) = -P(\mathrm{SB} \mid \mathrm{TP}))$ where $\mathbf{x} = [\Delta_{TB}, \Delta_{LB}, D_W]^T$ is the decision vector. The aim is to simultaneously minimize these functions, i.e. to maximize the probability of true positives, minimized false positives and maximize the probability of safe braking in the case of a true positive warning. Therefore, a multiobjective optimization problem was formulated. Figure 6.8 shows and event tree for the various event outcomes.

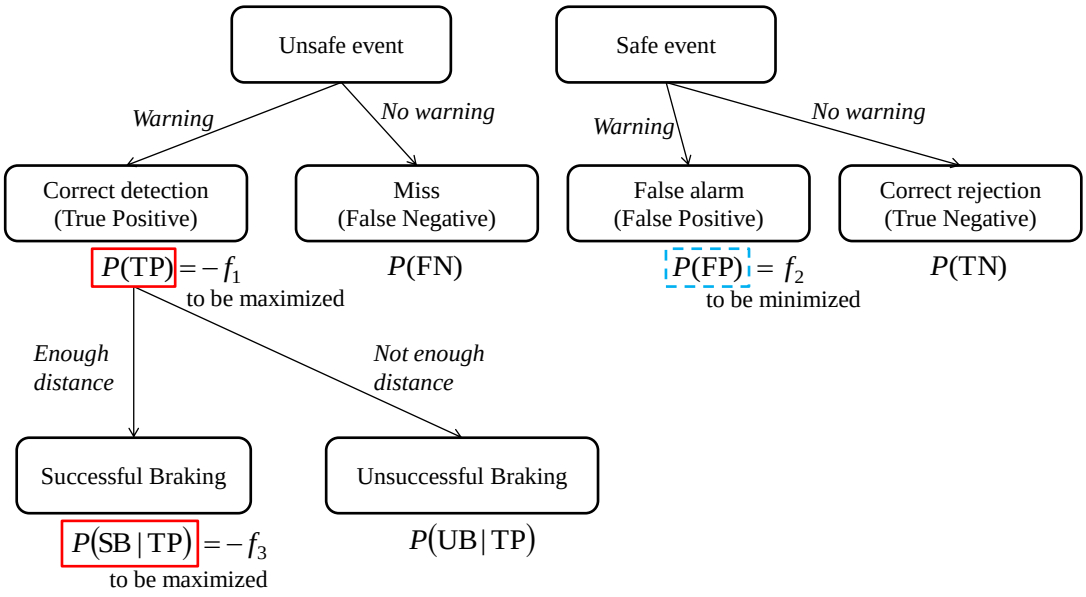

Figure 6.8 Tree diagram of probabilities for event safety estimation.

A general form of a multiobjective optimization problem can be written as

$$\begin{aligned} &\min_{\mathbf{x}} \ \mathbf{f}(\mathbf{x}) \\ &s.t.\ \mathbf{h}(\mathbf{x}) = \mathbf{0}, \\ &\quad \mathbf{g}(\mathbf{x}) < \mathbf{0} \end{aligned} \tag{6.4}$$

where **x** is a decision vector of design variables and **f**(**x**) is a vector of objective functions, f_i(**x**)'s, and **h**(**x**) and **g**(**x**) are constraint functions [85]. A multiobjective optimization

problem may involve trade-offs between objectives, because improving the performance of an objective may deteriorate the others [86]. Such a trade-off was shown in Figure 1.3. One way to solve a multiobjective problem is using the weighted sum method in which a scalar function, which is a linear combination of the objective functions,

$$\min_{\mathbf{x}} f(\mathbf{x}) = \sum_{i=1}^{n} w_i f_i(\mathbf{x}) \tag{6.5}$$

is used. However, selecting suitable values for the weighting factor w_i is not possible a priori [85-87]. Moreover, there would be infinitely many combinations of weights which give the same scalar number in equation (6.5) [87]. Therefore, the weights are often selected subjectively and the significance of the obtained design against the original design criteria may be obscure. On the other hand, the evolution strategy [86, 88, 89] uses the Pareto optimality to take into account the trade-offs directly. The Pareto optimal solutions comprise a set of all nondominated solutions. This set is called a Pareto set, in which any point is considered optimal in the Pareto optimal sense. In order to find Pareto optimal solutions, the concept of dominance plays a central role. A decision vector $\mathbf{x}$ is said to strictly dominate another decision vector $\mathbf{x}'$ if and only if

$$f_i(\mathbf{x}) \leq f_i(\mathbf{x}'), \forall i \quad \wedge \quad f_i(\mathbf{x}) < f_i(\mathbf{x}'), \exists i \tag{6.6}$$

and $\mathbf{x}$ is said to weakly dominate $\mathbf{x}'$ if and only if

$$f_i(\mathbf{x}) \leq f_i(\mathbf{x}'), \forall i. \tag{6.7}$$

These relationships are denoted $\mathbf{x} \prec \mathbf{x}'$ and $\mathbf{x} \preccurlyeq \mathbf{x}'$ in terms of the decision vectors, respectively. Then, the Pareto set S_P can be described by

$$S_P = \{\mathbf{x} : \forall \mathbf{x}' \not\prec \mathbf{x}, \mathbf{x} \neq \mathbf{x}'\}. \tag{6.8}$$

The evolution strategy employs a random search method by mutating a current decision vector in order to avoid an obtained solution from staying at a local minimum. A (μ+λ)-ES is a commonly used evolution strategy, which selects the decision vector to be tested by mutating μ parents to create λ offspring and the μ best individuals among μ+λ individuals will be the next generation's parents [88]. At each generation, a dominancy test is conducted to determine if there are any offspring to be included in the set of non-dominated decision vectors. The candidate decision vector was added to the non-dominant set which results in S_p if the negation of expression (6.6), i.e.

$$f_i(\mathbf{x}') > f_i(\mathbf{x}), \exists i \quad \vee \quad f_i(\mathbf{x}') \geq f_i(\mathbf{x}), \forall i, \tag{6.9}$$

is true. In this study, a single decision vector was evaluated at a time, so the procedure is similar to a (1+1)-ES in [86, 89]. However, since the saved objective vectors (Section 6.6) could be mapped to the corresponding decision vectors easily and the number of members in the objective space is not significantly large (39,401 members), all decision vectors can be tested easily. Therefore, the random search part to find a candidate decision vector at each iteration (generation) as in the full structure of the evolution strategy was omitted.

6.8 Results and Discussion

Figure 6.9 shows the Pareto front, which is a subset of the objective space associated with the Pareto set, and the selected operating point is shown by the red circle. The following steps were taken to select this operating point. First, $P(\mathrm{SB} \mid \mathrm{TP})$ was required to achieve 0.8, meaning that 80 % of braking attempts by responding to warning signals were successful braking to rest. (It is noted that 2 % of tolerance was allowed for each of the sides above and below 80 % in selecting such data points.) This created a "slice" of the Pareto front surface and a target ROC curve was obtained as shown by the red dots in Figure 6.9 and Figure 6.10. Then, the operating point was selected at 0.2 for $P(\mathrm{TP})$, and $P(\mathrm{FP})$ of approximately 0.89 was expected. Of course, the selection of the operating point is somewhat arbitrary and may vary depending on designers with different

requirements for the system. The corresponding decision vector is $[\Delta_{TB^*}, \Delta_{LB^*}, D_{w^*}] = [2.3\text{s}, -1.2\text{s}, 52.5\text{m}]$. Δ_{TB^*} and Δ_{LB^*} have the offsets of 0.3s and -0.2s from the nominal values, $\Delta_{PET} = 2$ and -1 s, respectively. This means that these are conservative selections of the detection levels since both are in the outside of the unsafe region defined between the Δ_{PET} values.

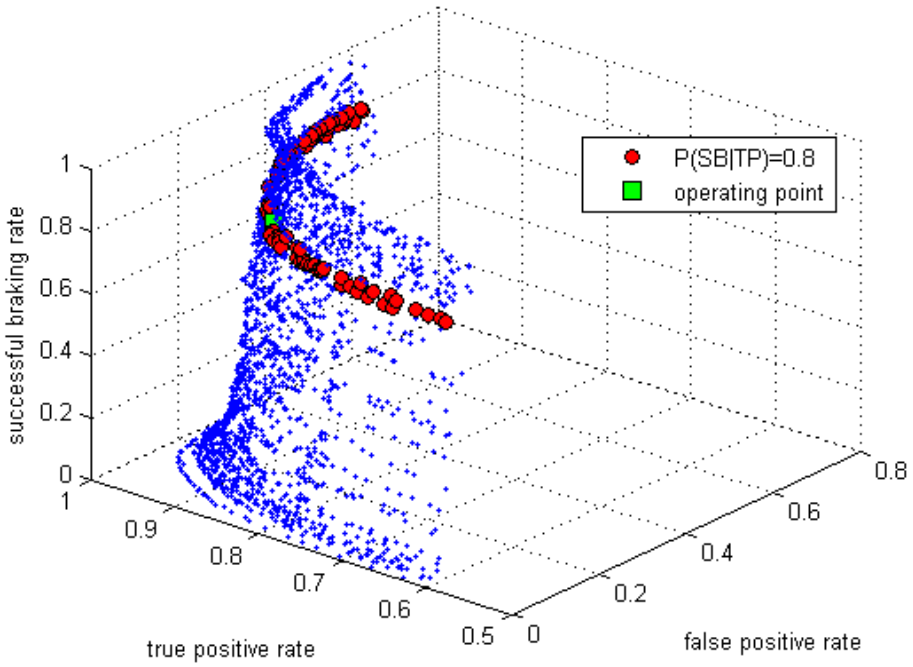

Figure 6.9 Pareto front from the perspective view.

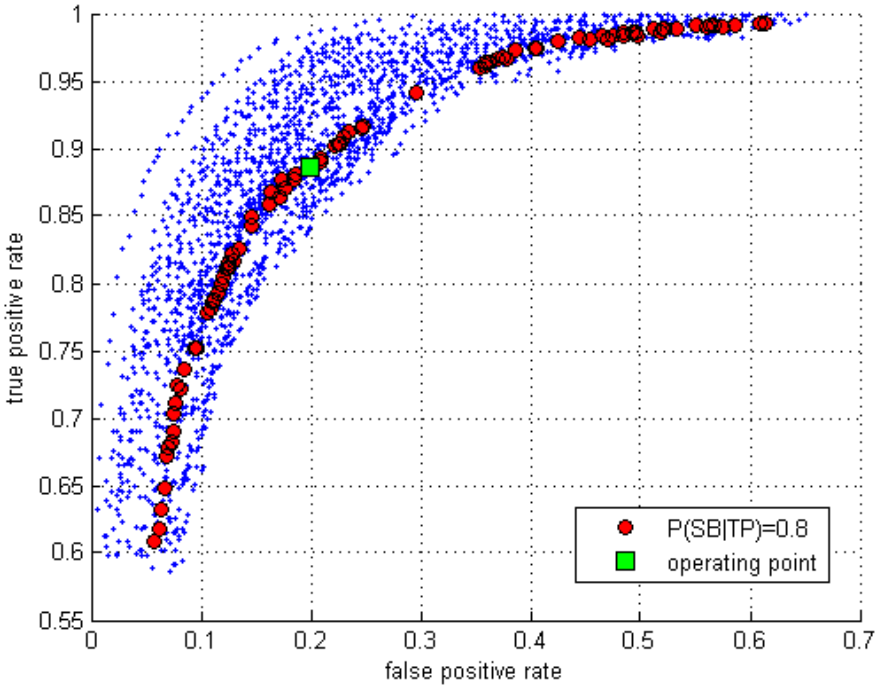

Figure 6.10 Pareto front from the top view.

Although the designed system has shown good performance in detecting conflicts correctly with a small false warning rate and providing a sufficient distance to stop safely, these selections of the system parameters are not definite. Since the Pareto optimality is to search a set of optimal solutions each of which is non-dominated by the other solutions, selecting a particular solution for implementation may depend on other specific design criteria. For example, if the system is required to have a smaller false positive rate for driver comfort, the current operating point needs to be shifted to the left in Figure 6.10, sacrificing the true positive rate. On the other hand, if the same weight is applied to all the objectives, it may be selected at the point closest to the top left corner at (0, 1, 1) in Figure 6.9.

The warning point, specified by D_w, does not greatly affect the overall shape of the resulting ROC curve, as seen in Figure 6.10. If D_w is reduced, warnings occur closer to the intersection, and the prediction performance of the conflict metrics improve; hence

the ROC curve in Figure 6.10 shifts toward the top left corner at (0, 1). The penalty is of course that the warning is more often given too late for stop before the stop-bar.

The methodology used to optimize the driver assistance system design in this study is very general. It particularly addresses situations where the rate of true positives, the rate of false positives, as well as the timing of interventions are all key aspects of the system performance. It is therefore very broadly applicable to driver assistance systems, not just LTAP/OD conflicts at intersections. It is based on a combination of general processes including the developments of a suitable predictive conflict metric, simulation model for Monte Carlo simulations, and design of an assistance system achieved by solving a multiobjective optimization problem. For the LTAP/OD scenario it can also be applied to alternative warning or control concepts, for example where the timing of the warning is varied according to the state of knowledge of the conflict risk and the severity of the possible outcomes.

Chapter 7
Conclusions

A methodology has been proposed for designing a driver assistance system, aimed at reducing the number of intersection crashes. The methodology is shown to be capable of balancing several desired outcomes: a high rate of true positive warnings, a low rate of false positive warnings, plus a high percentage of timely warnings leading to successful braking interventions by the driver. The analysis was conducted for free left turn scenarios in which the left turn vehicle is unaware of a conflicting vehicle traveling in the opposite direction. While the methodology is very general, it has been developed in detail for the left turn across path conflict type. To carry through the design and analysis, several new results have been established and several analysis tasks have been completed: 1) automated extraction of kinematic data relevant to intersection conflicts including simple but novel techniques for time synchronization and data fusion; 2) application of this data to determine and validate improved predictive conflict metrics, including the estimation of acceptable thresholds for gap acceptance; 3) development of a new driver control model for speed and lateral control, based on the concept of *anticipated acceleration*, including extensive validation of that model; and 4) formulating and demonstrating the methodology for objective design.

An important aspect of the contribution has been the comprehensive application of quantitative and predictive methods coupled with the use of naturalistic data, in a research area previously dominated by empirical studies with recruited test subjects. The specific achievements are summarized in more detail as follows.

1) Accurate SV trajectories were reconstructed by multiple use of Kalman filtering including a “constant speed” Kalman filter and angular measurement fusion using

yaw rate from the yaw rate sensor to remove noise in the heading angle of the SV at low speed. The reconstruction of trajectories of POVs was achieved by using the kinematic filters to associate target points, which were detected only relatively to the SV. The quality of the trajectories was not as good as the SV trajectories since the observation of the POVs was made relative to the SVs. It was improved by automatically correcting latency time differences between the relevant sensors and reasonable results for the conflict analysis were obtained.

2) The conflict analyses for intersection left turns were conducted by computing the post encroachment time (PET) of each left turn from the naturalistic driving data. Qualitatively, the resulting PET distributions showed realistic human driver behavior, i.e. they tend to take a shorter gap time in the case of the SV crossing second than in the case of crossing first (Figure 4.3). Quantitatively, the obtained gap acceptance thresholds were found to be similar between Michigan and California drivers [9] increasing the confidence over the generality of the results for U.S. drivers. For each event, the observed PET was predicted by the leading buffer or trailing buffer (LB/TB) in which the predicted speed profile is based on a computed *reference speed profile*. The LB/TB provided more realistic predictions than conventional conflict metrics which use a constant speed assumption (e.g. TTC and GT).

3) The driver model for free left turn scenarios was developed including both the longitudinal and lateral controls. The longitudinal model is based on the *anticipated acceleration reference* (AAR) and the lateral control is based on preview tracking. Monte Carlo simulation results showed a highly-correlated turning behavior between the model and real-world drivers as shown by the similar time histories of the kinematic variables. The model faithfully reproduces the measured speed characteristics of human drivers, and involves a switching of AARs between the stopping and turning targets. Additionally, the driving data analysis has revealed that there is uniformity of maximum lateral acceleration in a turn, even as geometry and speeds vary; this is in contrast to driving in curved

road segments where there is a “reciprocal relationship” of maximum lateral acceleration decreasing with speed.

4) The design methodology for intersection assistance system was performed for free left turn scenarios. It involved: 1) event sampling using the Monte Carlo simulation results; 2) conflict estimation; and 3) parameter optimization based on Pareto optimality. The obtained parameters are predicted to achieve 89 % true-positive rate, 20 % false-positive rate, and 80 % rate of successful braking under true-positive conditions. Therefore, for the free left turn cases, the designed model is expected to detect conflicts at a high accuracy with a significantly smaller false positive rate.

The multiple use of Kalman filtering to reconstruct trajectories was found to be simple and effective; given the prevalence of GPS in navigation fields and the ability of the Kalman filters to remove extraneous noise from such signals, the method should find wider application. Due to the limited field of view of the forward radars, the POV trajectories obtained from the only forward radar data were extrapolated, and satisfactory results were obtained in the conflict analyses in LTAP/OD cases. However, the accuracy of conflict estimation partly depends on the duration of the detection time of a POV, so use of a vehicle-based system to capture POV motions might be less effective for other intersection path-crossing scenarios [2] where the detection time may be shorter.

Since the PET results show that the human driver accepts a shorter time separation in the SV crossing second case than in the crossing second case, it may be implied that their natures are different. In the crossing first case, the SV driver has to judge if the available gap is sufficient to provide an enough distance between the SV and POV in the *future* vehicle configuration when the SV is leaving the encroachment zone. On the other hand, in the crossing second case the left turn maneuver becomes simple for the SV driver to control with feedback; and once the POV has passed, no prediction of the future situation is necessary, the potential for a crash having been removed.

It is essential to select a suitable vehicle configuration and associated conflict point when the LB/TB is calculated. In this study, two configurations were considered for the cases of the SV crossing first and second (Section 1.2). These provide the smallest distances between the SV and POV in the respective cases. The crossing first case is the only conflict of significance if there is only one POV. On the other hand, the crossing second case needs to be considered if multiple POVs exist since an available gap between POVs needs to be evaluated for a safe left turn. Buffer bands can be used to visualize the available gap for each pair of POVs, and the accuracy of the LB/TB can be confirmed by the degree of their distortions. Moreover, this idea can be applied directly to other path-crossing type scenarios once target vehicle configurations and corresponding conflict points are available.

An accurate prediction of the SV speed is crucial in calculating the conflict metrics. The asymptotic convergence (curve fitting) method was used in this study to find the predicted speed profile; this proved satisfactory for free left turn cases, one reason being the relatively small deviation of the vehicle speed from the reference speed profile. However, in other cases where the SV speed drops to near zero as the driver waits for a suitable gap, the initial speed differences are larger and the error between actual and predicted speed profiles is also expected to be larger.

The speed control model based on AAR represents a novel approach to understanding the human driving strategy. Here the visual preview information is presumed to be associated with simple kinematic estimates that can be used to control speed. Another novel aspect of the model is that multiple references can be used simultaneously, with speed control options relating to stopping and turning. It is worth clarifying that, while the model is applied to simulations in which the SV will definitely make the turn, it is derived from situations where braking to rest and turning are both considered feasible. For turning, the transition from the approach stage to turn stage is mirrored by a switch from longitudinal AAR to AAR based on lateral acceleration. It was found that AAR is controlled within a small range, even while the actual longitudinal acceleration from the driving data shows quite large fluctuations. The model explains how this happens, with a number of layers in

the control mechanism; this result speaks strongly against naively screening driving data for patterns that reveal driver control actions. It also emphasizes the need for computational modeling techniques that represent the coupled system of driver-vehicle-environment; otherwise it is impossible to understand the complex dynamic interactions.

The methodology used for the assistance system design has demonstrated a comprehensive procedure including data analyses, modeling, and simulation. In addition, it is based on a quite general approach and could be applied to a wider class of intersection safety systems. For example, warnings might also be given to the POV driver, or the timing of the SV warning might be considered flexible (e.g. earlier warnings given in cases with high conflict probability).

There is a clear difference between the assistance system considered in this study for intersection left turns and other types of safety system (e.g. lane departure warning system). In the former case, it is impossible (at least currently) to determine if the SV driver is aware of an existing potential conflict since the driver's natural behavior during the approach stage and the most likely collision avoidance maneuver is the same, i.e. braking. On the other hand, it is natural to assume that the driver is unaware of a potential conflict in the latter case, in which unusual driving behavior is involved (i.e. lane departure). Then, the assistance system for intersection left turns can annoy the driver with a true positive warning signal if he or she actually intends to stop. Therefore, it may be preferable to investigate alternative human-machine interface concepts, ones that can support a driver's decision to stop rather than warn against a possible turning conflict.

The work presented in this dissertation shows how systematic modeling, analysis, and optimization can be employed to design a safety system that operates in a complex real-world environment. Of course the resulting system would need to be tested further with human subjects and appropriate human-machine interfaces, especially to determine the appropriate constraints placed on the Pareto-optimal solutions.

One limitation in the research presented is the lack of detail in defining the precise functionality and hardware design of the candidate intersection safety system. This should be the subject of future research, as would be the following:

1) A larger LTAP/OD event set, obtained from naturalistic driving data, will be helpful to improve the classification of left turn behavior by driver types such as age and gender.

2) The quality of the POV trajectories is lower than the SV trajectories due to limited radar field of view, and the fact that the kinematics of the POV is measured relative to the SV. This can be improved if site-based data is fused with vehicle-based data.

3) An improved reference velocity profile U_{pred} may reduce the offset between the LB/TB and PET especially for non-free left turns, in which buffer bands tend to be more distorted than in free left turns. As a result, the trade-off between true positives and false positives can be mitigated. One way to achieve this may be to include factors for individual driving styles, as well as factors for traffic conditions obtained from site-based monitoring.

4) Although the SV driver's cognitive process, i.e. perception, recognition and decision, were omitted in free left turns, determining the driver's decision state becomes important in order to improve the system so that it can be applied to the other types of the LTAP/OD conflicts such as misjudgment of gap or POV speed as mentioned in Section 1.1. The decision making may also be affected by other factors such as a phase transition of the traffic signal [90].

5) Additional research is needed to establish and confirm the relationship between speed profiles and intersection geometry. It is expected that left turn drivers turn at a faster speed as the curvature of the turning trajectory becomes smaller, but the analysis in Section 4.6 did not show such a relationship. Further use of the driver

model, validated with expanded data sets for free left turns at multiple intersections, would be the preferred approach.

6) As mentioned in Section 5.6, the AAR model may be expanded to improve understanding of speed selection in general curve driving. It would be particularly interesting to investigate further the difference between curve driving and intersection left turn situations. For example, it might help to understand what kind of information and strategies human drivers use to turn the vehicle by comparing the two situations, curve driving involving the reciprocal relationship as mentioned in Section 5.6 and intersection turns showing constant lateral acceleration.

Appendices

Appendix A
RDCW Instrumentations

A.1 Overall system

The project for the Road Departure Crash Warning (RDCW) system was intended to develop two main functions: lateral drift warning (LDW) and curve speed warning (CSW). Test instruments were prepared with eleven Nissan Altima 3.5SE sedans (model year 2003) (Figure A.1). Figure A.2 shows the RDCW system with architecture installed in the above vehicles.

Figure A.1 Vehicle fleet. (Reproduced from [53]**)**

Table A.1 shows the primary and supporting sensors in the LDW and CSW. Among these, the GPS, yaw rate sensor and accelerometer in the data acquisition system (DAS) were used to reconstruct SV trajectories. For POVs, necessary information about their motion was given by the forward radars. In addition, video clips by the CCD camera were accessed to confirm manually if the reconstructed trajectories were reasonable. Note that there were two GPSs installed in the vehicles. One with differential corrections was

installed in the DAS and the other was in the CSW. For the SV trajectory reconstruction, the former GPS was adopted.

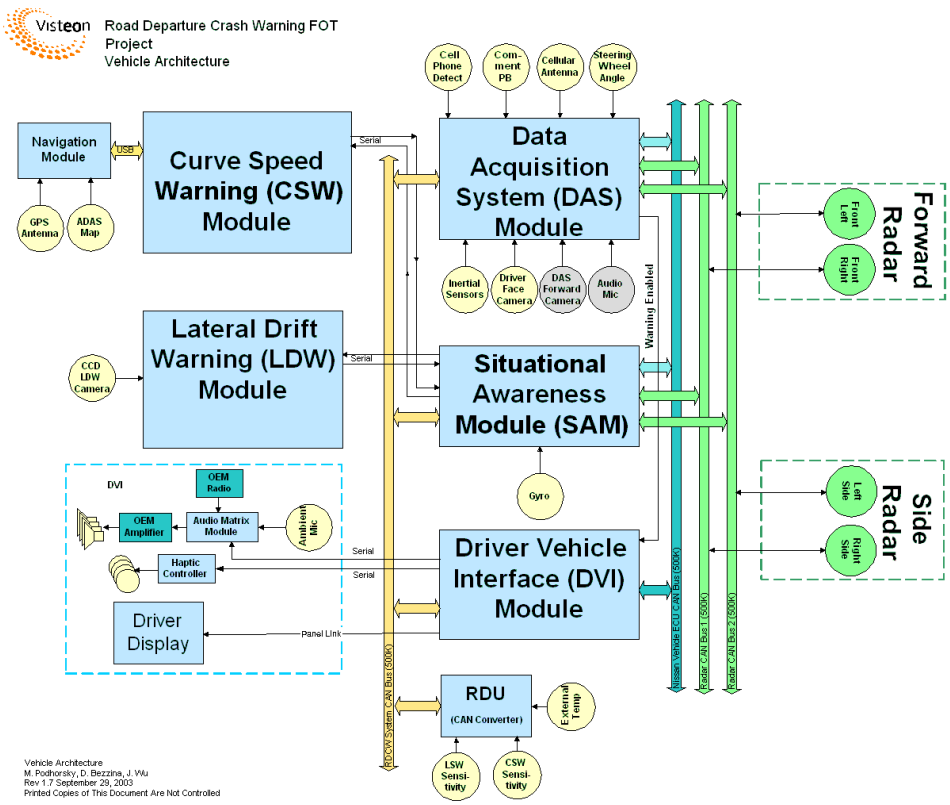

Figure A.2 Schematic diagram of the RDCW system architecture. (Reproduced from [53]**)**

Table A.1 Key sensors used by the LDW and CSW systems. (Reproduced from [53]**)**

Sensor	LDW system sensors		CSW system	
	Primary	Supporting	Primary	Supporting
Forward CCD camera	X			X
GPS		X	X	
Digital map		X	X	
Digital map look-aside database		X		
Vehicle speed	X	X	X	
Yaw rate gyro		X	X	
Driver brake switch		X		
Driver turn signal switch		X		X
Forward-looking radars		X		
Side-looking radars		X		

The CCD camera was installed inside the cabin on the front windshield. The forward radars and the side radars were mounted inside the front bumper as shown in Figure A.3.

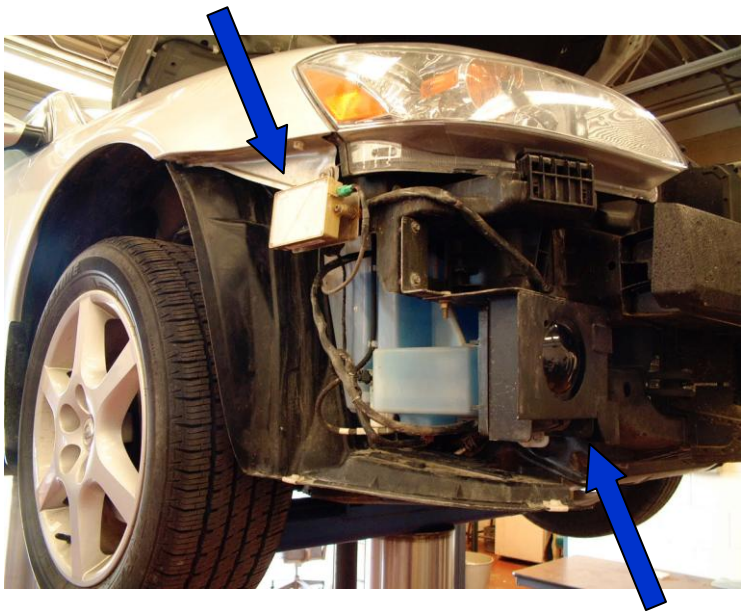

Figure A.3 Physical installation of the forward and side radars. (Reproduced from [53]**)**

It is important to confirm that the field operational test data contains naturalistic driver behaviors at left turns at intersections without warnings by the LDW or CSW. The LDW suppresses warning requests in particular situations;

1) The vehicle speed is 11.1 m/s or has been $\leq$11.1 m/s within the last 5 s,
2) The vehicle has completed a lane change within the last 2 s,
3) The lateral speed has exceeded 1m/s within the last 2 s,
4) A turn signal has been on within the last 5 s,
5) The brake pedal has been pressed within the last 5 s and
6) The curve radius is ≤ 250 m.

Also, the CSW suppresses warning requests in the following cases;

1) The vehicle speed is below 8 m/s and
2) The vehicle deceleration is less than the requested deceleration.

The CSW determines the vehicle position and a predicted path using digital map information. Given a predicted path, it provides a warning to slow down the vehicle

speed if an excessive vehicle speed is anticipated by comparing it with a threshold for the lateral speed.

With those conditions, there were no events detected with warnings from the LDW. On the other hand, there were 5 events with warnings from the CSW by 2 drivers at 2 intersections during left turns. Excluding these 5 events, it can be said that the driver behavior on left turns in the field operational test data is assumed to be naturalistic.

A.2 Specifications of instruments

Specifications of the instruments relevant to the left turn analyses are shown in the tables below.

Table A.2 Accelerometer.

Input range	±2 g
Zero g drift	±30 mV
Sensitivity	1 V/g
Noise RMS	1 mg
Bandwidth	DC -50 Hz
Data sampling rate	20 Hz

Table A.3 CCD camera.

Color	Monochrome
Horizontal FOV	40±4 deg
Vertical FOV	30±3 deg
Data sampling rate	10 Hz

Table A.4 Forward radars.

Range (moving objects)	120±1 m
Range (stationary objects)	60±1 m
Range rate	±48.88±0.17 m/s
Horizontal FOV	8±0.6 deg from 40 to 100 m
Vertical FOV	3 deg
Frequency	77 GHz
Data sampling rate	20 Hz

Table A.5 GPS.

Position error (horizontal direction)	Significantly less than 1m at 2σ (95 %) and close to 1m at 3 σ (99 %)
Position error (vertical direction)	2 to 2.5 times greater than horizontal error

Table A.6 Yaw rate transducer.

Sensitivity (-30 to 80 ºC)	25.00±2.5 mV/deg/sec
Sensitivity drift (-30 to 80 ºC)	±5 %
Dynamic range	±60 deg/s
Linearity (at -50 [deg/s])	±0.5 %
Linearity (at -60 [deg/s])	±5 %
Frequency response at 7 [Hz]	-7.0 dB (minimum) and -2.0 dB (maximum)
Cross axis sensitivity	±5.0 %
Data sampling rate	10 Hz

Appendix B
Transformation of Geographical Coordinates into Cartesian Coordinates

The GPS coordinates given in the geographical coordinates (θ, γ) can be transformed into the Cartesian coordinates as follows.

A point on the earth's surface, *P*, is denoted as,

$$\{\mathbf{r}_P\}_{spherical} = R_e \mathbf{e}_r \tag{B.1}$$

by using the spherical coordinate system. R_e is the radius of the earth and $\mathbf{e}_r$ is a unit vector which can be rewritten by a set of unit vectors of the *XYZ* global (fixed) coordinate system as,

$$\begin{aligned} \mathbf{e}_r &= \cos\phi\mathbf{K} + \sin\phi\mathbf{n} \\ &= \sin\phi\cos\theta\mathbf{I} + \sin\phi\sin\theta\mathbf{J} + \cos\phi\mathbf{K}. \end{aligned} \tag{B.2}$$

Thus, the point, *P*, can be given in the *XYZ* global coordinate system by,

$$\begin{aligned} \{\mathbf{r}_P\}_{XYZ} &= R_e\left(\sin\phi\cos\theta\mathbf{I} + \sin\phi\sin\theta\mathbf{J} + \cos\phi\mathbf{K}\right) \\ &= R_e\left(\cos\gamma\cos\theta\mathbf{I} + \cos\gamma\sin\theta\mathbf{J} + \sin\gamma\mathbf{K}\right). \end{aligned} \tag{B.3}$$

Then, a rotation matrix to rotate the global axes about the *Z* axis by $-(\pi/2-\theta)$ followed by another rotation about the *X* axis by $(\pi-\phi)$ is given by,

$$\mathbf{R} = \begin{bmatrix} 1 & 0 & 0 \\ 0 & -\cos\phi & \sin\phi \\ 0 & -\sin\phi & -\cos\phi \end{bmatrix} \begin{bmatrix} \sin\theta & -\cos\theta & 0 \\ \cos\theta & \sin\theta & 0 \\ 0 & 0 & 1 \end{bmatrix}. \tag{B.4}$$

Therefore,

$$\{\mathbf{r}_P\}_{X'Y'Z'} = \mathbf{R}\{\mathbf{r}_P\}_{XYZ}. \tag{B.5}$$

The resulted orientation becomes the one shown in Figure B.1(b).

For the reconstruction of the SV trajectory, the rotation matrix needs to be defined only once for each left turn by a datum position specified by, (θ_0, γ_0), such as the intersection node or initial SV coordinates in a left turn event, and this matrix can be used for the other positions too since the vehicle motion is considered approximately planar. Therefore, the transformation of SV coordinates from the *XYZ* global coordinate system to the $X'Y'Z'$ local coordinate system is described by,

$$\{\mathbf{r}_{SV}\}_{X'Y'Z'} = \mathbf{R}_0\{\mathbf{r}_{SV}\}_{XYZ} \tag{B.6}$$

where

$$\mathbf{R}_0 = \begin{bmatrix} 1 & 0 & 0 \\ 0 & -\cos\phi_0 & \sin\phi_0 \\ 0 & -\sin\phi_0 & -\cos\phi_0 \end{bmatrix} \begin{bmatrix} \sin\theta_0 & -\cos\theta_0 & 0 \\ \cos\theta_0 & \sin\theta_0 & 0 \\ 0 & 0 & 1 \end{bmatrix}. \tag{B.7}$$

The radius of the earth used here is defined as 6,371,000 m. Although the value is approximate because of the non-spherical shape of the earth, the distance between a final position of the SV in a typical left turn event obtained by using the semimajor axis and another obtained by using the semiminor axis is about 15 cm. Therefore, this deviation is negligible in the conflict metric analysis.

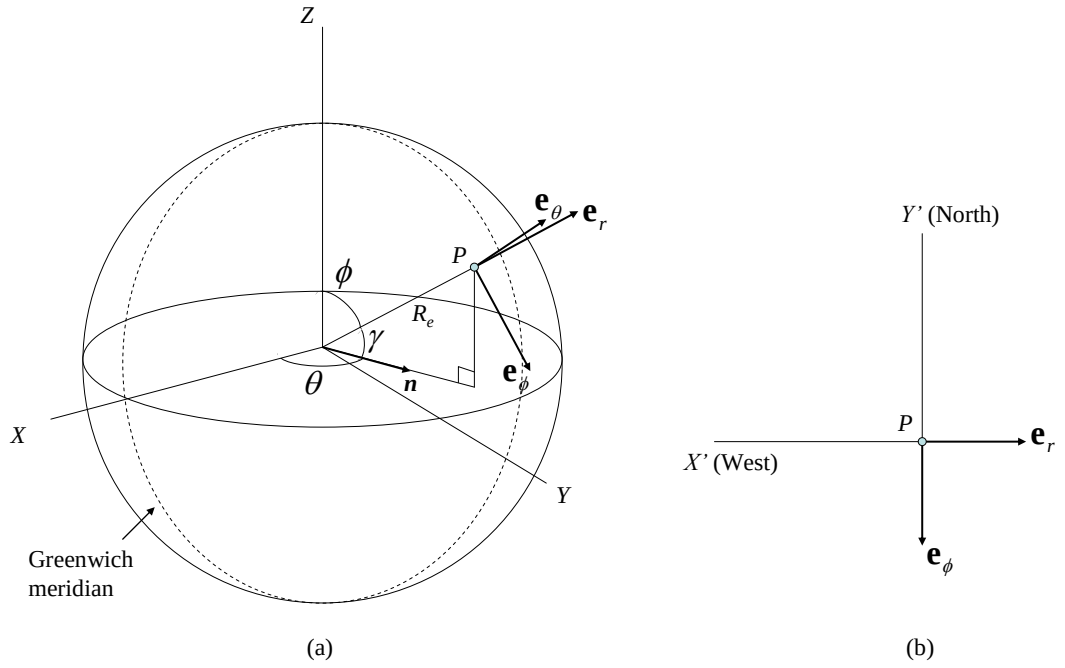

Figure B.1 Coordinate systems used in the coordinate transformation. (a) three dimensional view and (b) top view of the designated coordinate orientation for the planar motion.

Appendix C
Equations for X-Y Kalman Filter

The Kalman filters used in the trajectory reconstruction share common characteristics as mentioned in Chapter 3, that is, the Wiener process acceleration model, varying time step and backward sweep before forward sweep. First, the Wiener process acceleration model [70], which assumes that the time derivative of the acceleration (jerk) is a zero mean white noise, is described by the following equations;

$$\mathbf{x}(k+1) = \mathbf{A}(k)\mathbf{x}(k) + \mathbf{G}v \tag{C.1}$$

where

$$\mathbf{x} = \begin{Bmatrix} x \\ v_x \\ a_x \\ y \\ v_y \\ a_y \end{Bmatrix},\ \mathbf{A}(k) = \begin{bmatrix} 1 & T(k) & 0.5T(k)^2 & 0 & 0 & 0 \\ 0 & 1 & T(k) & 0 & 0 & 0 \\ 0 & 0 & 1 & 0 & 0 & 0 \\ 0 & 0 & 0 & 1 & T(k) & 0.5T(k)^2 \\ 0 & 0 & 0 & 0 & 1 & T(k) \\ 0 & 0 & 0 & 0 & 0 & 1 \end{bmatrix} \text{ and}$$

$$\mathbf{G}(k) = \begin{bmatrix} 0.5T(k)^2 \\ T(k) \\ 1 \\ 0.5T(k)^2 \\ T(k) \\ 1 \end{bmatrix}, \tag{C.2}$$

and $T(k) = t_{k+1} - t_k$ for one time step to indicate varying time steps.

The measurement equation is defined as

$$\mathbf{y}(k) = \mathbf{C}\mathbf{x}(k) + w \tag{C.3}$$

where

$$\mathbf{C} = \begin{bmatrix} 1 & 0 & 0 & 0 & 0 & 0 \\ 0 & 0 & 0 & 1 & 0 & 0 \end{bmatrix}. \tag{C.4}$$

The covariance matrices **Q** and **R** for the process noise, *v*, and measurement noise are given by

$$\mathbf{Q}(k) = \sigma_v{}^2 \mathbf{G}(k)\mathbf{G}(k)^T \tag{C.5}$$

and

$$\mathbf{R} = \sigma_w{}^2 \mathbf{C}\mathbf{C}^T, \tag{C.6}$$

where $\sigma_v{}^2$ and $\sigma_w{}^2$ are the standard deviations of *v* and *w* respectively. The state prediction and measurement prediction are represented by

$$\begin{aligned} \hat{\mathbf{x}}(k+1 \mid k) &= \mathbf{A}(k)\hat{\mathbf{x}}(k \mid k) \\ \hat{\mathbf{y}}(k+1 \mid k) &= \mathbf{C}\hat{\mathbf{x}}(k+1 \mid k) \end{aligned} \tag{C.7}$$

and the updated state estimate is given by

$$\hat{\mathbf{x}}(k+1 \mid k+1) = \hat{\mathbf{x}}(k+1 \mid k) + \mathbf{W}(k+1)\{\mathbf{y}(k+1) - \hat{\mathbf{y}}(k+1 \mid k)\} \tag{C.8}$$

where **W** is the filter gain that is found by

$$\mathbf{W}(k+1) = \{\mathbf{A}(k)\mathbf{P}(k \mid k)\mathbf{A}^T(k) + \mathbf{Q}(k)\}\mathbf{C}^T\{\mathbf{R} + \mathbf{C}\mathbf{P}(k+1 \mid k)\mathbf{C}^T\}^{-1}. \quad \text{(C.9)}$$

The state covariance matrix **P** is described as

$$\begin{aligned}\mathbf{P}(k+1 \mid k) &= \mathbf{A}(k)\mathbf{P}(k \mid k)\mathbf{A}^T(k) + \mathbf{Q}(k) \\ \mathbf{P}(k+1 \mid k+1) &= \mathbf{P}(k+1 \mid k) - \mathbf{W}(k+1)\{\mathbf{R}(k+1) + \mathbf{C}\mathbf{P}(k+1 \mid k)\mathbf{C}^T\}\mathbf{W}^T(k+1).\end{aligned} \quad \text{(C.10)}$$

Since appropriate initial conditions must be given for the Kalman filter (forward sweep), another Kalman filter is swept from the last point of the SV path (backward sweep) to find suitable initial conditions for the forward Kalman filter. The combination of these Kalman filters can increase the overall accuracy of the estimates of the SV motion. The system equations for the backward Kalman filter are described similarly to the forward Kalman filter as follows,

$$\mathbf{x}(k) = \mathbf{A}^{-1}(k+1)\mathbf{x}(k+1) + \mathbf{G}v \quad \text{(C.11)}$$

with the same measurement equation as for the forward Kalman filter,

$$\mathbf{y}(k) = \mathbf{C}\mathbf{x}(k) + w. \quad \text{(C.20)}$$

Appendix D
Trajectories of Vehicle Corners

In order to calculate the conflict metrics, the size of the vehicles must be considered. Thus, the trajectories of the corner points of the vehicles were constructed by using $\left(\hat{X},\hat{Y}\right)$, $\tilde{\theta}$ and the geometry of the vehicle body. According to Figure D.1, the position vectors of the corner points are given by

$$\begin{aligned}
\mathbf{r}_1 &= \left(\hat{X} + L'_a\cos\tilde{\theta} + L_c\sin\tilde{\theta}\right)\mathbf{I} + \left(\hat{Y} + L'_a\sin\tilde{\theta} - L_c\cos\tilde{\theta}\right)\mathbf{J} \\
\mathbf{r}_2 &= \left(\hat{X} + L'_a\cos\tilde{\theta} - L_c\sin\tilde{\theta}\right)\mathbf{I} + \left(\hat{Y} + L'_a\sin\tilde{\theta} + L_c\cos\tilde{\theta}\right)\mathbf{J} \\
\mathbf{r}_3 &= \left(\hat{X} - L'_b\cos\tilde{\theta} + L_c\sin\tilde{\theta}\right)\mathbf{I} + \left(\hat{Y} - L'_b\sin\tilde{\theta} - L_c\cos\tilde{\theta}\right)\mathbf{J} \\
\mathbf{r}_4 &= \left(\hat{X} - L'_b\cos\tilde{\theta} - L_c\sin\tilde{\theta}\right)\mathbf{I} + \left(\hat{Y} - L'_b\sin\tilde{\theta} + L_c\cos\tilde{\theta}\right)\mathbf{J}
\end{aligned} \tag{D.1}$$

Instead of applying the Kalman filter to each corner trajectory, the first and second time derivatives are computed to find the velocity and acceleration by using the trajectory of O'. The velocity vectors can be represented as

$$\begin{aligned}
\dot{\mathbf{r}}_1 &= \left(\dot{\hat{X}} - L'_a\dot{\tilde{\theta}}\sin\tilde{\theta} + L_c\dot{\tilde{\theta}}\cos\tilde{\theta}\right)\mathbf{I} + \left(\dot{\hat{Y}} + L'_a\dot{\tilde{\theta}}\cos\tilde{\theta} + L_c\dot{\tilde{\theta}}\sin\tilde{\theta}\right)\mathbf{J} \\
\dot{\mathbf{r}}_2 &= \left(\dot{\hat{X}} - L'_a\dot{\tilde{\theta}}\sin\tilde{\theta} - L_c\dot{\tilde{\theta}}\cos\tilde{\theta}\right)\mathbf{I} + \left(\dot{\hat{Y}} + L'_a\dot{\tilde{\theta}}\cos\tilde{\theta} - L_c\dot{\tilde{\theta}}\sin\tilde{\theta}\right)\mathbf{J} \\
\dot{\mathbf{r}}_3 &= \left(\dot{\hat{X}} + L'_b\dot{\tilde{\theta}}\sin\tilde{\theta} + L_c\dot{\tilde{\theta}}\cos\tilde{\theta}\right)\mathbf{I} + \left(\dot{\hat{Y}} - L'_b\dot{\tilde{\theta}}\cos\tilde{\theta} + L_c\dot{\tilde{\theta}}\sin\tilde{\theta}\right)\mathbf{J} \\
\dot{\mathbf{r}}_4 &= \left(\dot{\hat{X}} + L'_b\dot{\tilde{\theta}}\sin\tilde{\theta} - L_c\dot{\tilde{\theta}}\cos\tilde{\theta}\right)\mathbf{I} + \left(\dot{\hat{Y}} - L'_b\dot{\tilde{\theta}}\cos\tilde{\theta} - L_c\dot{\tilde{\theta}}\sin\tilde{\theta}\right)\mathbf{J}.
\end{aligned} \tag{D.2}$$

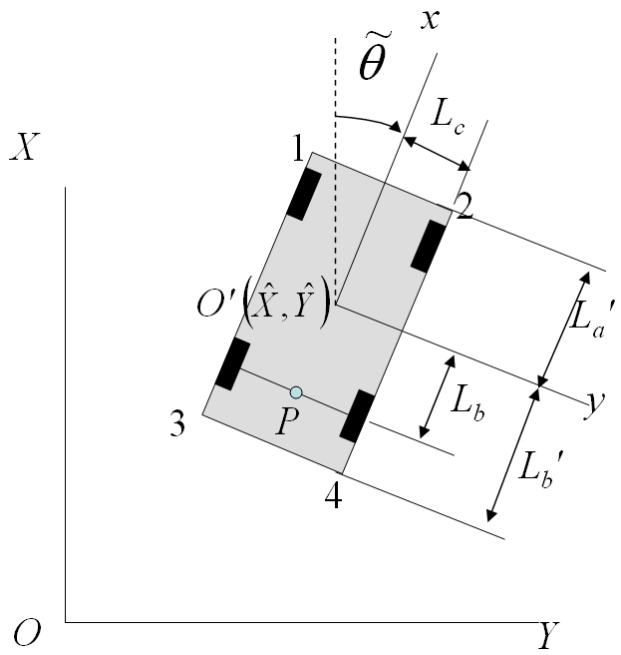

Figure D.1 Geometry of the subject vehicle and coordinate system for the corner trajectories from the top view.

The acceleration vectors are

$$
\begin{aligned}
\ddot{\mathbf{r}}_1 &= \left(\ddot{\hat{X}} - L_a'\ddot{\tilde{\theta}}\sin\tilde{\theta} - L_a'\dot{\tilde{\theta}}^2\cos\tilde{\theta} + L_c\ddot{\tilde{\theta}}\cos\tilde{\theta} - L_c\dot{\tilde{\theta}}^2\sin\tilde{\theta} \right)\mathbf{I} \\
&\quad + \left(\ddot{\hat{Y}} - L_a'\ddot{\tilde{\theta}}\sin\tilde{\theta} - L_a'\dot{\tilde{\theta}}^2\cos\tilde{\theta} + L_c\ddot{\tilde{\theta}}\cos\tilde{\theta} - L_c\dot{\tilde{\theta}}^2\sin\tilde{\theta} \right)\mathbf{J} \\
\ddot{\mathbf{r}}_2 &= \left(\ddot{\hat{X}} - L_a'\ddot{\tilde{\theta}}\sin\tilde{\theta} - L_a'\dot{\tilde{\theta}}^2\cos\tilde{\theta} - L_c\ddot{\tilde{\theta}}\cos\tilde{\theta} + L_c\dot{\tilde{\theta}}^2\sin\tilde{\theta} \right)\mathbf{I} \\
&\quad + \left(\ddot{\hat{Y}} - L_a'\ddot{\tilde{\theta}}\sin\tilde{\theta} - L_a'\dot{\tilde{\theta}}^2\cos\tilde{\theta} - L_c\ddot{\tilde{\theta}}\cos\tilde{\theta} + L_c\dot{\tilde{\theta}}^2\sin\tilde{\theta} \right)\mathbf{J} \\
\ddot{\mathbf{r}}_3 &= \left(\ddot{\hat{X}} + L_b'\ddot{\tilde{\theta}}\sin\tilde{\theta} + L_b'\dot{\tilde{\theta}}^2\cos\tilde{\theta} + L_c\ddot{\tilde{\theta}}\cos\tilde{\theta} - L_c\dot{\tilde{\theta}}^2\sin\tilde{\theta} \right)\mathbf{I} \\
&\quad + \left(\ddot{\hat{Y}} - L_b'\ddot{\tilde{\theta}}\cos\tilde{\theta} + L_b'\dot{\tilde{\theta}}^2\sin\tilde{\theta} + L_c\ddot{\tilde{\theta}}\sin\tilde{\theta} + L_c\dot{\tilde{\theta}}^2\cos\tilde{\theta} \right)\mathbf{J} \\
\ddot{\mathbf{r}}_4 &= \left(\ddot{\hat{X}} + L_b'\ddot{\tilde{\theta}}\sin\tilde{\theta} + L_b'\dot{\tilde{\theta}}^2\cos\tilde{\theta} - L_c\ddot{\tilde{\theta}}\cos\tilde{\theta} + L_c\dot{\tilde{\theta}}^2\sin\tilde{\theta} \right)\mathbf{I} \\
&\quad + \left(\ddot{\hat{Y}} - L_b'\ddot{\tilde{\theta}}\cos\tilde{\theta} + L_b'\dot{\tilde{\theta}}^2\sin\tilde{\theta} - L_c\ddot{\tilde{\theta}}\sin\tilde{\theta} - L_c\dot{\tilde{\theta}}^2\cos\tilde{\theta} \right)\mathbf{J}.
\end{aligned}
\tag{D.3}
$$

It is needed to find analytical expressions for $\dot{\tilde{\theta}}$ and $\ddot{\tilde{\theta}}$ in the above equations. This can be achieved by using the constraint on the center of the rear wheels by assuming that they are connected by a rigid shaft. Since they are velocity-constrained (non-holonomic), the constraint equation can be found from the differential of the position vector. The position vector of the point *P* is

$$\mathbf{r}_P = \left(\hat{X} - L_b \cos\tilde{\theta}\right)\mathbf{I} + \left(\hat{Y} - L_b \sin\tilde{\theta}\right)\mathbf{J} \tag{D.4}$$

and thus, after the coordinate transformation from the global coordinate system to the local coordinate system, the differential of this vector is written by

$$\begin{aligned} d\mathbf{r}_P &= \left(d\hat{X} + (L_b \sin\tilde{\theta})d\tilde{\theta}\right)\mathbf{I} + \left(d\hat{Y} - (L_b \cos\tilde{\theta})d\tilde{\theta}\right)\mathbf{J} \\ &= \left(\cos\tilde{\theta}d\hat{X} + \sin\tilde{\theta}d\hat{Y}\right)\mathbf{i} + \left(-\sin\tilde{\theta}d\hat{X} + \cos\tilde{\theta}d\hat{Y} - L_b d\tilde{\theta}\right)\mathbf{j} \end{aligned} \tag{D.5}$$

The rear wheels are constrained in the lateral direction by assuming the tire slip is negligible, so the second term of the last equation becomes zero. Consequently, $\dot{\tilde{\theta}}$ and $\ddot{\tilde{\theta}}$ are given by

$$\dot{\tilde{\theta}} = \frac{-\dot{\hat{X}}\sin\tilde{\theta} + \dot{\hat{Y}}\cos\tilde{\theta}}{L_b} \tag{D.6}$$

and

$$\ddot{\tilde{\theta}} = \frac{-\ddot{\hat{X}}\sin\tilde{\theta} - \dot{\hat{X}}\dot{\tilde{\theta}}\cos\tilde{\theta} + \ddot{\hat{Y}}\cos\tilde{\theta} - \dot{\hat{Y}}\dot{\tilde{\theta}}\sin\tilde{\theta}}{L_b}. \tag{D.7}$$

Appendix E
Control Gain Tuning

E.1 Longitudinal Control

The longitudinal and lateral control gains are selected by a simple analysis using the linear control theory to achieve a desired phase margin. Figure E.1 shows the block diagram of the inner feedback loop in the longitudinal control. It is noted that the saturation integrator which limits the rate of the pedals is replaced with a regular integrator for simplicity without loss of generality for normal driving.

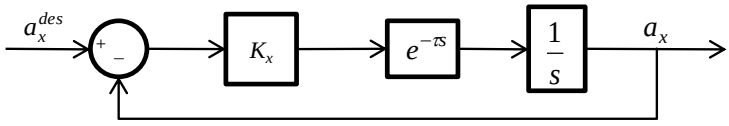

Figure E.1 Inner feedback loop of the longitudinal control.

The open-loop transfer function of this system in the frequency domain is

$$G_{o.l.}(j\omega) = \frac{K_x e^{-j\omega\tau}}{j\omega} \tag{E.1}$$

and its amplitude ratio and phase angle are

$$\left|G_{o.l.}(j\omega)\right| = \frac{K_x}{\omega} \tag{E.2}$$

and

$$\angle G_{o.l.}(j\omega) = -\tau\omega - \tan^{-1}\omega \tag{E.3}$$

respectively. Since the gain crossover frequency $\omega_{g.c.} = K_x$, equation (E.3) becomes

$$\angle G_{o.l.}(j\omega)\big|_{\omega=\omega_{g.c.}} = -\tau K_x - \frac{\pi}{2}. \tag{E.4}$$

The required phase angle to achieve a desired phase margin is then

$$\angle G_{o.l.}(j\omega)\big|_{\omega=\omega_{g.c.}} = -\pi + \gamma\frac{\pi}{180°} \tag{E.5}$$

where γ is phase margin in degrees. Combining equations (E.4) and (E.5), we get

$$K_x = \frac{\pi}{\tau}\left(\frac{1}{2} - \frac{5}{900}\gamma\right) \tag{E.6}$$

For $\gamma = 65°$ and $\tau = 0.2\,\text{s}$, $K_x = 2.18\,\text{s}^{-1}$ is selected.

E.2 Lateral Control

The lateral control contains the gain, K_y and non-dimensional sensitivity factor K_r of the yaw angle error to the yaw rate error as shown in equations (5.8) and (5.9). Also, the preview time T_p which affects the tracking performance is included. The procedure of adjusting these parameters is explained in the following.

First, K_y is considered. Since the yaw rate is inputted to the controller block, it is necessary to include the lateral dynamics of the vehicle, for which the bicycle model is chosen in this analysis. The regular integrator is substituted for the saturating integrator in the original block diagram as in Section E.1. The block diagram used for tuning K_y and

K_r is shown in Figure E.2. The open loop transfer function for the inner loop is used for tuning K_y and that for the outer loop is for tuning K_r.

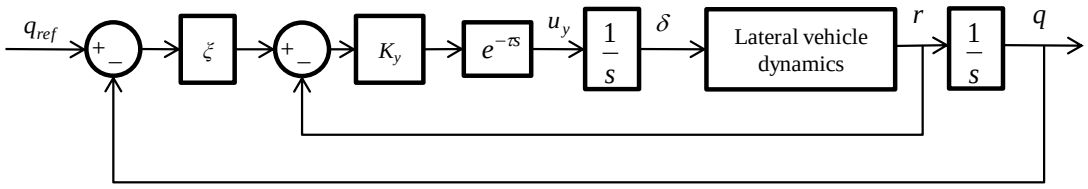

Figure E.2 Block diagram of lateral control.

The bicycle model is given by the following equations

$$\begin{cases} \dot{\mathbf{x}} = \mathbf{A}\mathbf{x} + \mathbf{B}u \\ y = \mathbf{C}\mathbf{x} + \mathbf{D}u \end{cases} \tag{E.7}$$

where

$$\mathbf{x} = \begin{Bmatrix} \beta \\ r \end{Bmatrix},\ u = \delta,\ \mathbf{A} = \begin{bmatrix} -\dfrac{C_{\alpha f} + C_{ar}}{mU_0} & -\dfrac{L_a C_{\alpha f} - L_b C_{ar}}{mU_0{}^2} - 1 \\ -\dfrac{L_a C_{\alpha f} - L_b C_{ar}}{I_z} & -\dfrac{L_a{}^2 C_{\alpha f} + L_b{}^2 C_{ar}}{I_z U_0} \end{bmatrix},$$
$$\mathbf{B} = \begin{bmatrix} \dfrac{C_{\alpha f}}{mU_0} \\ \dfrac{L_a C_{\alpha f}}{I_z} \end{bmatrix},\ \mathbf{C} = \begin{bmatrix} 0 & 1 \end{bmatrix} \text{ and } \mathbf{D} = 0. \tag{E.8}$$

Table E.1 shows descriptions of the variables and parameters. These numbers were taken from the CarSim® vehicle used for the Monte Carlo simulations.

Table E.1 Variables and parameters in Equation (E.8).

Name	Description	Value
β	Body slip angle	(variable) rad
r	Yaw rate	(variable) rad/s
δ	Steer angle	(variable) rad
$C_{\alpha f}$	Front cornering stiffness (both tires)	7000 N
$C_{\alpha r}$	Rear cornering stiffness (both tires)	5000 N
L_a	Distance between the front axle and vehicle mass center	0.962 m
L_b	Distance between the rear axle and vehicle mass center	1.795 m
m	Vehicle mass	1567 kg
U_0	Vehicle speed	10 m/s
I_z	Yaw moment of inertia	2535 kgm^2

The open loop transfer function is given by

$$\begin{aligned} G_{o.l.}^{inner}(j\omega) &= \frac{K_y e^{-j\omega\tau}}{j\omega}\mathbf{C}\left[(j\omega\mathbf{I}-\mathbf{A})^{-1}\mathbf{B}+\mathbf{D}\right] \\ &= K_y \frac{e^{-j0.2\omega}(j1.063\omega+0.9717)}{j\omega(1.554-\omega^2)-1.657\omega^2} \end{aligned} \tag{E.9}$$

The frequency response of equation (E.9) is shown for $K_y = 0.75$. The desired phase margin is set to $\gamma = 30°$ in order to avoid slow response. This phase margin might be small, but the system will be stabilized by the outer loop which is associated with the yaw angle error part in equation (5.9). This is explained in the later part of this section. In the simulation model for the batch simulations including the CarSim vehicle model, the lateral input is given to the steering wheel instead of the front wheel, so K_y is modified by multiplying the steering ratio (1:16), i.e. $K_y^{sw} = 0.75 \times 16 = 12$.

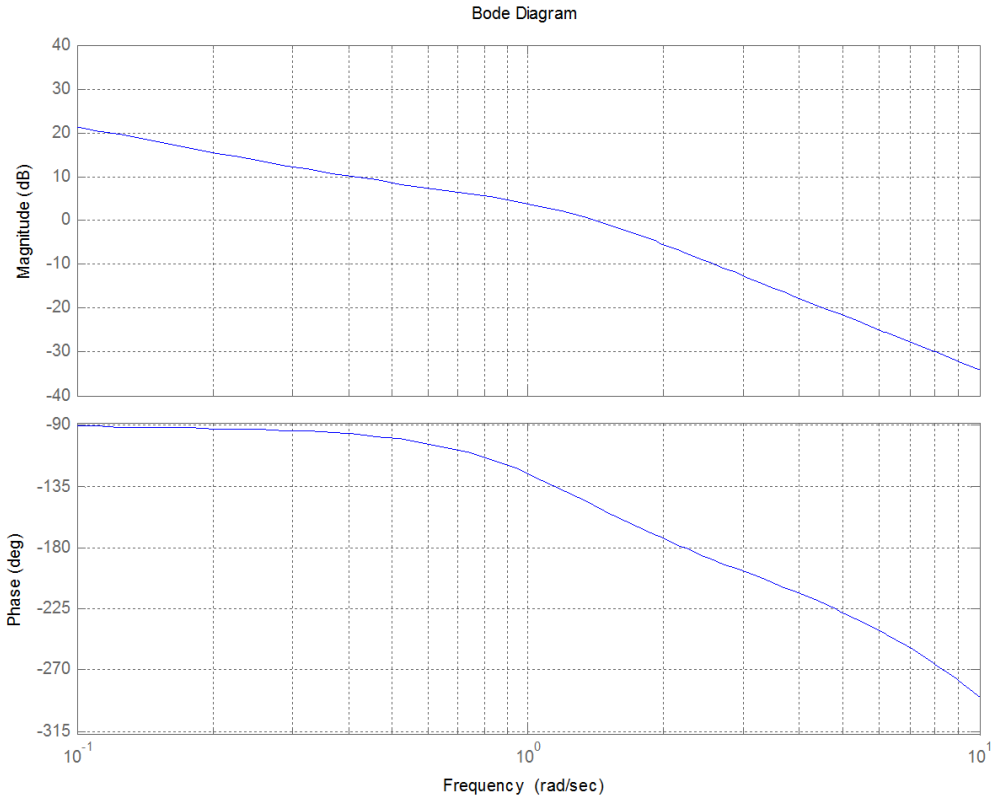

Figure E.3 Frequency response for tuning K_y.

Next, the second control parameter K_r is considered. In practice, ξ is tuned instead of K_r for convenience as explained in the following. Extracting the yaw angle error contribution to the reference yaw rate,

$$u_y = K_y e^{-\varpi}\left(\frac{K_r U\tilde{\Delta}\psi}{d} - r\right). \tag{E.10}$$

Since $T_p \approx d/U$ and a constant value is assumed for T_p, $\xi = K_r U/d$ is defined and thus

$$u_y = K_y e^{-\varpi}\left(\xi\tilde{\Delta}\psi - r\right). \tag{E.11}$$

The open loop transfer function for the outer loop is

$$G_{o.l.}^{outer} = \frac{K_y \xi e^{-j0.2\omega}(j2.656\omega + 2.429)}{j\omega^3(\omega^2 - 1.554) + 1.657\omega^4 + K_y e^{-j0.2\omega}\omega(j2.429 - 2.656\omega)}. \qquad \text{(E.12)}$$

In order to avoid a slow response, $\xi = 0.59$ is adopted and a 65 degree of phase margin is achieved using equation (E.12) as shown in Figure E.4. The transport delay is approximated by $1/(1 + j0.2\omega)$.

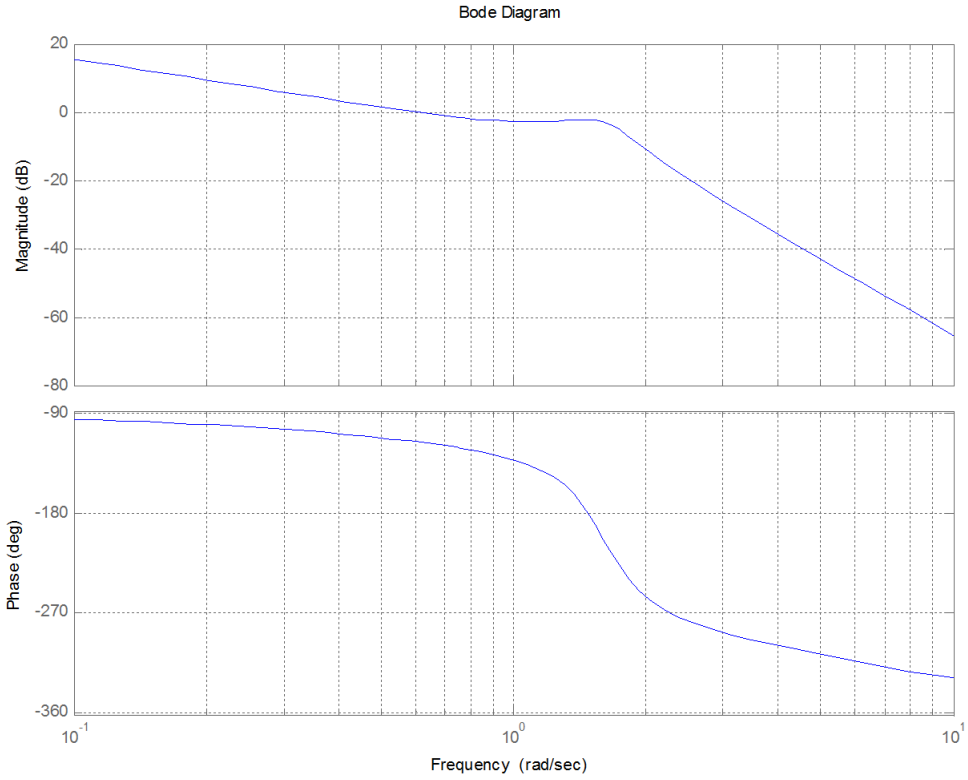

Figure E.4 Frequency response for tuning ξ.

Finally, the preview time T_p is adjusted by minimizing the root mean square error of the lateral deviation during a left turn. T_p was tested for the range [0.4, 3.4] s with 0.2 s intervals. The K_y and ξ values selected above and a constant vehicle speed (U=6 m/s) were used. In addition, the same desired left turn path and driver parameters were used for all T_p values. As can be seen in the figure below, $T_p = 1.6$ s shows the best tracking performance and thus $K_r = \xi T_P = 0.94$.

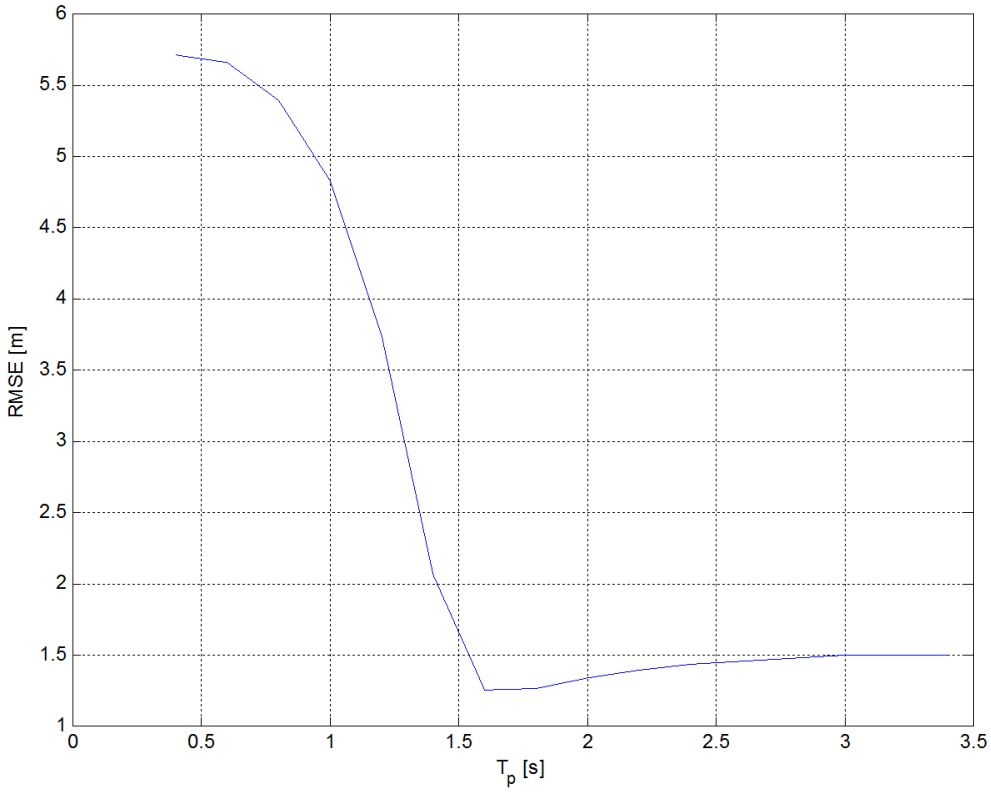

Figure E.5 Root mean square error in the lateral deviation vs. preview time.

Appendix F
Identification of Hard Braking Events

The braking response of each hard braking event in the field operational test for the Automotive Collision Avoidance Systems (ACAS) was approximated by the following first-order response,

$$a_x = \begin{cases} A\left(1 - e^{-(t-t_d)/\tau}\right), & t_d < t \le t_{\text{at max decel}} \\ 0 & , 0 \le t \le t_d \end{cases} \qquad \text{(F.1)}$$

where A is the deceleration amplitude, t_d is the time delay in the beginning region of the braking period and τ is the time constant of the first-order response. Before curve fitting, the acceleration curve of raw data was shifted so that the amplitude at the brake initiation and time are both zero. Figure F.1 shows an example of the original acceleration curve after the preliminary treatment and a fitted curve obtained. Figure F.2 shows histograms of the three parameters (A, t_d and τ) for the 88 events.

The histograms of the random variables which are the natural logarithms $X = \ln(.)$ of $|A| - 3.3$, $t_d + \tau$ and τ and results of normal distribution fitting are shown in Figure F.3. The first two variables were derived from the original model parameters, since $\ln|A|$ and $\ln t_d$ did not show normal distributions by themselves alone. The mean values of $|A| - 3.3$, $t_d + \tau$ and τ are 0.27, 0.32 and −0.19 respectively and the covariance matrix for their natural logarithms, $\ln(|A| - 3.3)$, $\ln(t_d + \tau)$ and $\ln \tau$ is

$$\mathbf{C} = \begin{bmatrix} 0.2655 & -0.0513 & -0.0490 \\ -0.0513 & 0.1108 & 0.0752 \\ -0.0490 & 0.0752 & 0.0776 \end{bmatrix}. \tag{F.2}$$

Then, a correlated set of these variables $\mathbf{y} = \left[\ln(|A| - 3.3), \ln(t_d + \tau), \ln \tau\right]^T$ is given by

$$\mathbf{y} = \boldsymbol{\sigma}\mathbf{x} + \boldsymbol{\mu} \tag{F.3}$$

where $\boldsymbol{\sigma}$ is a square root of $\mathbf{C}$, $\mathbf{x} = \left[x_1, x_2, x_3\right]^T$ in which $x_i \sim N(0,1)$, (i =1,2 and 3) and $\boldsymbol{\mu}$ is a column vector with the mean values. Finally, a resulting $\mathbf{y}$ can be easily converted to obtain the original parameters, A, t_d and τ. Figure F.4 shows the generated sets of the parameter distributions which are similar to the distributions in Figure F.2.

In addition, $\boldsymbol{\sigma}$ can be easily calculated by first diagonalizing $\mathbf{C}$

$$\mathbf{U}^{-1}\mathbf{C}\mathbf{U} = \mathbf{D} = \mathbf{D}_s{}^2 \tag{F.4}$$

where $\mathbf{U}$ is the matrix of the eigenvectors, $\mathbf{D}$ is the diagonal matrix with the eigenvalues and $\mathbf{D}_s$ is the square root of $\mathbf{D}$ with its elements being the square roots of the elements of $\mathbf{D}$. Then,

$$\mathbf{C} = \mathbf{U}\mathbf{D}_s{}^2\mathbf{U}^{-1} = (\mathbf{U}\mathbf{D}_s\mathbf{U}^{-1})(\mathbf{U}\mathbf{D}_s\mathbf{U}^{-1}) \tag{F.5}$$

and thus

$$\boldsymbol{\sigma} = \mathbf{U}\mathbf{D}_s\mathbf{U}^{-1} \tag{F.6}$$

which is, in the current problem, found as

$$\boldsymbol{\sigma} = \begin{bmatrix} 0.5094 & -0.0541 & -0.0558 \\ -0.0541 & 0.2997 & 0.1343 \\ -0.0558 & 0.1343 & 0.2376 \end{bmatrix} \tag{F.7}$$

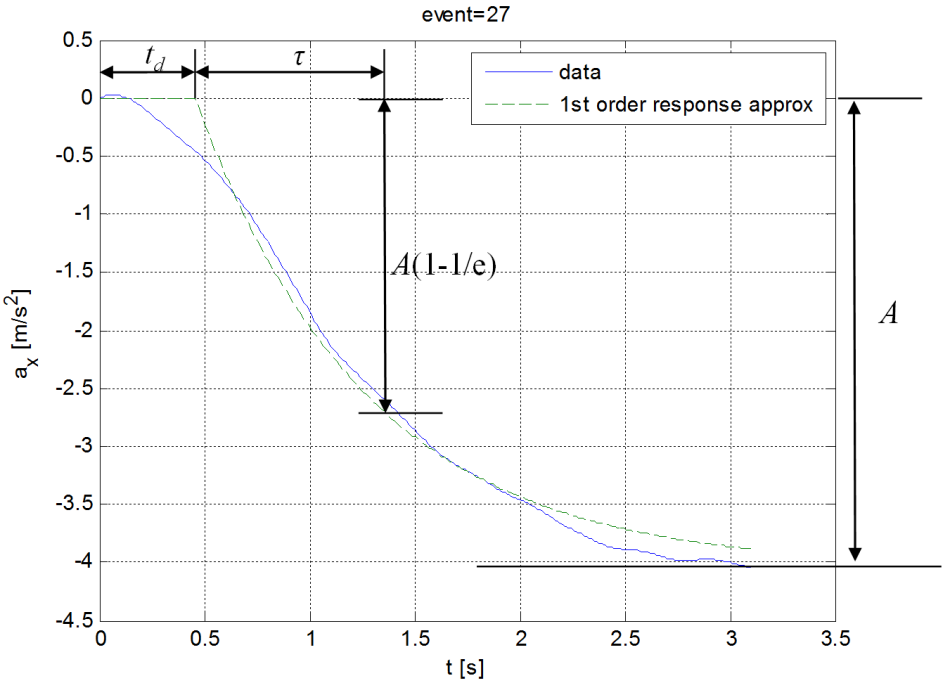

Figure F.1 Braking response and fitted curve.

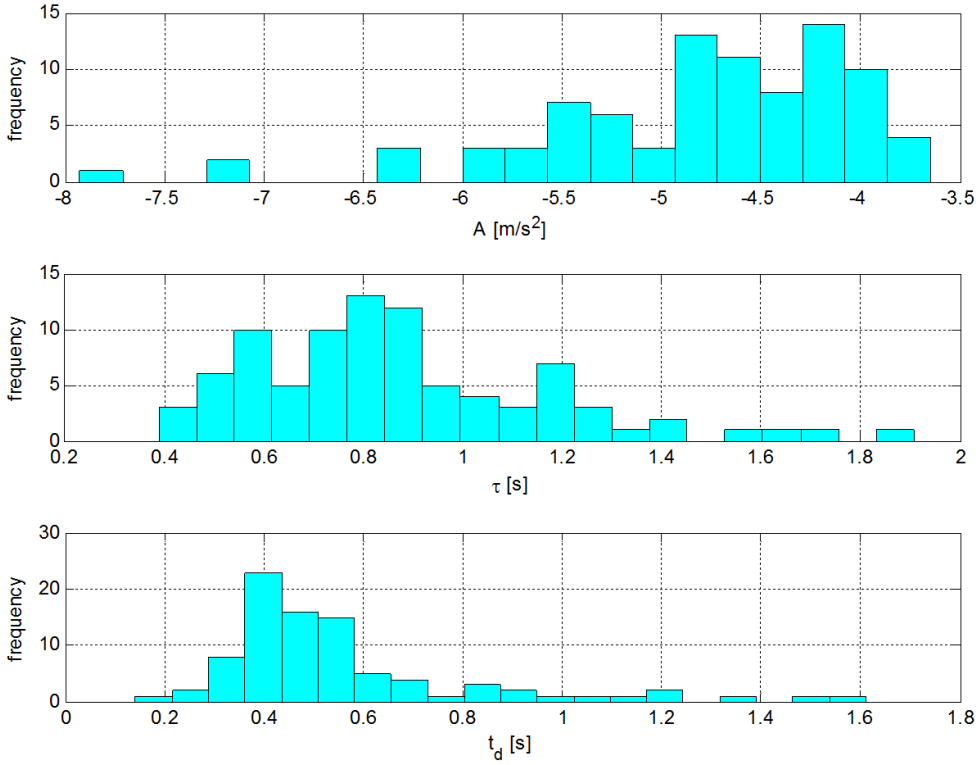

Figure F.2 Distributions of the braking model parameters.

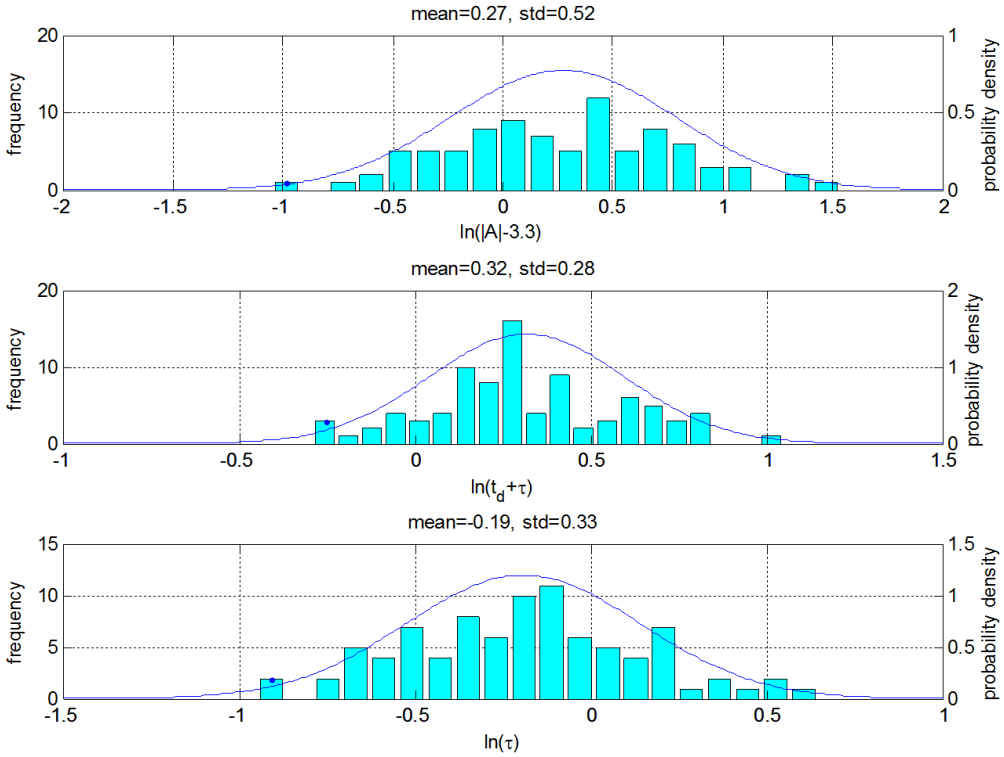

Figure F.3 Distributions of ln(|*A*|-3.3), ln(t_d+τ) and lnτ.

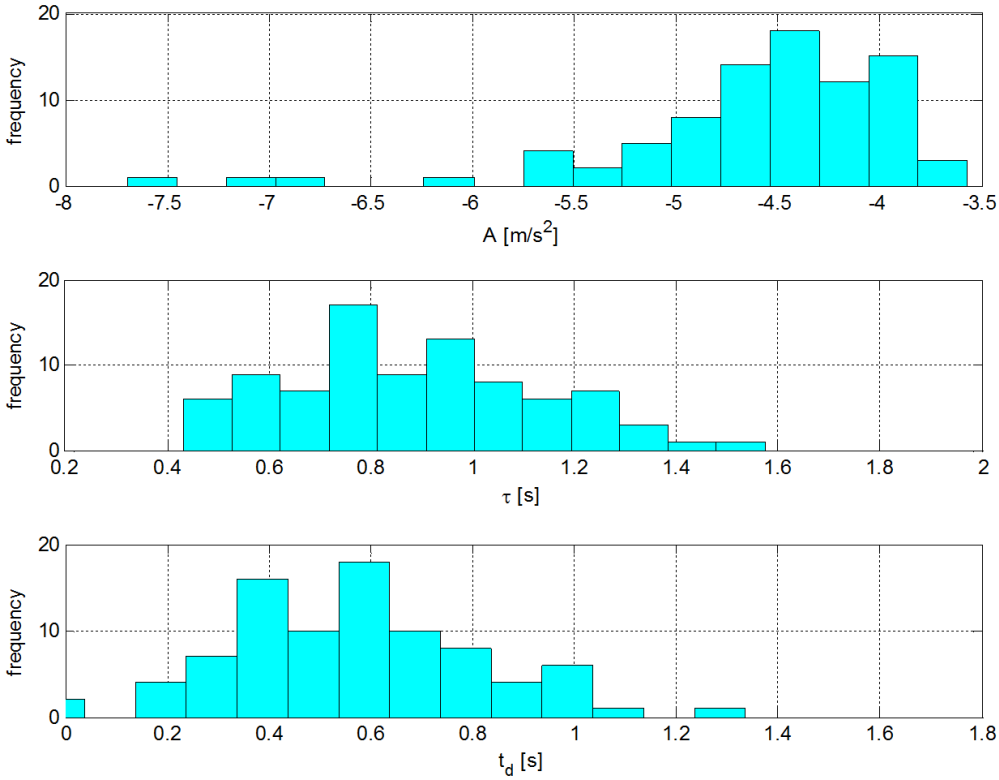

Figure F.4 Distributions of generated parameter values.

References

[1] Annual Report, 2011, "Traffic Safe Facts 2009: Early Edition," National Highway Traffic Safety Administration, DOT HS 811 402, Washington, DC.

[2] Najm, W.G., Smith, J.D., and Smith, D.L., 2001, "Analysis of Crossing Path Crashes," National Highway Traffic Safety Administration, DOT HS 809 423, Washington, DC.

[3] Ragland, D.R., and Zabyshny, A.A., 2003, "Intersection Decision Support Project: Taxonomy of Crossing-Path Crashes at Intersections Using GES 2000 Data," Institute of Transportation Studies, University of California, Berkeley.

[4] Pierowicz, J., Jocoy, E., Lloyd, M., Bittner, A., and Pirson, B., 2000, "Intersection Collision Avoidance Using ITS Countermeasures," National Highway Traffic Safety Administration, DOT HS 809 171, Washington, DC.

[5] Misener, J., Barnes, M., Chan, C.Y., Cody, D., Dickey, S., Goodsell, R., Gordon, T., Kim, Z.W., Kuhn, T., Lian, T., Nelson, D., Nowakowski, C., Nobukawa, K., Sharafsaleh, A., Shladover, S.E., Spring, J., VanderWerf, J., Zhang, W.B., Zhang, L., and Zhou, K., 2010, "Cooperative Intersection Collision Avoidance System (CICAS) : signalized left turn assist and traffic signal adaptation," California PATH Program, Institute of Transportation Studies, University of California at Berkeley, Berkeley, CA.

[6] Hayward, J. C., 1972, "Near-Miss Determination through use of A Scale of Danger," (384), pp. 24-34.

[7] Allen, B. L., Shin, T. T., and Cooper, P. J., 1978, "Analysis of Traffic Conflicts and Collisions," Transportation Research Record, **667**, pp. 67-74.

[8] Gettman, D., and Head, L., 2003, "Surrogate Safety Measures from Traffic Simulation Models," Federal Highway Administration, FHWA-RD-03-050.

[9] Chan, C. Y., 2006, "Characterization of Driving Behaviors Based on Field Observation of Intersection Left-Turn Across-Path Scenarios," IEEE Transactions on Intelligent Transportation Systems, **7**(3), pp. 322-331.

[10] Nobukawa, K., Barnes, M., Goodsell, R., and Gordon, T., 2009, "Reconstruction of Vehicle Trajectories for Intersection Conflict Analysis Using Vehicle-Based Sensors," International Association for Vehicle System Dynamics, Stockholm, Sweden.

[11] McRuer, D. T., and Krendel, E. S., 1959, "The Human Operator as A Servo System Element Part I," Journal of the Franklin Institute, **267**(5), pp. 381-403.

[12] McRuer, D. T., and Krendel, E. S., 1959, "The Human Operator as A Servo System Element Part II," Journal of the Franklin Institute, **267**(6), pp. 511-536.

[13] McRuer, D. T., Allen, W. R., Weir, D. H., and Klein, R. H., 1977, "New Results in Driver Steering Control Models," Human Factors, **19**(4), pp. 381-397.

[14] MacAdam, C. C., 1980, "An Optimal Preview Control for Linear Systems," Journal of Dynamic Systems, Measurement, and Control, **102**, pp. 188-190.

[15] Gordon, T. J., and Magnuski, N., 2006, "Modeling normal driving as a collision avoidance process," 8th International Symposium on Advanced Vehicle Control (AVEC), Taipei, Taiwan.

[16] Gordon, T., Blankespoor, A., Barnes, M., Blower, D., Green, P., and Kostyniuk, L., 2009, "Yaw Rate Error: A Dynamic Measure of Lane Keeping Control Performance for the Retrospective Analysis of Naturalistic Driving Data," Proceedings of the 21st International Technical Conference on the Enhanced Safety of Vehicles.

[17] Wilde, G. J. S., 1982, "The Theory of Risk Homeostasis: Implications for Safety and Health," Risk Analysis, **2**(4), pp. 209-225.

[18] Näätänen, R., and Summala, H., 1974, "A Model for the Role of Motivational Factors in Drivers' Decision-Making," Accident Analysis & Prevention, **6**(3-4), pp. 243-261.

[19] Fuller, R., 1984, "A Conceptualization of Driving Behaviour as Threat Avoidance," Ergonomics, **27**(11), pp. 1139-1155.

[20] Godthelp, H., Milgram, P., and Blaauw, G. J., 1984, "The Development of a Time-Related Measure to Describe Driving Strategy," Human Factors: The Journal of the Human Factors and Ergonomics Society, **26**(3), pp. 257-268.

[21] van Winsum, W., and Godthelp, H., 1996, "Speed Choice and Steering Behavior in Curve Driving," Human Factors, **38**(3), pp. 434-441.

[22] Rasmussen, J., 1983, "Skills, Rules, and Knowledge Signals, Signs, and Symbols, and Other Distinctions in Human Performance Models." IEEE Transactions on Systems, Man, and Cybernetics, **13**(3), pp. 257.

[23] Michon, J.A., 1985, "Human Behavior and Traffic Safety,"Plenum, New York, pp. 485-520.

[24] Hale, A. R., Stoop, J., and Hommels, J., 1990, "Human Error Models as Predictors of Accident Scenarios for Designers in Road Transport Systems," Ergonomics, **33**(10), pp. 1377-1387.

[25] Hollnagel, E., 2002, "Time and Time again," Theoretical Issues in Ergonomics Science, **3**(2), pp. 143-158.

[26] Hollnagel, E., Nåbo, A., and Lau, I. V., 2003, "A systemic model for driver-in-control," The Second International Driving Symposium on Human Factors in Driver Assessment, Training and Vehicle Design, Park City, Utah, pp. 86-91.

[27] Chandler, R. E., Herman, R., and Montroll, E. W., 1958, "Traffic Dynamics: Studies in Car Following," Operations Research, **6**(2), pp. 165-184.

[28] Newell, G. F., 1961, "Nonlinear Effects in the Dynamics of Car Following," Operations Research, **9**(2), pp. 209-229.

[29] Gipps, P. G., 1981, "A Behavioural Car-Following Model for Computer Simulation," Transportation Research Part B: Methodological, **15**(2), pp. 105-111.

[30] Fancher, P. S., and Bareket, Z., 1998, "Evolving Model for Studying Driver-Vehicle System Performance in Longitudinal Control of Headway," Transportation Research Record, **1631**(1), pp. 13-19.

[31] Yang, H. H., and Peng, H., 2010, "Development and Evaluation of Collision warning/collision Avoidance Algorithms using an Errable Driver Model," Vehicle System Dynamics, **48**(Supplement), pp. 525-535.

[32] Reymond, G., Kemeny, A., Droulez, J., and Berthoz, A., 2001, "Role of Lateral Acceleration in Curve Driving: Driver Model and Experiments on a Real Vehicle and a Driving Simulator," Human Factors: The Journal of the Human Factors and Ergonomics Society, **43**(3), pp. 483-495.

[33] Hisaoka, Y., Yamamoto, M., and Okada, A., 1999, "Closed-Loop Analysis of Vehicle Behavior during Braking in a Turn," JSAE Review, **20**(4), pp. 537-542.

[34] Yamakado, M., and Abe, M., 2008, "An Experimentally Confirmed Driver Longitudinal Acceleration Control Model Combined with Vehicle Lateral Motion," Vehicle System Dynamics, **46**(Supplement), pp. 129.

[35] Kondo, M., and Ajimine, A., 1968, "Driver's sight point and dynamics of the driver-vehicle-system related to it," Automotive Engineering Congress, Detroit, Michigan, pp. 1-14.

[36] Levison, W. H., Kantowitz, B. H., Moyer, M. J., and Robinson, M., 1998, "A Stopping-Distance Model for Driver Speed Decision Making in Curve Approach," Human Factors and Ergonomics Society Annual Meeting**, 42**, pp. 1222-1226.

[37] MacAdam, C. C., 2003, "Understanding and Modeling the Human Driver," Vehicle System Dynamics, **40**(1), pp. 101.

[38] Drury, C. G., 1971, "Movements with Lateral Constraint," Ergonomics, **14**(2), pp. 293.

[39] Bottoms, D. J., 1983, "The Interaction of Driving Speed, Steering Difficulty and Lateral Tolerance with Particular Reference to Agriculture," Ergonomics, **26**(2), pp. 123-139.

[40] DeFazio, K., Wittman, D., and Drury, C. G., 1992, "Effective Vehicle Width in Self-Paced Tracking," Applied Ergonomics, **23**(6), pp. 382-386.

[41] Coutton-Jean, C., Mestre, D. R., Goulon, C., and Bootsma, R. J., 2009, "The Role of Edge Lines in Curve Driving," Transportation Research Part F: Traffic Psychology and Behaviour, **12**(6), pp. 483-493.

[42] Hogema, J.H., 1996, "Effects of rain on Daily Traffic Volume and on Driving Behaviour," TNO, TM-96-B019, Soesterberg, Netherlands.

[43] Guo, K., and Guan, H., 1993, "Modelling of driver/vehicle Directional Control System," Vehicle System Dynamics: International Journal of Vehicle Mechanics and Mobility, **22**(3 & 4), pp. 141-184.

[44] Misener, J.A., Chan, C.Y., Cody, D., Dickey, S., Nowakowski, C., Greenhouse, D., Ragland, D., Shladover, S.E., and Vanderwerf, J., 2007, "California Intersection

Decision Support: A Systems Approach to Achieve Nationally Interoperable Solutions II," California Partners for Advanced Transit and Highways.

[45] Hartman, K., and Strasser, J., 2005, "Saving Lives Through Advanced Vehicle Safety Technology: Intelligent Vehicle Initiative Final Report," Federal Highway Administration, FHWA-JPO-05-057.

[46] Kuchar, J. K., 1996, "Methodology for Alerting-System Performance Evaluation," Journal of Guidance, Control, and Dynamics, **19**(2), pp. 438-444.

[47] Lee Yang, Ji Hyun Yang, Feron, E., and Kulkarni, V., 2003, "Development of a performance-based approach for a rear-end collision warning and avoidance system for automobiles," Intelligent Vehicles Symposium, 2003. Proceedings. IEEEIntelligent Vehicles Symposium, 2003. Proceedings. IEEE, pp. 316-321.

[48] Cheng, S. Y., and Trivedi, M. M., 2006, "Turn-Intent Analysis using Body Pose for Intelligent Driver Assistance," Pervasive Computing, IEEE, **5**(4), pp. 28-37.

[49] Salvucci, D. D., Mandalia, H. M., Kuge, N., and Yamamura, T., 2007, "Lane-Change Detection using a Computational Driver Model," Human Factors, **49**(3), pp. 532-542.

[50] Doshi, A., and Trivedi, M. M., 2009, "On the Roles of Eye Gaze and Head Dynamics in Predicting Driver's Intent to Change Lanes," Intelligent Transportation Systems, IEEE Transactions on, **10**(3), pp. 453-462.

[51] Sheridan, T.B., and Ferrell, W.R., 1981, "Man-machine systems: Information, control, and decision models of human performance," MIT Press, Cambridge, MA, pp. 452.

[52] McNicol, D., 2005, "A primer of signal detection theory," Lawrence Erlbaum Associates, Mahwah, NJ, pp. 240.

[53] LeBlanc, D., Sayer, J., Winkler, C., Ervin, R., Bogard, S., Devonshire, J., Mefford, M., Hagan, M., Bareket, Z., Goodsell, R., and Gordon, T., 2006, "Road Departure Crash Warning System Field Operational Test: Methodology and Results, Volume 1: Technical Report," National Highway Traffic Safety Administration, UMTRI-2006-9-1, Washington, DC.

[54] Bevly, D. M., Gerdes, J. C., Wilson, C., and Zhang, G., 2000, "The Use of GPS Based Velocity Measurements for Improved Vehicle State Estimation," Proceedings of the American Control Conference.

[55] Ryu, J., Rossetter, E. J., and Gerdes, J. C., 2002, "Vehicle Sideslip and Roll Parameter Estimation using GPS," Proceedings of the 6th International Symposium on Advanced Vehicle Control.

[56] Roecker, J. A., and McGillem, C. D., 1988, "Comparison of Two-Sensor Tracking Methods Based on State Vector Fusion and Measurement Fusion," Aerospace and Electronic Systems, IEEE Transactions on, **24**(4), pp. 447-449.

[57] Gan, Q., and Harris, C. J., 2001, "Comparison of Two Measurement Fusion Methods for Kalman-Filter-Based Multisensor Data Fusion," IEEE Transactions of Aerospace and Electronic Systems, **37**(1), pp. 273-280.

[58] Bar-Shalom, Y., and Li, X.R., 1995, YBS Publishing, pp. 395.

[59] McLeod, R. W., and Ross, H. E., 1983, "Optic-Flow and Cognitive Factors in Time-to-Collision Estimates," Perception, **12**, pp. 417-423.

[60] Cavallo, V., and Laurent, M., 1988, "Visual Information and Skill Level in Time-to-Collision Estimation," Perception, **17**, pp. 623-632.

[61] Schiff, W., and Detwiler, M. L., 1979, "Information used in Judging Impending Collision," Perception, **8**, pp. 647-658.

[62] Caird, J. K., and Hancock, P. A., 1994, "The Perception of Arrival Time for Different Oncoming Vehicles at an Intersection," Ecological Psychology, **6**(2), pp. 83-109.

[63] Kaiser, M. K., and Mowafy, L., 1993, "Optical Specification of Time-to-Passage: Observers' Sensitivity to Global Tau," Journal of Experimental Psychology: Human Perception and Performance, **19**(5), pp. 1028-1040.

[64] Cooper, P. J., and Zheng, Y., 2002, "Turning Gap Acceptance Decision-Making: The Impact of Driver Distraction," Journal of Safety Research, **33**(3), pp. 321-335.

[65] DeLucia, P. R., Kathryn Bleckley, M., Meyer, L. E., and Bush, J. M., 2003, "Judgments about Collision in Younger and Older Drivers," Transportation Research Part F: Traffic Psychology and Behaviour, **6**(1), pp. 63-80.

[66] Yan, X., Radwan, E., and Guo, D., 2007, "Effects of Major-Road Vehicle Speed and Driver Age and Gender on Left-Turn Gap Acceptance," Accident Analysis & Prevention, **39**(4), pp. 843-852.

[67] Hancock, P. A., and Manser, M. P., 1997, "Time-to-Contact: More than Tau Alone," Ecological Psychology, **9**(4), pp. 265-297.

[68] Schiff, W., Oldak, R., and Shah, V., 1992, "Aging Persons' Estimates of Vehicular Motion," Psychology and Aging, **7**(4), pp. 518-525.

[69] Lee, D. N., 1976, "A Theory of Visual Control of Braking Based on Information about Time-to-Collision," Perception, **5**, pp. 437-459.

[70] Bar-Shalom, Y., Li, X.R., and Kirubarajan, T., 2001, "Estimation with applications to tracking and navigation," Wiley, New York, pp. 274-275.

[71] Land, M. F., and Lee, D. N., 1994, "Where we Look when we Steer," Nature, **369**(6483), pp. 742-744.

[72] Felipe, E., and Navin, F., 1998, "Automobiles on Horizontal Curves: Experiments and Observations," Transportation Research Record: Journal of the Transportation Research Board, **1628**, pp. 50-56.

[73] Herrin, G. D., and Neuhardt, J. B., 1974, "An Empirical Model for Automobile Driver Horizontal Curve Negotiation," Human Factors, **16**(2), pp. 129-133.

[74] Levison, W. H., Bittner Jr., A. C., Campbell, J. L., and Schreiner, C., 2002, "Modification and Partial Validation of the Driver/Vehicle Module," Transportation Research Record, **1803**, pp. 52-58.

[75] Odhams, A. M. C., and Cole, D. J., 2004, "Models of Driver Speed Choice in Curves," Proceedings of the 7th International Symposium on Advanced Vehicle Control (AVEC), pp. 439-444.

[76] Ritchie, M. L., McCoy, W. K., and Welde, W. L., 1968, "A Study of the Relation between Forward Velocity and Lateral Acceleration in Curves during Normal Driving," Human Factors, **10**(3), pp. 255-258.

[77] Kozak, K., Pohl, J., Birk, W., Greenberg, J., Artz, B., Blommer, M., Cathey, L., and Curry, R., 2006, "Evaluation of Lane Departure Warnings for Drowsy Drivers," Human Factors and Ergonomics Society Annual Meeting**, 50**, pp. 2400-2404.

[78] Dingus, T. A., McGehee, D. V., Manakkal, N., Jahns, S. K., Carney, C., and Hankey, J. M., 1997, "Human Factors Field Evaluation of Automotive Headway maintenance/collision Warning Devices," Human Factors: The Journal of the Human Factors and Ergonomics Society, **39**(2), pp. 216-229.

[79] Green, M., 2000, ""how Long does it Take to Stop?" Methodological Analysis of Driver Perception-Brake Times," Transportation Human Factors, **2**(3), pp. 195.

[80] Johansson, G., and Rumar, K., 1971, "Drivers' Brake Reaction Times," Human Factors: The Journal of the Human Factors and Ergonomics Society, **13**(1), pp. 23-27.

[81] Taoka, G., 1989, "Brake Reaction Times of Unalerted Drivers," ITE Journal, **59**(3), pp. 19-21.

[82] Sohn, S. Y., and Stepleman, R., 1998, "Meta-Analysis on Total Braking Time," Ergonomics, **41**(8), pp. 1129.

[83] Gordon, T., Blower, D., Nobukawa, K., Sardar, H., Sullivan, J., Goudy, R., Christensen, A., and Mizoguchi, K., 2011, "Advanced crash avoidance technologies 2 program (ACAT) - Final report - Lane change conflicts," National Highway Traffic Safety Administration, Washington, D.C.

[84] Ervin, R., Sayer, J., LeBlanc, D., Bogard, S., Mefford, M., Hagan, M., Bareket, Z., and Winkler, C., 2005, "Automotive collision avoidance system field operational test methodology and results," National Highway Traffic Safety Administration, DOT HS 809 901, Washington D.C.

[85] Papalambros, P.Y., and Wilde, D., J., 2000, "Principles of Optimal Design: Modeling and Computation," Cambridge University Press, .

[86] Everson, R. M., and Fieldsend, J. E., 2006, "Multiobjective Optimization of Safety Related Systems: An Application to Short-Term Conflict Alert," IEEE Transactions on Evolutionary Computation, **10**(2), pp. 187-198.

[87] Anastasio, M. A., Kupinski, M. A., and Nishikawa, R. M., 1998, "Optimization and FROC Analysis of Rule-Based Detection Schemes using a Multiobjective Approach," IEEE Transactions on Medical Imaging, **17**(6), pp. 1089-1093.

[88] Schwefel, H., 1995, "Evolution and optimum seeking," Wiley, New York, pp. 444.

[89] Knowles, J., and Corne, D., 1999, "The Pareto archived evolution strategy: a new baseline algorithm for Pareto multiobjective optimisation," Evolutionary Computation, 1999. CEC 99. Proceedings of the 1999 Congress onProceedings of the 1999 Congress on Evolutionary Computation, pp. 98-105.

[90] Rakha, H., El-Shawarby, I., and Setti, J. R., 2007, "Characterizing Driver Behavior on Signalized Intersection Approaches at the Onset of a Yellow-Phase Trigger," IEEE Transactions on Intelligent Transportation Systems, **8**(4), pp. 630-640.